UNIVERSITY OF OKLAHOMA

GRADUATE COLLEGE

REACTIONS OF NITRIC OXIDE, NITROSOALKANES WITH GROUP 8 & 9

METALLOPORPHYRINS AND HEME PROTEINS

A DISSERTATION

SUBMITTED TO THE GRADUATE FACULTY

in partial fulfillment of the requirements for the

Degree of

DOCTOR OF PHILOSOPHY

By

YE GUAN
Norman, Oklahoma
2015

REACTIONS OF NITRIC OXIDE, NITROSOALKANES WITH GROUP 8 & 9
METALLOPORPHYRINS AND HEME PROTEINS

A DISSERTATION APPROVED FOR THE
DEPARTMENT OF CHEMISTRY AND BIOCHEMISTRY

BY

_____
Dr. George B. Richter-Addo, Chair

_____
Dr. Ann H. West

_____
Dr. Shaorong Liu

_____
Dr. Zhibo Yang

_____
Dr. Zhisheng Shi

ACKNOWLEDGEMENTS

valuable suggestions throughout the years. They were very thoughtful and supportive during my pregnancy and the first year after my son's birth. I thank them for all the help, consideration and tolerance.

My parents are always proud of me and they are my source of confidence. I thank them from my soul for their unconditional love and care. I wouldn't have made this far without them. I would also like to thank my beloved husband, Dr. Penghe Qiu, for all the support and encouragement throughout this experience. To my beloved son, Charley Qiu, I would like to express my thanks for being such a little good boy always bringing me joy and cheering me up.

TABLE OF CONTENTS

LIST OF FIGURES

ABSTRACT

This dissertation describes the interactions of nitric oxide (NO) and *C*-nitrosoalkanes (RNO) with group 8 and 9 metalloporphyrins and heme proteins. The goal of this research is to provide new information on the coordination chemistry of NO and NO-related compounds.

Chapter 1 introduces the biological role of nitric oxide (NO), the application of heme models, and previous research on the *C*-nitrosoalkane adducts of metalloporphyrins from our former group members and others.

Chapter 2 describes the synthesis and structural characterization of nitrosoamphetamine and *N*-hydroxyamphetamine adducts of group 8 & 9 metalloporphyrins. The reactivity of selected complexes was studied. Density functional theory calculations were also conducted on selected structurally characterized metalloporphyrin-nitrosoamphetamine and metalloporphyrin-*N*-hydroxyamphetamine complexes, and the data were compared to the experimental results.

Chapter 3 focuses on the coordination chemistry of *C*-nitroso compounds with heme proteins. In this chapter, the first crystal structures of hemoglobin (Hb) in complex with nitrosoalkanes are presented, along with sperm whale H64A myoglobin (Mb) in complex with NOAmph. The two structures of the Hb-nitrosoalkane proteins surprisingly revealed insight into the Hb degradation process induced by organic *C*-nitroso complexes. The structure of sw H64AMb(NOAmph) displayed an unexpected orientation of the NOAmph ligand in the heme pocket.

Chapter 4 describes the interactions between NO and d^6 group 9 metalloporphyrins. In this work, a series of d^6 group 9 metalloporphyrins were

synthesized and structurally characterized. They were used as precursors for the reactions with NO gas. The first known molecular structures of rhodium nitrosyl porphyrins are described, as well as the first observation of a NO insertion into a metal-carbon bond in a porphyrin system, which resulted in the formation of a *C*-nitroso ligand.

Chapter 1. Introduction

Nitric oxide (NO) is a simple diatomic molecule. It has received great research attention in the last two decades for its biological roles in vasodilation and neurotransmission in mammals.[1-3] The most important biological reaction of NO is perhaps its interaction with heme proteins. NO is biosynthesized by a heme-containing enzyme, NO synthase.[4] As a signaling agent in vasodilation, NO stimulates a heme containing protein, namely soluble guanylyl cyclase (sGC), through binding with the heme group of this enzyme.[5,6] The most intensively studied interaction between NO and heme proteins is the coordination of NO to the metal centers of these proteins.[7-10] Due to the complexity of the protein-NO interaction and the difficulties of obtaining protein crystal structures, much of the research on the interactions between NO and heme proteins is complemented by using synthetic metalloporphyrins as heme models.[11-15]
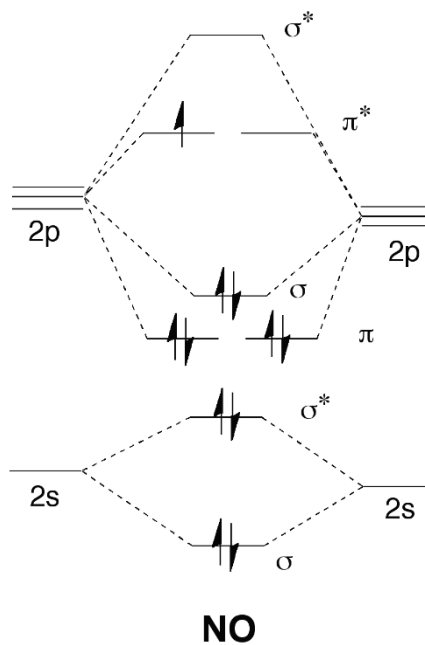
Figure 1.1. The molecular orbital diagram of NO.

It is important to note that NO is a free radical. As shown in Figure 1.1, the π^* orbital of NO is singly occupied. When NO bonds with a transition metal complex, there is a back-donation of electron density from the metal d orbital into the π^* antibonding orbital of NO, this results in a weakening of the N-O bond which lowers υ_{NO} in the IR spectrum.

Iron protoporphyrin IX (PPIX) (Figure 1.2), also known as heme *b*, plays an important role in biology. It is the iron-containing cofactor of myoglobin (Mb) and hemoglobin (Hb) proteins.[16] The propionate groups of PPIX participate in important hydrogen bonds with solvent (water) and some amino acids near the distal pockets of Mb and Hb. [17]
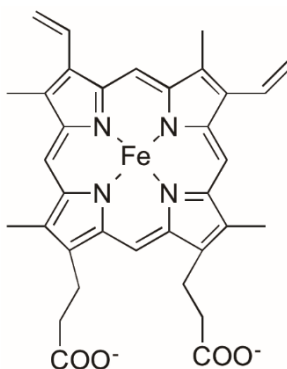
Figure 1.2. The structure of heme *b* (iron protoporphyrin IX).

Heme is produced in nature through a complex eight-step biosynthetic pathway involving multiple enzymes.[18,19] However, this asymmetric porphyrin is difficult to synthesize in the laboratory. Consequently, a series of symmetrical and hydrophobic porphyrins have been synthesized and utilized by bioinorganic chemists as models for heme. The known synthetic iron porphyrins used in this dissertation include the octa-β-substituted 2,3,7,8,12,13,17,18-octaethylporphyrin (OEPH$_2$) (Figure 1.3, *top left*), the

tetra-*meso*-substituted 5,10,15,20-tetraphenylporphyrin (TPPH$_2$) (Figure 1.3, *top right*) and the tetra-*meso*-substituted 5,10,15,20-tetra(*p*-methoxyphenyl)porphyrin (T(*p*-OMe)PPH$_2$) (Figure 1.3, *bottom*).

(OEP)Fe

(TPP)Fe

(T(p-OMe)PP)Fe
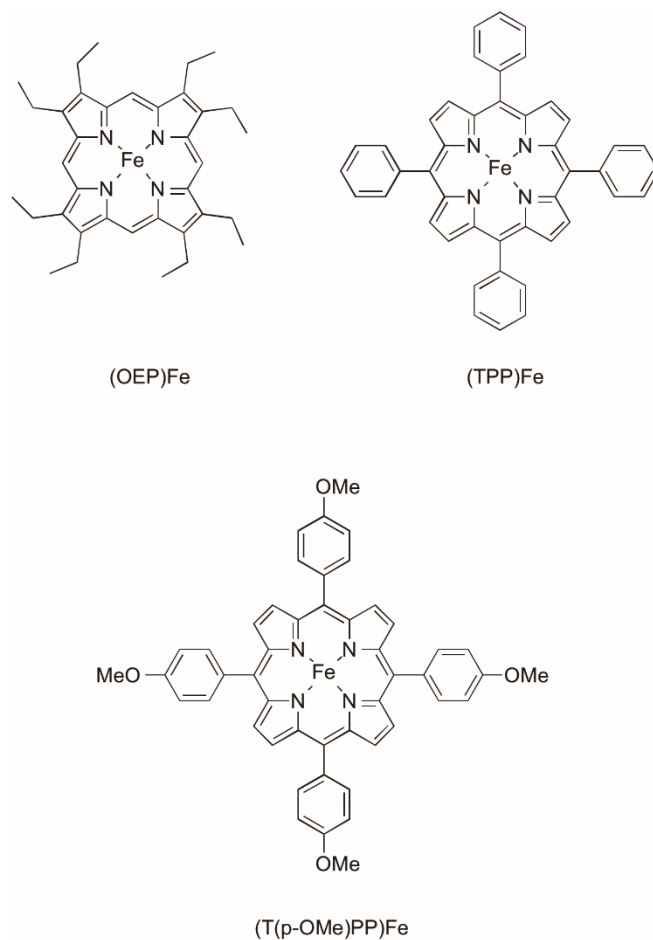
Figure 1.3. Synthetic iron porphyrin complexes used in this work.

Our group is interested in the chemistry of NO$_x$ species. One branch of our research is the study of the interaction of *C*-nitroso compounds with metal porphyrins and heme proteins. The *C*-nitroso compounds, as shown in Figure 1.4, have the general formula RNO (R= aryl or alkyl). The nitroso moiety in these molecules is valence isoelectronic with dioxygen, and displays strong binding affinity towards the metal

centers of porphyrins. Studies in the early 1970s on *C*-nitroso compounds revealed that they are toxic substances and play important physiological roles in biology. A variety of RNO compounds have been demonstrated to react with heme proteins such as myoglobin (Mb), hemoglobin (Hb) and cytochrome P450 to form stable complexes that consequently result in the inhibition of these heme proteins.[20-22] In addition, the formation of nitrosobenzene from the oxidative metabolism of aniline was found to induce methemoglobinemia and hemolytic anemia in animals.[23,24]

$$R - \ddot{N} \diagdown\!\!\!\!\diagup O$$
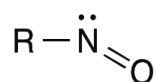
R = alkyl, aryl

Figure 1.4. The structure of *C*-nitroso compounds.

Interestingly, all of the above-mentioned reports on the interactions of *C*-nitroso compounds with proteins were investigated using only UV-vis spectroscopy. No structural information was available at that time to reveal how RNO ligands coordinate with the metal center of heme proteins. In 1983, Mansuy prepared and structurally characterized the first metalloporphyrin-RNO complex, (TPP)Fe(^{i}PrNO)(^{i}PrNH$_2$).[25] This work established the *N*-binding mode of the RNO compound to the ferrous porphyrin (Figure 1.5, *left*).

Our group started to work on *C*-nitroso compounds in 1996. Our group demonstrated, by X-ray crystallography, that nitrosoarenes can bind to metal porphyrins through multiple modes (Figure 1.5).[26] While the d^6 (TPP)Fe^{II}(PhNO)$_2$ displayed an *N*-binding mode of the nitrosoarene, the d^5 [(TPP)Fe^{III}(Et$_2$NC$_6$H$_4$NO)$_2$]SbF$_6$ displayed the

4

hitherto unreported *O*-binding mode of a nitrosoarene. The same *O*-binding mode was

observed in the structure of a d^4 Mn^{III} porphyrin complex, namely

[(TPP)Mn(ONC$_6$H$_4$NEt$_2$)$_2$]SbF$_6$, published by our group. [27] To date, these are the only

two known *O*-binding *C*-nitroso metal porphyrin complexes reported in the literature.

All other reactions of RNO (R = phenyl, tolyl, isopropyl) with d^6 Fe^{II}, Ru^{II}, Os^{II} and

Co^{III} porphyrins resulted in the formation of *N*-binding complexes.[28-30] The binding

mode of the RNO complex is quite an interesting topic, since it could help us to

understand how the *C*-nitroso ligands approach the heme center in the heme proteins.
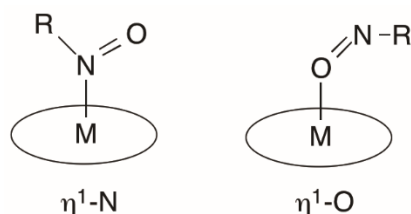
Figure 1.5. Two binding modes of RNO to metalloporphyrins.

In 2002, our group started to work on the structures of *C*-nitroso adducts of

heme proteins.[31] At the time, there was only one reported heme-nitrosoarene structure,

namely that of legHb(PhNO) from *Lupinus luteus*.[32] In 2003, a member from our group

who was jointly supervised by Dr. West, Daniel Copland, published the first crystal

structure of a heme protein complexed to a nitrosoalkane, namely horse heart

Mb(EtNO).[31] In both the structures of legHb(PhNO) and Mb(EtNO), the RNO ligand

bound with the heme center through the N atom as observed in the model complexes of

d^6 metal porphyrins.

My dissertation research consists of two main areas. In Chapters 2 and 3, I present my work on the interactions of *C*-nitroso compounds with synthetic metalloporphyrins and heme proteins. In Chapter 4, I present my work on the coordination chemistry of the NO molecule with d^6 group 9 metal porphyrins.

Chapter 2 focuses on a physiologically important, but structurally uncharacterized, *C*-nitroso compound nitrosoamphetamine (NOAmph), which is the *N*-oxidized derivative of amphetamine. A series of NOAmph adducts of metalloporphyrins were synthesized and structurally characterized, and the reactivity of selected complexes have been studied. The information I obtained fills in a gap of knowledge in the coordination chemistry of *C*-nitroso compounds such as nitrosoamphetamine.

In Chapter 3, I extend the studies to the interactions between *C*-nitroso compounds and heme proteins. I collaborated with two of our group members, Dr. Jun Yi and Bing Wang, to obtain the first crystal structures of a nitrosoalkane binding to Hb and of NOAmph binding to sperm whale (sw) H64AMb. The two structures of the Hb-nitrosoalkane proteins gave us insight into the Hb degradation process induced by organic *C*-nitroso complexes. The structure of NOAmph binding sw H64AMb also displayed an unexpected orientation of the NOAmph ligand in the heme pocket.

Chapter 4 describes my work on a previously unknown area in the coordination chemistry of NO with metal porphyrins. In this work, I managed to prepare and structurally characterize the first reported rhodium nitrosyl porphyrins, which displayed weak NO binding and unexpected long Rh-N(O) bond distances. I also observed, for the

first time, an NO insertion into a metal-carbon bond in any porphyrin system, which led

to the formation of a *C*-nitroso ligand.

References

(1)   Garg, U. C.; Hassid, A. *J Clin Invest* **1989**, *83*, 1774.

(2)   Gally, J. A.; Montague, P. R.; Reeke, G. N.; Edelman, G. M. *Proc Natl Acad Sci U S A* **1990**, *87*, 3547.

(3)   Palmer, R. M.; Ferrige, A. G.; Moncada, S. **1987**.

(4)   Marletta, M. A. *J Biol Chem* **1993**, *268*, 12231.

(5)   Stone, J. R.; Marletta, M. A. *Biochemistry* **1994**, *33*, 5636.

(6)   Bellamy, T. C.; Wood, J.; Garthwaite, J. *Proc Natl Acad Sci U S A* **2002**, *99*, 507.

(7)   Abu-Soud, H. M.; Ichimori, K.; Nakazawa, H.; Stuehr, D. J. *Biochemistry* **2001**, *40*, 6876.

(8)   Hu, S. Z.; Kincaid, J. R. *J Am Chem Soc* **1991**, *113*, 2843.

(9)   Ribeiro, J. M. C.; Hazzard, J. M. H.; Nussenzveig, R. H.; Champagne, D. E.; Walker, F. A. *Science* **1993**, *260*, 539.

(10)   Williams, P. A.; Fulop, V.; Garman, E. F.; Saunders, N. F. W.; Ferguson, S. J.; Hajdu, J. *Nature* **1997**, *389*, 406.

(11)   Richter-Addo, G. B.; Hodge, S. J.; Yi, G.-B.; Khan, M. A.; Ma, T.; Van Caemelbecke, E.; Guo, N.; Kadish, K. M. *Inorg Chem* **1996**, *35*, 6530.

(12)   Xu, N.; Goodrich, L. E.; Lehnert, N.; Powell, D. R.; Richter-Addo, G. B. *Angew Chem Int Edit* **2013**, *52*, 3896.

(13)   Xu, N.; Powell, D. R.; Richter-Addo, G. B. *Angew Chem Int Edit* **2011**, *50*, 9694.

(14)   Cheng, L.; Richter-Addo, G. B. Binding and Activation of Nitric Oxide by Metalloporphyrins and Heme. In *The Porphyrin Handbook*; Kadish, K.M., Smith, K. M., Guilard, R., Eds.; Academic Press: New York, 2000; Vol.4 (Biochemistry and Binding: Activation of Small Molecules), pp. 219-291

(15)   Cheng, L.; Chen, L.; Chung, H.-S.; Khan, M. A.; Richter-Addo, G. B.; Young, V. G. *Organometallics* **1998**, *17*, 3853.

(16)   Antonini, E.; Brunori, M. Hemoglobin and myoglobin in their reactions with ligands. Amsterdam, Netherlands: North-Holland Pub. Co.; **1971**.

(17)   Harada, K.; Makino, M.; Sugimoto, H.; Hirota, S.; Matsuo, T.; Shiro, Y.; Hisaeda, Y.; Hayashi, T. *Biochemistry* **2007**, *46*, 9406.

(18)   Ryter, S. W.; Tyrrell, R. M. *Free Radic Biol Med* **2000**, *28*, 289.

(19)   Ponka, P. *Blood* **1997**, *89*, 1.

(20)   Mansuy, D.; Chottard, J. C.; Chottard, G. *Eur J Biochem* **1977**, *76*, 617.

(21)   Mansuy, D.; Beaune, P.; Chottard, J. C.; Bartoli, J. F.; Gans, P. *Biochem Pharmacol* **1976**, *25*, 609.

(22)   James, R. C.; Franklin, M. R. *Biochem Pharmacol* **1975**, *24*, 835.

(23)   Harrison, J. H.; Jollow, D. J. *Mol Pharmacol* **1987**, *32*, 423.

(24)   Peter, E.; Michaela, A. *Bio Chem Hoppe-seyler* **1987**, 368, 285.

(25)   Mansuy, D.; Battioni, P.; Chottard, J. C.; Riche, C.; Chiaroni, A. *J Am Chem Soc* **1983**, *105*, 455.

(26)   Wang, L.-S.; Chen, L.; Khan, M. A.; Richter-Addo, G. B. *Chem Commun* **1996**, 323.

(27)   Schultze, S. J.; Chen, L.; Khan, M. A.; Richter-Addo, G. B. *Inorg Chem* **1997**, *36*, 6465.

(28)   Sohl, C. D.; Lee, J. Y.; Alguindigue, S. S.; Khan, M. A.; Richter-Addo, G. B. *J Inorg Biochem* **2004**, *98*, 1238.

(29)   Chen, L.; Khan, M. A.; Richter-Addo, G. B.; Young, V. G.; Powell, D. R. *Inorg Chem* **1998**, *37*, 4689.

(30)   Chen, L.; Fox, J. B.; Yi, G. B.; Khan, M. A.; Richter-Addo, G. B. *J Porphyr Phthalocya* **2001**, *5*, 702.

(31)   Richter-Addo, G. B.; Copeland, D. M.; West, A. H. *J Inorg Biochem* **2003**, *96*, 216.

(32)   I. P. Kuranova, A. V. T., G. V. Obmolova, A. A. Voronova, A. N. Popov, D. M. Kheiker and E. G. Arutyunyan *Bioorg. Khim.* **1982**, *8*, 1625.

Chapter 2. Reactions between *N*-hydroxyamphetamine and metalloporphyrins: synthesis, characterization and computational studies

2.1 Introduction

The coordination chemistry of *C*-nitroso (RNO, R = alkyl, aryl) compounds with transition metal porphyrins and proteins containing the heme group is a research interest of our group. The nitroso group on RNO compounds is isoelectronic with dioxygen, and has a high affinity to the metal center of some porphyrins.[1] Such affinity remains in the biological environment, which enables the efficient binding of RNO compounds towards the heme center in heme proteins.[2-4] As a result, the RNO compounds are known to be actively involved in various harmful biological metabolic processes, including the nitrobenzene poisoning,[5,6] the inhibition of cytochrome P450 enzymes[3,7] and the degradation of hemoglobins (discussed in Chapter 3).[8] To make things worse, the nitroso compounds can be generated from the metabolism of amine- and nitro-containing drugs. There is also an increased effort in the exploration of RNO compounds as NO donors for biological studies.[9] Thus, understanding the fundamental chemistry of *C*-nitroso binding to metal porphyrins becomes very crucial for drug design.[10]

RNO binding with metalloporphyrins has previously been extensively studied, including a series of (por)Fe(*i*PrNO)(L) (L=MeOH, py, 1-MeIm) complexes synthesized and characterized by our previous group member, Christal D. Sohl.[11] However, the structural studies are surprisingly limited to a small range of ligands. Most of the structures published to date show the binding of nitrosobenzene (PhNO) derivatives to the synthetic metalloporphyrins.[12-15] There is only one nitrosoalkane

ligand involved in such studies, which is the above-mentioned 2-nitrosopropane (^{i}PrNO). No drug-related nitrosoalkane compounds have previously been used in these kind of studies. Also, all the crystal structures of (por)Fe(^{i}PrNO)(L) contain an organic base as a *trans* ligand on the other side of the porphyrin, which serves as an electron-donating group, thus enhancing the π-backbonding from the metal to the ^{i}PrNO. Efforts of making nitrosoalkane bound iron porphyrin complexes without a *trans* ligand, to the best of my knowledge, have been unsuccessful. More importantly, the structures involving *C*-nitrosoalkanes are all from the reactions with d^6 Fe(II) porphyrins. Cobalt also plays a very important role in the biological environment. Surprisingly, however, the interactions of nitroso compounds with d^7 Co(II) porphyrins have not yet been reported.

Our work in this chapter is intended to fill in the gap in this area. We are interested in the reactions of iron/cobalt porphyrins with the nitroso derivative of a very important drug molecule, amphetamine (Amph). Amphetamine is known for its effects on elevating dopamine, norepinephrine and biogenic amines in human brain.[16] It has been profoundly used as an illicit drug, and has also been applied to the treatment of children with attention deficit hyperactivity disorder (ADHD) and adults with narcolepsy.[17,18] The metabolism of amphetamine has been wildly studied. *N*-hydroxyamphetamine (AmphNHOH) was identified as one of the *N*-oxygenated metabolites of amphetamine in liver from early work.[19-21] In a recent paper, human FMO3 was also reported to *N*-oxidize amphetamine and methamphetamine to AmphNHOH in vitro.[22] After the generation of AmphNHOH, it could easily react with different heme proteins (Cytochrome P450[2], PHGS[4]) to form stable Fe(II)-RNO

complexes and lead to the inhibition of the enzyme activities. Although there are extensive studies on the reaction mechanisms of amphetamine and its derivatives, the determinants of pharmacological toxicity of amphetamine remain unclear. The amphetamine-induced release of serum myoglobin is proposed to be a biomaker of the toxicity of this drug.[23]

2.2 Experimental section

2.2.1 Materials, instrumentation, and methods

The reactions were performed under anaerobic conditions using standard Schlenk techniques under an atmosphere of nitrogen and/or in an Innovative Technology Labmaster 100 Dry Box unless stated otherwise. Solvents used for the reactions were obtained from an Innovative Technology Pure Solv 400-5-MD Solvent Purification system under an atmosphere of nitrogen. A Bio-Rad FT-155 FTIR spectrometer was used to record the infrared spectra. Proton NMR spectra were recorded on Varian Mercury VX 300 MHz spectrometer or Varian VXR-S 400 MHz spectrometer for room temperature and low temperature experiments, and the signals were referenced to the solvent employed (CD_3Cl at 7.24 ppm). UV-vis data was collected on an HP 8453 diode array instrument with a 1.0 cm cuvette. X-ray diffraction data were collected by Dr. Douglas R.Powell using a diffractometer with a Bruker APEX ccd area detector[24,25] and graphite-monochromated Mo Kα radiation ($\lambda = 0.71703$Å).

Density functional calculations (B3LYP/DGDVZP) were performed using Gaussian-09[26] on the WebMO interface (https://webmo.oscer.ou.edu). Geometric optimizations, vibrational frequency calculations and molecular orbital calculations were performed for selected complexes: (porphine)Fe(1-MeIm)(NOAmph) (S = 0),

(porphine)Fe(NOAmph)-(AmphNHOH) (S = 0), (porphine)Fe(NOAmph)$_2$ (S = 0), (por)Fe(NOAmph) (S = 0), (por)Co(AmphNHOH) (S = 1/2).

Nitromethane (99.5%) and sodium borohydride (98.5%) were purchased from Sigma-Aldrich. *N*-butylamine (99%), benzaldehyde (99%), borane-tetrahydrofuran (1M solution in THF) were purchased from Aldrich Chemical Co. Anhydrous ethanol (ACS grade) was purchased from Pharmco-AAPER. Sodium bicarbonate was purchased from EM Science. Anhydrous magnesium sulfate (97%) was purchased from Mallinckrodt. Hydrochloric acid (37%) was purchased from EMD chemicals. Ether (anhydrous, 99.9%) was purchased from J.T.Baker. THF, dichloromethane and hexane were collected from the solvent distillation system under nitrogen.

(OEP)FeCl and (TPP)Co were purchased from Midcentury Chemicals. ((*p*-OMe)TPP)FeCl, (TPP)FeCl and (TPP)CoCl were prepared following literature methods.[27] The purity of the synthesized complexes was ascertained by spectroscopy.

2.2.2 Synthesis

1-Phenyl-2-nitropropene and *N*-hydroxyamphetamine were prepared following the literature methods with slightly modification.[28,29] 1-Phenyl-2-nitropropene was synthesized by reacting nitroethane (1.4 ml, 0.02 mol) with benzaldehyde (2.1 ml, 0.02 mol) in anhydrous ethanol (5 ml) with the addition of butylamine (0.1 ml, 0.001 mol). The mixture was refluxed for 8 hrs and resulted in the formation of a large amount of pale yellow crystals during cooling on ice. The crystals were washed with water and methanol to remove the orange colored impurities. The yield of the product was 60% by weight. ^{1}H NMR (CDCl$_3$): 8.10 (s, 1H, CH), 7.44 (m, 5H, phenyl), 2.42 (s, 3H, CH$_3$). The NMR spectrum is identical to that previously reported[30].

N-hydroxyamphetamine was prepared from the reduction of 1-phenyl-2-nitropropene with $BH_3 \cdot THF$ in a THF solution in the presence of a small amount of $NaBH_4$ as catalyst.[28] An oven-dried nitrogen-flushed Schlenk tube was cooled to 0 °C on ice. A $BH_3 \cdot THF$ (2.65 ml, 0.0027 mol) solution was added to Schlenk tube using a syringe under nitrogen. In another oven-dried nitrogen-flushed Schlenk tube, 1-phenyl-2-nitropropene (0.45 g, 0.0027 mol) was dissolved in 9.5 ml THF. The solution of 1-phenyl-2-nitropropene was slowly added to the $BH_3 \cdot THF$ solution cooled with ice bath. After addition was completed, the ice bath was removed, and a catalytic amount of $NaBH_4$ (~40mg) was added into the mixture. The solution was kept stirring until the yellow color of the starting material turned clear. Ice water (40 ml) and 5.5 ml HCl (10%) were then added to the mixture. The mixture was refluxed at 65 °C for 2 hours and cooled to room temperature. The organic soluble compounds were extracted with ether and discarded. Sodium carbonate was added to remaining aqueous fraction to neutralize the solution. Solid NaCl was added to the solution until saturated. The products were extracted with ether in three cycles. Anhydrous $MgSO_4$ was used to dry the extracts overnight and the solvent was removed under vacuum. The final yield of the product was 45% by weight of the white powdery product. The *N*-hydroxyamphetamine was kept at -20 °C in glove box for several weeks showing no sign of decomposition. It will gradually decompose to a yellow liquid if kept at room temperature. ^1H NMR ($CDCl_3$): 7.19-7.32 (m, 5H, phenyl group), 3.21 (m, 1H, CH), 2.65 (dd, 1H, CH_2), 2.85 (dd, 1H, CH_2). We did not observe the protons on the –NHOH group.

(OEP)Fe(ONCH(CH₃)CH₂Ph)(1-MeIm) (1): Excess *N*-hydroxyamphetamine
(0.037 g, 0.2 mmol) was added to a stirred 5 mL solution of (OEP)FeCl (0.037 g, 0.06
mmol) in CH_2Cl_2. The color of the solution changed from brown red to black purple
during a 6 hour period. 1-MeIm (0.02 ml, 0.25 mmol) was added into solution and the
mixture was stirred overnight. The solution was dried in vacuo and redissolved in a
CH_2Cl_2/hexane (1:1) mixture. 1-MeIm (0.01 ml, 0.125 mmol) was added to this solution.
Purple plate-shaped crystals formed during slow evaporation of the mixture in the dry
box at room temperature. The isolated yield of the crystals was 58%. IR (KBr, cm^{-1}):
ν_{NO} = 1419 s; also 1559 m, 1507 m, 1457 s, 1374 w, 1337 w, 1251 m, 1224 m, 1143 m,
1107 s, 1085 w, 1018 s, 955 s, 829 m, 745 s, 700 s. ^{1}H NMR (CDCl₃): 9.73 (s, 4H,
meso-H of OEP), 3.93 (q, 16H, *CH₂*CH₃ of OEP), 1.82 (t, 24H, CH₂*CH₃* of OEP), 6.78
(m, *p,m*-H of phenyl group), 5.78 (d, 2H, *o*-H of phenyl group), -0.578 (m, 1H, CH₂), -
1.58 (q, 1H, CH), -1.74 (d, 1H, CH₂), -2.525 (d, 3H, CH₃). The peaks of 1-MeIm were
not observed at room temperature, but could be observed in the NMR spectrum at lower
-40 °C. ^{1}H NMR (CDCl₃, -40 °C): 4.55 (s, 1H of 1-MeIm), 1.90 (s, overlapping with
CH₂CH₃ of OEP, CH₃ of 1-MeIm), 0.95 (s, 1H of 1-MeIm), 0.6 (s, 1H of 1-MeIm).

Attempted preparation of (OEP)Fe(ONCH(CH₃)CH₂Ph)(MeOH)(2): A mixture
of (OEP)FeCl (0.037 g, 0.06 mmol) and *N*-hydroxyamphetamine (0.037 g, 0.2 mmol) in
a 5 ml CH_2Cl_2/CH₃OH (2:1) solution was stirred for 6 h, during which time the solution
changed to a reddish purple color. The solution was dried in vacuo to give a solid
tentatively identified as (OEP)Fe(ONCH(CH₃)CH₂Ph)(MeOH). The slow evaporation
method with a CH_2Cl_2/MeOH solution did not grow X-ray quality crystals (78%
isolated yield of the micro crystals). IR (KBr, cm^{-1}): ν_{NO} = 1425 s; also 1657 w, 1546 w,

1495 w, 1453 s, 1375 s, 1298 m, 1268 s, 1226 w, 1146 s, 1110 m, 1057 s, 1016 s, 987 m, 957 s, 835 s, 744 s, 699 s.

Attempted preparation of (OEP)Fe(ONCH(CH₃)CH₂Ph)₂ (**3**): A mixture of (OEP)FeCl (0.015 g, 0.024 mmol) and *N*-hydroxyamphetamine (0.037 g, 0.2 mmol) in CH_2Cl_2 was stirred overnight, during which time the color changed from purple to black. The solution was dried in vacuo to give a solid tentatively identified as Fe(OEP)(ONCH(CH₃)CH₂Ph)₂. The residue was dissolved in a hexane/ CH_2Cl_2 mixture. The slow evaporation method did not yield X-ray quality crystals. IR (KBr, cm^{-1}): ν_{NO} = 1497 s; also 1453 s, 1377 s, 1318m, 1268 s, 1214 w, 1147 s, 1015 s, 983 w, 958 s, 915 m, 848 m, 744 s, 701 s.

(T(p-OMe)PP)Fe(ONCH(CH₃)CH₂Ph)₂ (**4**) : Excess *N*-hydroxyamphetamine (0.04 g, 0.22 mmol) was added to a 5 ml CH_2Cl_2 solution of (T(*p*-OMe)PP)FeCl (0.02 g, 0.02 mmol). The solution was stirred overnight (~12hr) and taken to dryness in vacuo. 1 ml CH_2Cl_2 was added to dissolve the red residue, followed by the careful layering of 8 ml on top of the CH_2Cl_2 solution. Purple block-shaped crystals formed at the bottom of solution within two weeks (35% isolated yield of crystals). IR (KBr, cm^{-1}): ν_{NO} = 1505cm^{-1}; also 1456 m, 1451 m, 1348 m, 1304 w, 1287 w, 1247 s, 1174 s, 1106 w, 1076 w, 1030 m, 999 s, 955 w, 809 m, 743 s, 700 s. ^{1}H NMR (CDCl₃): 8.70 (s, 8H, pyrrole-H of T(*p*-OMe)PP), 7.95 (d, 8H, *o*-H of T(*p*-OMe)PP), 7.20 (m, *meso*-H of T(*p*-OMe)PP, overlapped with CH_2Cl_2), 6.90 (m, 6H, *p,m*-H of phenyl group), 5.72 (d, 2H, *o*-H of phenyl group), 5.41 (d, 2H, *o*-H of phenyl group), 4.07 (s,12H, OCH₃ of T(*p*-OMe)PP), -0.7 (b, 2H, CH₂), -1.5 (m, 1H, CH), -1.90 (b, 2H, CH₂), -2.27 (d, 3H, CH₃).

Peaks of the second nitrosoamphetamine ligand were not clearly observed at room temperature.

(T(p-OMe)PP)Fe(ONCH(CH₃)CH₂Ph)₂ (**4**) and *(T(p-OMe)PP)Fe(ONCH(CH₃)CH₂Ph)* (**5**): The synthesis procedure was identical to the one just described for compound $(T(p\text{-OMe})PP)Fe(ONCH(CH_3)CH_2Ph)_2$. The crystal structure of the final product indicated that it was a mixture of both five and six coordinate complexes. IR (KBr, cm^{-1}): ν_{NO} = 1505 cm^{-1}, 1434 cm^{-1}; Also 1606 s, 1574 w, 1539 m, 1454 m, 1386 w, 1348 s, 1286 m, 1245 s, 1174 s, 1106 w, 1072 w, 1036 w, 995 s, 850 w, 798 s, 741 w, 715 m, 696 m, 606 s. ^{1}H NMR (CDCl₃): 8.72 (s, 8H, pyrrole-H of T(p-OMe)PP),7.98 (d, 8H, o-H of T(p-OMe)PP),7.30 (m, *meso*-H of T(p-OMe)PP, overlapped with CH₂Cl₂), 4.11 (s, 12H, OCH₃ of T(p-OMe)PP), 6.93 (m, 6H, *p,m*-H of phenyl group), 5.77 (d, 2H, o-H of phenyl group), -0.26 (t, 1H, CH₂), -0.93 (b, 1H, CH), -1.47 (d, 1H, CH₂), -2.21 (d, 3H, CH₃). Peaks of the second nitrosoamphetamine ligand were not clearly observed at room temperature.

(TPP)Fe(ONCH(CH₃)CH₂Ph)(NHOHCH(CH₃)CH₂Ph) (**6**): Excess *N*-hydroxyamphetamine (0.015 g, 0.1 mmol) was added into to a stirred 5 ml CH₂Cl₂ solution of (TPP)FeCl (0.015 g, 0.02 mmol). The solution was reacted overnight (~12 hr), during which time the color changed from yellow/red to red/purple. The product was taken to dryness in vacuo and the residue was re-dissolved in 1 ml of CH₂Cl₂. 6 ml of hexane was then careful layered on the top of the CH₂Cl₂ solution in Schlenk tube. Block-shaped black crystals were formed at the bottom of the solution after two weeks (40% isolated yield of crystals). IR (KBr, cm^{-1}): ν_{NO} = 1435; also 1599 s, 1538 w, 1494 s, 1453 s, 1349 m, 1303 m, 1259 m, 1204 w, 1177 w, 1073 m, 1002 s, 796 m, 744 s, 700

s. ^{1}H NMR (CDCl$_3$): 13.40 (b, H of NH), 12.00 (b, H of OH), 8.64 (pyrrole-H of TPP), 7.97 (o-H of TPP), 7.60 (p, m-H of TPP), 6.84 (p, m-H of phenyl group), 5.64 (o-H of phenyl group), -0.61 (H of CH$_2$), -1.61 (H of CH), -2.35 (H of CH$_3$).

(TPP)Fe(ONCH(CH$_3$)CH$_2$Ph)(1-MeIm) (**7**): To a solution of Fe(TPP)Cl (0.02 g, 0.028 mmol) was added *N*-hydroxyamphetamine (0.02 g, 0.13 mmol) followed by the addition of 1-MeIm (0.01 ml, 0.125 mmol). The color of the solution changed from yellow red to dark red after overnight stirring. The solution was taken to dryness in vacuo. Attempted crystallization of the residue in a solution of CH$_2$Cl$_2$/hexane did not yield good quality crystals. IR (KBr, cm^{-1}): ν_{NO} = 1430; also 1496 s, 1453 s, 1375 s, 1362 w, 1284 w, 1258 w, 1223 m, 1203 w, 1159 w, 1110 s, 1091 w, 1069 w, 1032 s, 1001 m, 995 m, 966 s, 901 s, 877 w, 824 s, 795 m, 739 s, 699 s.

(TPP)(Fe)(1-MeIm)$_2$·2(1-MeIm) (**8**): A crystal of Fe(TPP)(1-MeIm)$_2$·2(1-MeIm) was obtained serendipitously as follows: To a 10 mL CH$_2$Cl$_2$ solution of (TPP)FeCl (0.010 g, 0.014 mmol) was added *N*-hydroxyamphetamine (0.07 g, 0.05 mmol) and 1-MeIm (0.05 ml, 0.6 mmol). After 6 hours of reaction, the solution was dried under reduced pressure. The red purple residue was re-dissolved in CH$_2$Cl$_2$, and an equal volume of hexane was added. Red plate-shaped crystals grew from the slow evaporation of this mixture in the glove box. The isolated yield of crystals is 50%.

(TPP)Co(NHOHCH(CH$_3$)CH$_2$Ph) (**9**): Excess *N*-hydroxyamphetamine (0.03 g, 0.2 mmol) was added into a stirred CH$_2$Cl$_2$ solution of (TPP)CoCl (0.015 g, 0.02 mmol). The solution changed from red purple to an orange color after an overnight reaction. The product was taken to dryness in vacuo and the residue was washed with methanol. The slow evaporation of a CH$_2$Cl$_2$/hexane (2:1) solution of the residue in the glove box

resulted in the formation of cubic brown crystals within one week. The yield is 55% as estimated from ^{1}H NMR spectroscopy. ^{1}H NMR (CDCl$_3$): 15.60 (b, 8, pyrrole H of TPP), 12.73 (b, 8, *o*-H of phenyl group), 9.78 (m, *p*-H of phenyl group), 9.55 (m, *m*-H of phenyl group), 9.12~8.91 (d, pyrrole H of TPP), 8.16 (m, *o*-H of phenyl group), 7.77 (m, *p, m*-H of TPP), -0.92 (b, CH$_2$), -2.70 (b, CH$_3$), -4.61 (b, CH), -5.60 (b, NH).

2.3 Results and discussion

2.3.1 Synthesis

Our research group previously reported the preparation and characterization of some iron porphyrin nitrosoarene/alkane complexes. They were prepared via one of two main methods as shown in eqs. 2.1 and 2.2. The first method involves the direct coordination of the nitrosoarene ligand to the ferrous center in the metalloporphyrin (Eq. 2.1).

$$\text{Fe}^{II} \quad + \quad 2\text{PhNO} \quad \longrightarrow \quad \text{Fe}^{II} \qquad \textbf{(2.1)}$$

$$\text{Fe}^{III}\text{Cl} \quad + \quad i\text{-PrNHOH} \quad \xrightarrow{\ \text{MeOH}\ } \quad \text{Fe}^{II} \qquad \textbf{(2.2)}$$
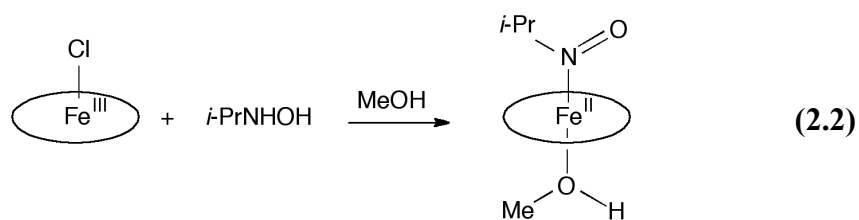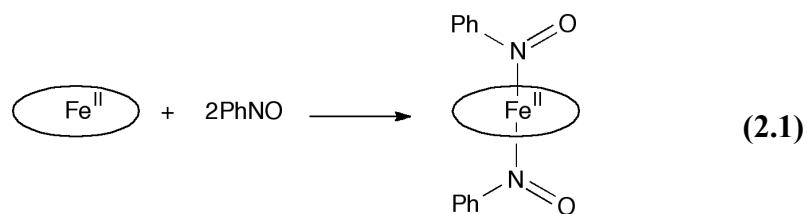
The second method involves a redox reaction between a ferric porphyrin and an alkylhydroxylamine (Eq. 2.2); the ferric center is reduced by the ligand, and the ligand is oxidized in the process to the nitroso derivative that binds to the metal. Since the alkylhydroxylamine oxidation is formally a two-electron oxidation, it is not surprising that the yield of the product is not quantitative; as there are other minor uncharacterized products from the reaction.

In my desire to prepare the previously unreported nitrosoamphetamine derivatives of iron porphyrins, I noted that the "free" nitrosoamphetamine ligand is unstable towards tautomerization to the oxime (Eq. 2.3).

$$
\underset{\underset{H}{|}}{\overset{\overset{Me}{|}}{PhCH_2-C-N=O}} \longrightarrow PhCH_2-\overset{\overset{Me}{|}}{C}=N-OH \qquad \textbf{(2.3)}
$$
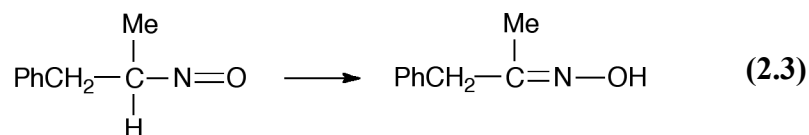
Consequently, it was impractical for me to attempt to utilize the first preparative method for the synthesis of the Fe-nitrosoamphetamine complexes. Utilization of the second preparative method (Eq. 2.1) in CH_2Cl_2 at room temperature provided the target complexes.

(2.4)
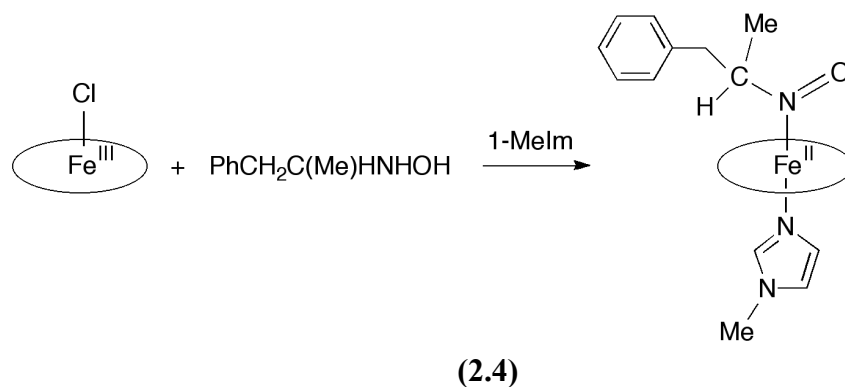
In the case of the representative compound **1** (Eq. 2.4; where por = OEP), the reaction in the presence of 1-methylimidazole proceeded over a 6-12 hour period during which time the color of the solutions due to the precursor (por)FeCl changed to a black-purple color. Work-up of the product resulted in its isolation in ~58% yield. I was unable to characterize any side-product of this reaction despite several attempts to do so. When the reaction was carried in the presence of methanol (in place of 1-MeIm), a product tentatively formulated, based on its IR spectrum, as the (OEP)Fe(NOAmph)(MeOH) was obtained. In the absence of any secondary axial ligand, I had hoped to generate and crystallize the bis-nitrosoAmph derivative. A product was obtained that could be formulated as the anticipated target compound (based in IR spectroscopy). However, I was not successful in crystallizing it for a structural study.

Fortunately, when the *p*-methoxy-substituted porphyrin (por = T(*p*-OMe)PP) was utilized for the reaction of the ferric precursor with the *N*-hydroxyamphetamine reagent, I was able to generate and isolate the final bis-nitrosoamphetamine product shown in eq. 2.5. It is likely, based on the results from related reactions (see below), that the initial product is the six-coordinate nitroso/hydroxylamine-coordinated complex shown at top right of eq. 2.5. However, I was not able to isolate this intermediate compound, but I note that the final crystalline product isolated in 35% yield was obtained after crystallization in air.
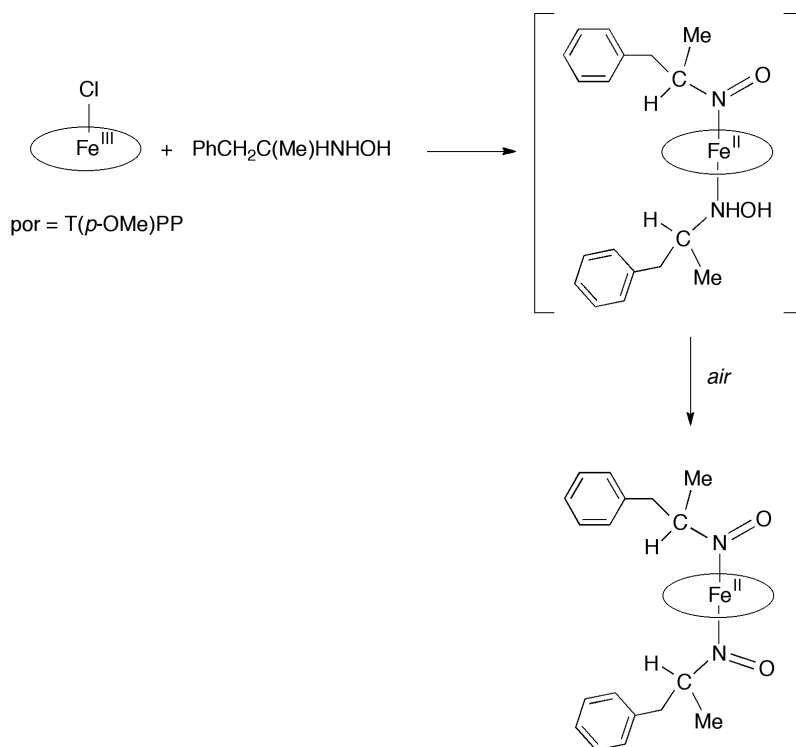
(2.5)

I was surprised that I could also obtain a crystalline sample as shown by X-ray crystallography to be a mixture of the six-coordinate product of eq. 2.5 and its 5-coordinate partner (namely with only one coordinated nitrosoAmph ligand). It is likely that very minor differences in the crystallization/experimental conditions provided this new crystal structure; I discuss this in more detail in the section on crystallography.

When the parent tetraphenylporphyrin macrocycle (por = TPP) is used for the reaction described in eq. 2.4 (i.e., in the presence of 1-MeIm), I was able to obtain the TPP analogue of the product. Curiously, when the same reaction was performed with a large excess of 1-MeIm, I obtained, after workup of the product mixture, crystals of the ferrous bis-imidazole compound (TPP)Fe(1-MeIm)$_2$.

22

It is interesting to note that in the absence of the added 1-MeIm as axial base, I obtained and successfully isolated the nitrosoAmph/hydroxylamineAmph product that had eluded me in the earlier T(*p*-OMe)PP attempts (i.e., eq. 2.6).
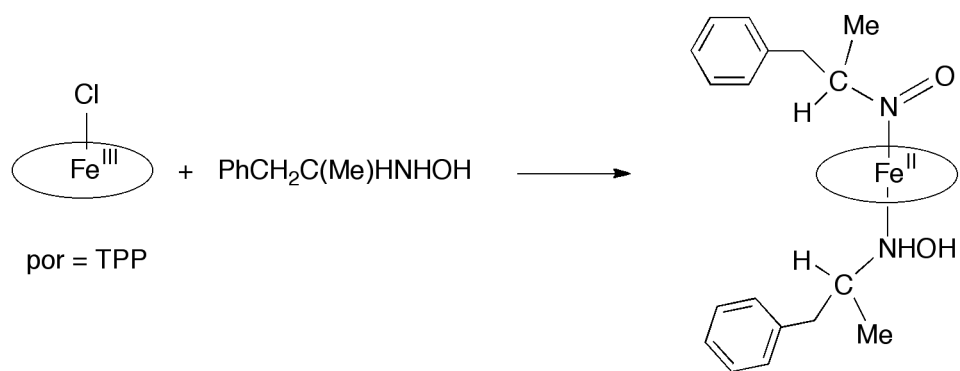
(2.6)

Cobalt(III) is isoelectronic with ferrous Fe(II). I was thus curious whether the d^6 Co(III) ion would be able to oxidize the AmphNHOH ligand in the same way as the d^5 Fe(III) ion did to form the NOAmph derivative. In the reaction between AmphNHOH with a Co(III) porphyrin, I saw no evidence for coordinated NOAmph in the products, although reduction to the Co(II) species (with or without AmphNHOH) did occur (eq. 2.7), as determined by UV-vis spectroscopy and by X-ray crystallography (see later). The (TPP)Co(AmphNHOH) complex was unstable in air, as determined by UV-vis and ^{1}H NMR spectroscopy.

Me
|
C
H— —NHOH

Co^{II}

Cl
|
Co^{III} + PhCH$_2$C(Me)HNHOH $\longrightarrow$ and/or

por = TPP

Co^{II}

(2.7)
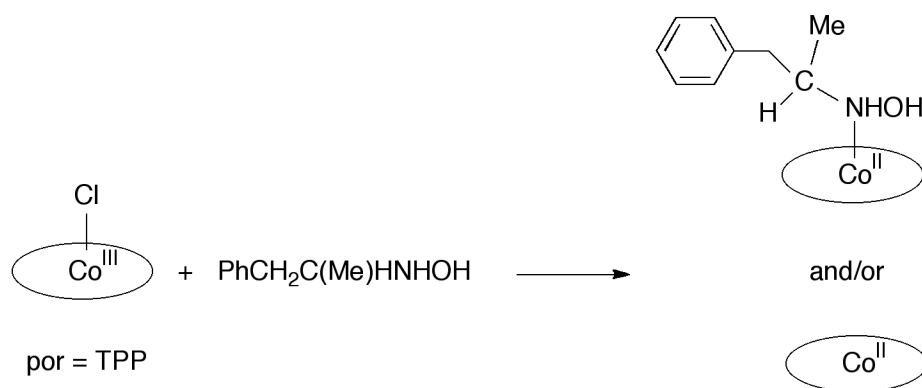
2.3.2 Spectroscopy

The organic nitroso moiety in the generated R-N=O ligand renders itself amenable to vibrational spectroscopic analysis. In general, such NO vibrations (υ_{NO}) occur in the 1300 cm^{-1} ~1500 cm^{-1} range for metal-coordinated nitrosoalkanes. This spectral range is normally unobstructed by porphyrin macrocycle vibrations, although on occasion the NO vibrations overlap with porphyrin bands.

In general, the υ_{NO}'s of the iron-coordinated nitrosoamphetamine complexes obtained in this chapter fall into the 1510-1410 cm^{-1} range. The υ_{NO} of the (OEP)Fe(NOAmph)(1-MeIm) (**1**) complex as a KBr pellet occurs at 1419 cm^{-1} (Figure 2.1, *bottom*) which is close to the υ_{NO}'s of 1423 cm^{-1} reported for a related secondary nitrosoalkane complex (OEP)Fe(*i*-PrNO)(1-MeIm) reported previously from our laboratory.
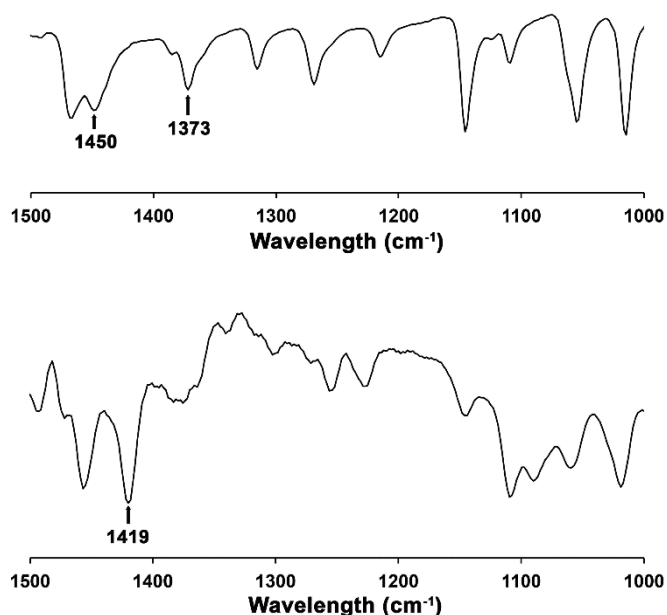
Figure 2.1. IR spectra of the precursor (OEP)FeCl (*top*) and the (OEP)Fe(NOAmph)(1-MeIm) product (**1**: *bottom*) as KBr pellets.

Selected chemical drawings from my work and their associated υ_{NO}'s are presented in Figure 2.2. When the axial 1-MeIm ligand of **1** is replaced with MeOH, the υ_{NO} shifts upward to 1425 cm^{-1}, a feature indicative of the greater electron donation to the iron center by 1-MeIm compared with the solvent MeOH. The lower overall electron donation by the axial MeOH ligand reduces the electron density at the metal center, which in turn, reduces the metal-to-RNO backbonding into the π^* orbital of the nitroso moiety, thus strengthening this bond and raising its υ_{NO}. This 1-MeIm and MeOH comparison is consistent with that observed for the *i*-PrNO analogue as well.

Interestingly, when the *β*-octasubstituted OEP porphyrin macrocyle is replaced with the less electron-rich *meso*-tetrasubstituted TPP macrocycle, the υ_{NO}'s of the NOAmph ligand also increases from 1419 cm^{-1} in (OEP)Fe(NOAmph)(1-MeIm) (**1**) to

1430 cm^{-1} in (TPP)Fe(NOAmph)(1-MeIm) (**7**; not shown in Figure 2.2), again indicative of a lower metal-to-ligand back-donation in the case of the TPP analogue.
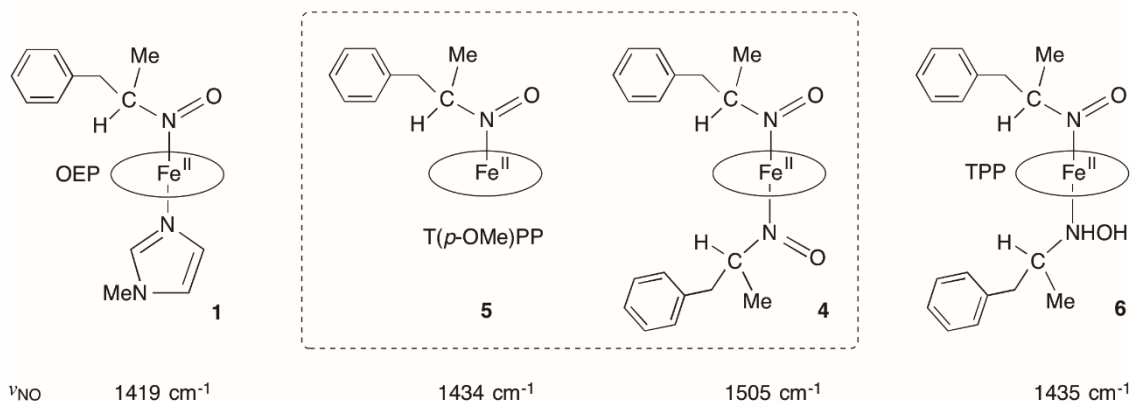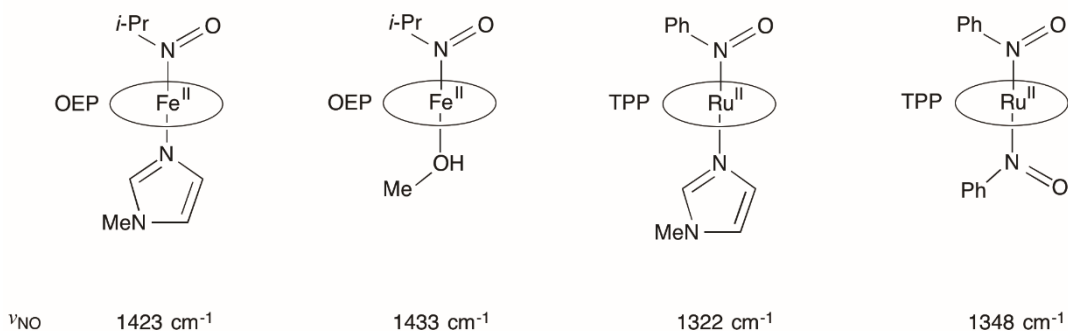
Figure 2.2. Chemical drawings of selected product complexes and their IR υ_{NO} bands.

I also note that replacement of the 1-MeIm ligand in **7** with the *N*-hydroxylamphetamine ligand (i.e., compound **6** in Figure 2.2) results in a further increase of the υ_{NO} by 5 cm^{-1}, suggesting that the 1-MeIm ligand is an overall better electron-donor that the RNHOH moiety. In fact, this observation is consistent with the fact that the mixed ligand RNO/RNHOH complex is not isolated from any of the reactions when 1-MeIm was present in the reaction mixture.

Although I was able to obtain crystalline samples of the bis-NOAmph compound **4** (por = T(p-OMe)PP), I was fortunate to also obtain one such sample that contained a mixture of the five-coordinate (T(p-OMe)PP)Fe(NOAmph) (**5**) and the six-coordinate **4** (see middle boxed area in Figure 2.2). *Importantly, the structure of 5 represents the very first reported five-coordinate iron porphyrin nitrosoalkane/arene complex for any porphyrin in the literature.* The large differences in the observed υ_{NO}'s of the five-coordinate **5** (1434 cm^{-1}) and the six-coordinate **4** (1505 cm^{-1}) is attributed to the π acidity of RNO ligands due to the electronegativity of the "NO" moiety as well as the availability of the π^* orbital in this moiety that can accept electron density from the metal. Thus, placing two π-acid RNO ligands in a mutually *trans* position effectively reduces the electron density at the metal center, with a resulting decreased back donation into the RNO π^* orbitals, thus significantly raising υ_{NO}. But why is there such a large υ_{NO} difference of 71 cm^{-1} in the case of the mono-NOAmph complex **5** vs. the bis-NOAmph complex **4**, whereas there is a smaller $\Delta\upsilon_{NO}$ of 26 cm^{-1} when comparing the mono-PhNO vs. bis-PhNO in the Ru derivatives shown at bottom of Figure 2.2. I believe that the answer lies in the orientations of the axial ligand planes; this is discussed further in the section on the X-ray crystal structures.

The iron nitrosoamphetamine complexes obtained in this chapter contain π-acid RNO moieties that are in strong analogy to carbon monoxide (CO), thus are at the high end of the spectrochemical series. It is therefore not surprising that they end up being low-spin ferrous d^6 compounds, hence are diamagnetic and readily amenable to ^{1}H NMR spectroscopic characterization. Many of the compounds I attempted to obtain throughout my studies with the amphetamine derivatives ended up not being very pure,

as judged by ^{1}H NMR spectroscopy. Consequently, I focused on additional purifications using crystallization of the target compounds, and then redissolving those crystals in deuterated chloroform for the ^{1}H NMR spectroscopic work. The ^{1}H NMR spectroscopic data for representative example, namely for **1**, is shown in Figure 2.3. The spectrum of this compound, as with the spectra of the others, displayed characteristic peaks for the porphyrin macrocycles (in the boxed area of Figure 2.3), thus we will not discuss these macrocycle proton peaks further.
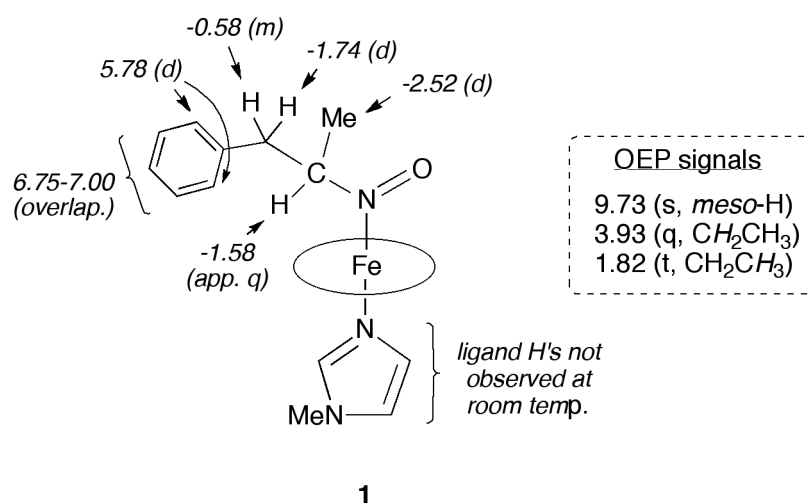
Figure 2.3. Sketch of compound **1** and its associated ^{1}H NMR spectroscopic data.

Two important features stand out from Figure 2.3. First, the ^{1}H NMR signals between the nitroso and phenyl groups of the coordinated NOAmph ligand are upfield from the "normal" 0-10 ppm range for diamagnetic complexes. This is attributed to the ring current effect of the aromatic porphyrin macrocycle. In fact, similar upfield shift of ^{1}H NMR spectral peaks have been noted for other complexes such as (por)Rh(R) and (por)Co(*t*-Bu) (see Chapter 4).

Another interesting observation is that the ^{1}H NMR spectral signals for the axial 1-MeIm ligand are not discernable in the room temperature (~20 °C) spectra, but become readily discernable at lower temperatures (e.g., at -40 °C). This is likely due to a fast equilibrium between the coordinated and uncoordinated 1-MeIm at room temperature that broadens the peaks such that they are not readily observed. Cooling down the ^{1}H NMR sample stabilizes the six-coordinate form and allows the observation of the 1-MeIm signals. A similar phenomenon has been previously reported by a former group member during her work with the (por)Fe(^{i}PrNO)(1-MeIm) complexes.[11]

The ^{1}H NMR spectrum of the complex mixture **5/4** (namely (T(*p*-OMe)PP)Fe(NOAmph) + (T(*p*-OMe)PP)Fe(NOAmph)$_2$; boxed area in Figure 2.2) was quite interesting. Although we determined, by X-ray crystallography, that there were two compounds in this mixture, the solution ^{1}H NMR spectrum at room temperature appeared to show the presence of only one species, namely that of the five-coordinate 5. This observation is, however, consistent with what I saw for the six-coordinate 1-MeIm compounds described in the previous paragraph, that the ^{1}H NMR signals for the sixth axial ligand were not observable at room temperature in solution. To ensure that our assignments of the ^{1}H NMR peaks for the NOAmph ligands were indeed correct in this complex mixture **5/4** (namely (T(*p*-OMe)PP)Fe(NOAmph) + (T(*p*-OMe)PP)Fe(NOAmph)$_2$; boxed area in Figure 2.2), I embarked on 2D ^{1}H NMR spectroscopy in collaboration with Dr. Susan Nimmo. The COSY and HSQCAD spectra are shown in Figures 2.4-2.6.
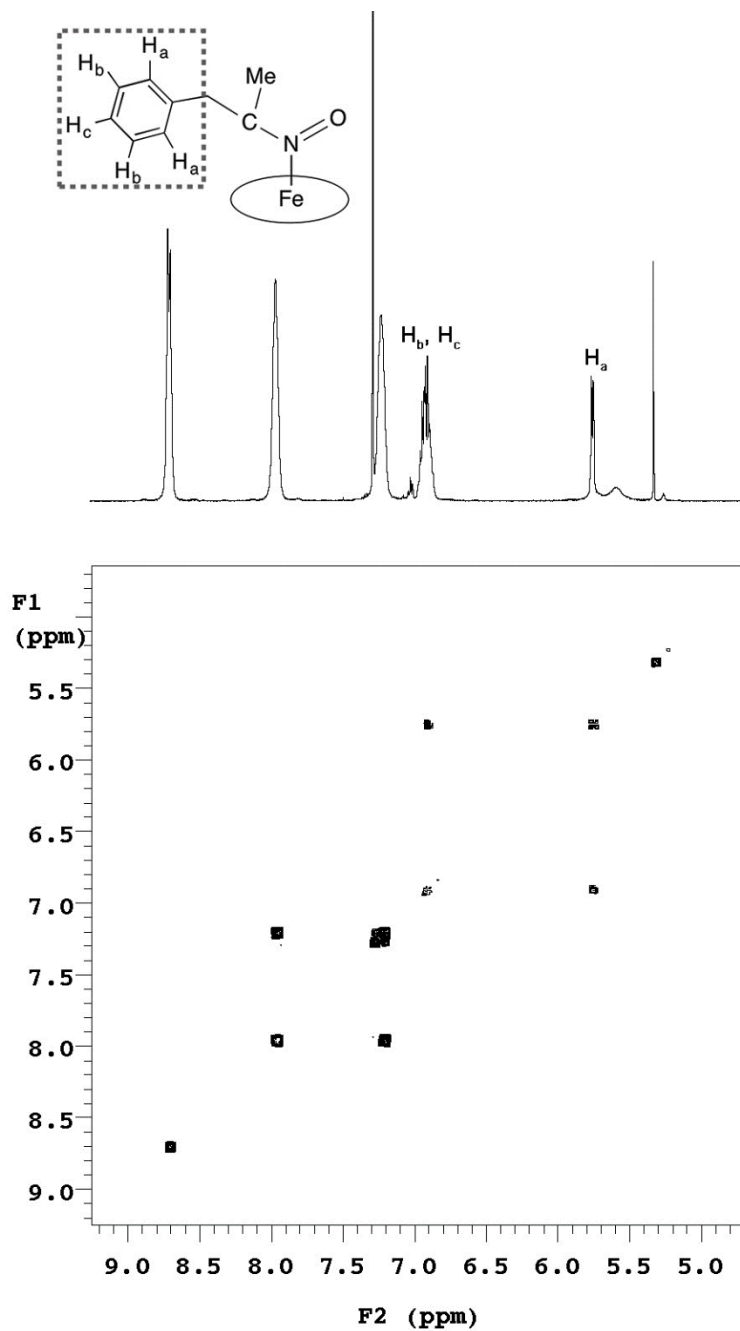
Figure 2.4. The COSY spectrum of the (T(*p*-OMe)PP)Fe(NOAmph) + (T(*p*-OMe)PP)Fe(NOAmph)$_2$ complex mixture in CDCl$_3$ at normal room temperature.
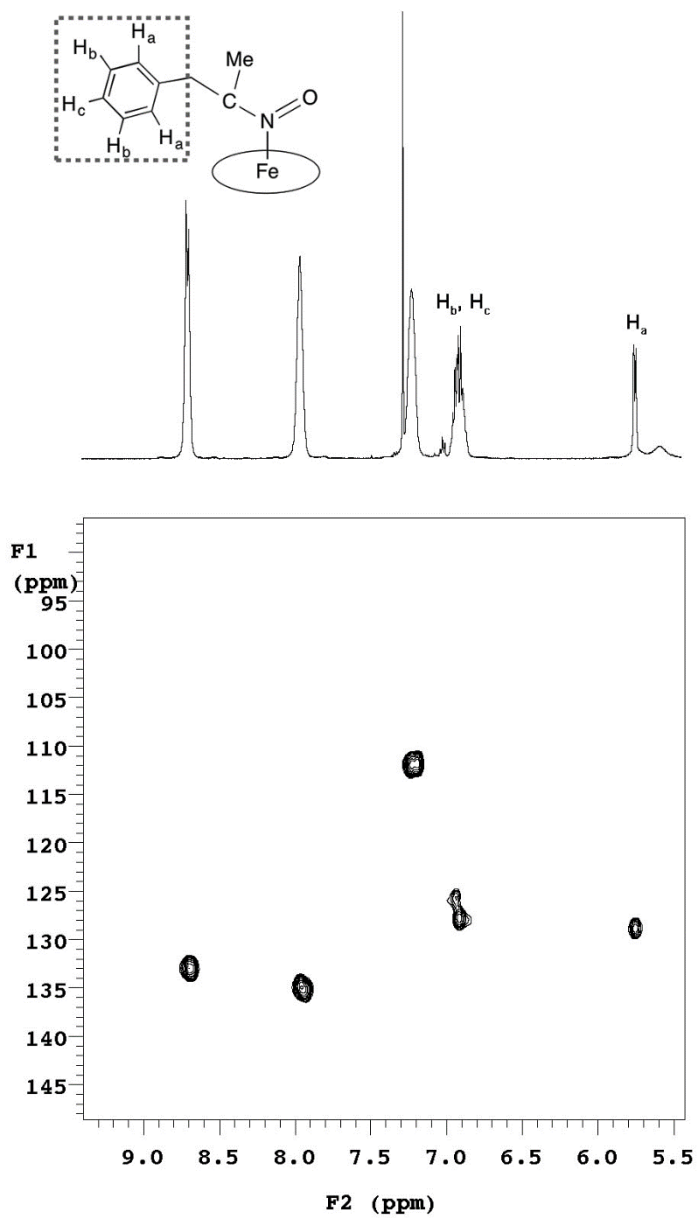
Figure 2.5. The HSQCAD spectrum of the (T(*p*-OMe)PP)Fe(NOAmph) + (T(*p*-OMe)PP)Fe(NOAmph)$_2$ complex mixture in CDCl$_3$ at normal room temperature.
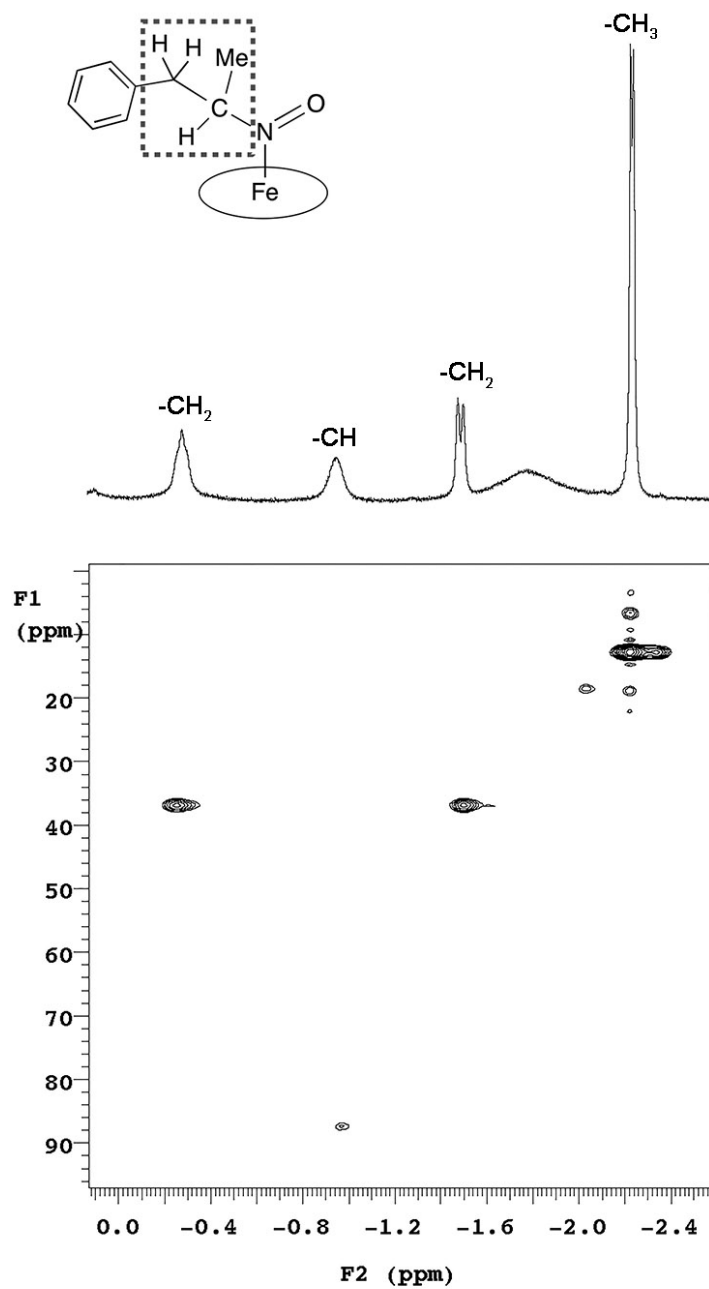
Figure 2.6. The HSQCAD spectrum of the (T(*p*-OMe)PP)Fe(NOAmph) + (T(*p*-OMe)PP)Fe(NOAmph)₂ complex mixture in CDCl₃ at normal room temperature.

In the COSY spectrum (Figure 2.4), a coupling interaction between the proton signals at 6.93, 5.77 and 5.61 ppm (the latter two overlapping in the 1D spectrum) was observed, which corresponds to the coupling of the *o*-H, and *p,m*-H of the phenyl group of the NOAmph ligand and confirms their assignment. The two HSQCAD spectra shown differ in the ppm ranges in the horizontal (^{1}H) and vertical (^{13}C) axes. The HSQCAD spectrum in Figure 2.5 shows the signals in the range of 5.0 ppm to 9.0 ppm that are assigned to the porphyrin macrocycle and the phenyl group of the ligand. The 2D NMR spectrum indicated that the signal at 6.93 ppm and 5.77 ppm belong to the protons on the phenyl group of the ligand.

The HSQCAD spectrum focusing on the 0 ppm to -2.5 ppm range is shown in Figure 2.6. I had initially assigned, from the 1D NMR spectrum, the triplet at -0.28 ppm and the doublet at -1.50 ppm to the protons of the methylene (*β*-carbon) group. In this 2D experiment, I confirmed that these two protons were bonded to the same carbon atom (at 37.1 ppm in the ^{13}C NMR spectrum). The ^{1}H NMR signal at -2.21 ppm is assigned to the methyl H group on the *α*-C atom, and this correlates with the ^{13}C signal of this *α*-C at 13.06 ppm. A ^{1}H NMR signal at -0.93 ppm is assigned to the H on the *α*-C atom, and this correlates with the ^{13}C signal of the *α*-C at 88 pm; this ^{13}C downfield shift is normal for *C*-nitroso compounds even without the metal.[31] Importantly, what was clear from the 1D and the 2D NMR spectra was the apparent 1:1 integration ratio of the NOAmph ^{1}H signals to the porphyrin macrocycle. Similar to that observed in the 1-MeIm six-coordinated derivatives, when the 1D NMR spectrum of the **5/4** mixture is collected at lower temperatures, additional signals at -0.6 (d), -1.7 (s), and -2.02 (s) ppm become apparent; this observation likely due to the stabilization of the six-coordinate **4**

at lower temperatures. However, we were not able to definitively assign these signals in the absence of 2D spectra at these lower temperatures. In addition, the compounds were not very stable in solution, as judged by the gradual disappearance (e.g., overnight at room temperature) of the α-CH signals in the ^{1}H NMR spectra.

^{1}H NMR spectroscopy also confirmed the identity of the sixth ligand in the (TPP)Fe(NOAmph)(AmphNHOH) compound **6** (Figure 2.2). In addition to the macrocyle peaks, signals at 6.84 (s), 5.64 9s), -0.61 (br), -1.62 (d), and -2.36 (s) ppm were observed for the coordinated ligand. Furthermore, two upfield and broad peaks at 13.40 and 12.20 ppm were observed and assigned to the protons on the -NHOH moiety of the sixth AmphNHOH ligand; such peaks were not observed in any of the NOAmph complexes discussed earlier.

I mentioned earlier that the cobalt complex (TPP)Co(AmphNHOH) was unstable in air. The following UV-vis spectra illustrate this point. The addition of AmphNHOH to an aerobic (TPP)CoCl solution (λ_{max} 406 nm; not shown) led to the reduction of the Co(III) reagent to a Co(II) product, as determined by the initial generation of a typical Co(II) spectrum with a Soret band at 410 nm and a visible band at 530 nm (Figure 2.7).[25] The smaller peak at ~434 nm is due to a new Co(III) species. When 1-MeIm was added to the solution and the solution allowed to stir overnight, the band at 432 nm grew in intensity and became the dominant band in the spectrum (Figure 2.7; dashed line). This Soret band at 432 nm with visible bands at 548 and 585 nm are consistent with the aerobic formation of the known $Co^{III}(TpivPP)(1\text{-}MeIm)O_2^-$ complex reported in literature.[32]
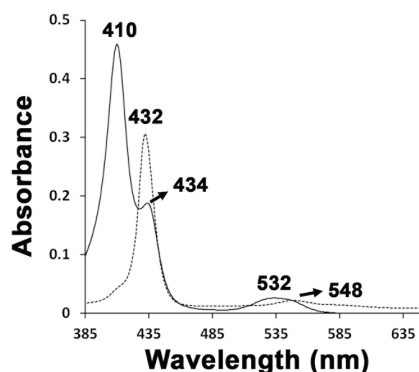
Figure 2.7. UV-vis spectra of the reaction between (TPP)CoCl and AmphNHOH in CH$_2$Cl$_2$ in air. *Solid line*: spectrum of the initial product solution. *Dashed line*: after addition of 1-MeIm and overnight stirring.

To examine further the air-sensitivity of the (TPP)Co(AmphNHOH) complex, I dissolved a few crystals (from the same batch of crystals I used for the X-ray structural characterization) in CH$_2$Cl$_2$ in air, and recorded the UV-vis spectrum (Figure 2.8). The spectrum showed immediate (after ~5 min exposure to air) oxidation of the (TPP)Co(AmphNHOH) to the Co(III) derivative (λ_{max} 431 nm). When the solution was left in air for ~8 hours, the 431 nm peak became the only prominent peak, indicating the high-yield conversion to the Co(III) product. It has been reported previously that Co(II) porphyrins are easily oxidized to a stable bis(hydroxylamine)cobalt(III) complex with the addition of hydroxylamine in air. The (TPP)Co(NH$_2$OH)$_2$ displays two bands at 427 nm and 542 nm.[33] The red-shifted Soret band from 412 nm to 431 nm in this work strongly suggests the aerobic oxidation of Co(II) to a Co(III) complex. The formation of Co(III) derivative in solution in air was also confirmed by an attempted ^{1}H NMR spectral characterization of (TPP)Co(AmphNHOH) that showed the presence of a diamagnetic Co(III) species. Due to an apparent lack of a defined anion in solution, the anion of the oxidized Co(III)

product is likely to be superoxide.   I note that a similar spectrum change was observed

previously during the introduction of O_2 into a Co(II)(TpivPP) solution in the presence

of 1-MeIm.[32]

Figure 2.8. *Solid line:* The UV-vis spectrum of a dissolved crystal of
(TPP)Co(AmphNHOH) in CH_2Cl_2 in air. *Dashed line*: After leaving the solution in air
for ~8 hrs.

2.3.3 X-ray crystallography

The metabolism of organic nitro or amine compounds involves the nitroso

and/or hydroxylamino derivatives as shown in the middle of eq. 2.8. As described in

(2.8)

the experimental section, I utilized the hydroxylamino precursor in the reactions to

isolate the ferrous NOAmph derivatives. Although the IR and NMR spectral data were

consistent with the structures proposed in Figure 2.2 (e.g., observation of a υ_{NO} for the nitroso derivative), it is important that the identities of the products and proposed binding modes of the ligands be verified by determining their three-dimensional molecular structures using X-ray crystallography. Several of the product complexes were crystallized and their solid-state crystal structures determined (Figures 2.9-2.13). The structure of (OEP)Fe(NOAmph)(1-MeIm) complex is shown in Figure 2.9 (top), and selected geometrical parameters are collected in Table 2.1. The NOAmph ligand is bound to the ferrous center via the N-atom, a feature that is consistent with our previous finding that this N-binding mode enhances stability of the complex via efficient π-backbonding from the ferrous center into the π^* orbital of the nitroso ligand. This is consistent with the slight upward displacement of the Fe atom towards the NOAmph ligand (by 0.05 Å; middle of Figure 2.9), with an Fe-N(O) bond length of 1.805(6) Å. The porphyrin macrocycle is *saddled*.[34]

We also note that since the organic NOAmph molecule is unstable towards tautomerization to the oxime form (see earlier eq. 2.3), that the binding to Fe and subsequent π-backbonding interaction stabilizes this otherwise unstable 2° RNO compound. Further evidence for the lack of tautomerization comes from the tetrahedral nature of the α-*C* atom (i.e., C32) bearing the N=O moiety (Figure 2.9); the unobserved (isomerized) oxime tautomer should have a planar α-C atom.

The axial NOAmph plane essentially bisects adjacent porphyin atoms as shown in at the bottom of Figure 2.9, with an O1-N7-Fe1-N3 torsion angle of 47°. In contrast, the 1-MeIm plane is essentially coplanar with porphyrin diagonal N-atoms (i.e., N2 and N4; not shown); the angle between the 1-MeIm plane and the nearest Fe-N(por) bond is

2°. Such axial ligand orientations have been observed previously in a few other complexes such as (OEP)Fe(*i*-PrNO)(1-MeIm).[11] The axial Fe-N(1-MeIm) bond length of 2.068 (5) Å is similar to those determined for other ferrous-imidazole porphyrin complexes.
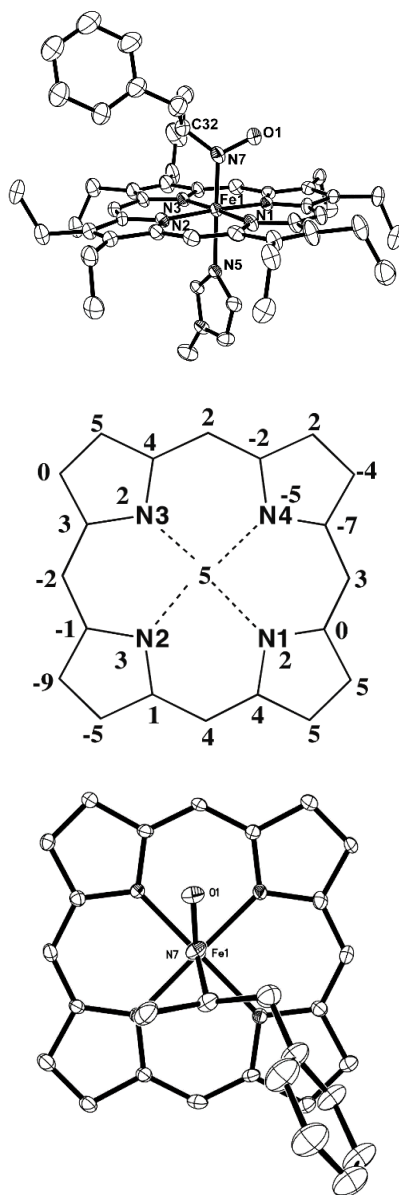
Figure 2.9. (a) Molecular structure of (OEP)Fe(NOAmph)(1-MeIm). The minor disordered components of the NOAmph ligand (~18%) are not shown. Hydrogen atoms have been omitted for clarity. (b) Perpendicular atom displacements (in units of 0.01 Å) of the porphyrin core from the 24-atom mean porphyrin plane. (c) Top view from RNO ligand side. The phenyl groups and 1-MeIm ligand are omitted for clarity.

38

Table 2.1. Selected bond lengths (Å) and angles (°) for synthetic (por)Fe(RNO)(L), (por)Fe(RNHOH)(L), (por)Co(RNHOH) and related complexes.

Compound	N-O	N(O)-Metal	Metal-L(ax)	Fe-N_p	Metal-N-O	Δ_{N4}Metal	Ref
Fe(OEP)(ONCH(CH$_3$)CH$_2$Ph)(1-MeIm) (**1**)	1.320(8) 1.325(8)[a]	1.805(6)	2.068(5)	1.999	120.1(5) 119.1(13)[a]	5	This work
Fe(T(pOMe)PP)(ONCH(CH$_3$)CH$_2$Ph)$_2$ (**4**)	1.242(3)	1.955(2)		2.005	119.45(19)	0	This work
Fe(TPP)(ONCH(CH$_3$)CH$_2$Ph) (OHNHCH(CH$_3$)CH$_2$Ph) (**6**)	1.284(2), 1.307(4)[a] 1.432(2)[b]	1.8226(17) 2.1405(17)	2.141	1.996	121.96(14) 113.8(4)[a] 116.53(11)[b]	4	This work
Fe(T(pOMe)PP)(ONCH(CH$_3$)CH$_2$Ph)$_2$/ Fe(T(p-OMe)PP)(ONCH(CH$_3$)CH$_2$Ph) (**5**)	1.245(4)	1.953(3)		2.006	119.5(2)	4	This work
Co(TPP)(OHNHCH(CH$_3$)CH$_2$Ph) (**9**)	1.451(2)	2.193(19)		1.979	114.98(12)	13	This work
(OEP)Fe(^{i}PrNO)(1-MeIm)	1.26(2)	1.80(1)	2.03(1) 2.11(2)[a]		123(1)		11
(TPP)Fe(^{i}PrNO)(1-MeIm)	1.24(1)	1.81(1)	2.05(1)		122(1)		11
(TTP) Fe(^{i}PrNO)(1-MeIm)	1.25(1), 1.28(1)	1.81(1), 1.86(1)	2.05(1), 2.03(1)		123(1) 121(1)		11

Δ_{N4}Metal: Displacement of Fe/Co from the porphyrin 4N mean plane
a. data from the disordered component;   b. two axial ligands in the molecule

The Ph moiety of the NOAmph ligand is oriented near-perpendicular at 73° to the porphyrin macrocycle. It is important to note that our complementary DFT calculations show two stable orientations of this Ph group, one near-perpendicular to the porphyrin macrocyle and one near-parallel as seen for the AmphNHOH derivatives in this work (see later). Importantly, Figures 2.9-2.12 represent the first reported crystal structures containing the biologically relevant NOAmph ligand.

The molecular structure of the bis-nitroso compound (T(p-OMe)PP)Fe(NOAmph)$_2$ (Figure 2.10) offers a nice comparison with that of (OEP)Fe(NOAmph)(1-MeIm) described above. The (T(p-OMe)PP)Fe(NOAmph)$_2$ structure is the first bis-nitrosoalkane porphyrin structure to be reported. In general, the NOAmph ligand conformation is similar to that observed in (OEP)Fe(NOAmph)(1-MeIm). The mutually *trans* π-accepting NOAmph ligands result, not too surprisingly, in weaker and longer Fe-N(axial) bonds (e.g., 1.955(2) Å in (T(p-OMe)PP)Fe(NOAmph)$_2$ (Table 2.1). Consistent with this observation is the shorter nitroso N=O bond length of 1.242(3) Å in the bis-NOAmph derivative where the Fe center is less electron rich due to both axial ligands being electron-withdrawing, resulting in less π-backbonding from Fe to the NO π* orbitals. This is also consistent with the IR spectroscopic data, namely a higher υ_{NO} for this bis-nitroso derivative, discussed in the previous section. The porphyrin macrocycle adopts a wave-like conformation, with the nitroso CNO moiety also bisecting adjacent porphyrin N-atoms.
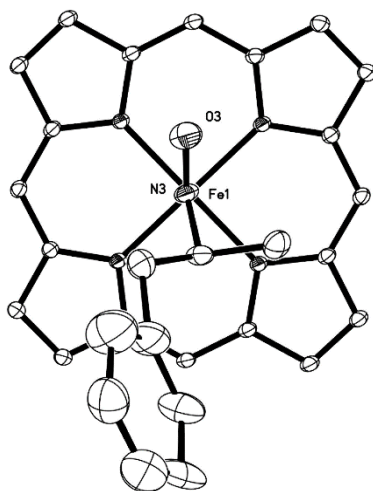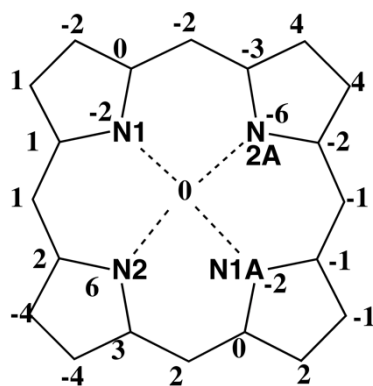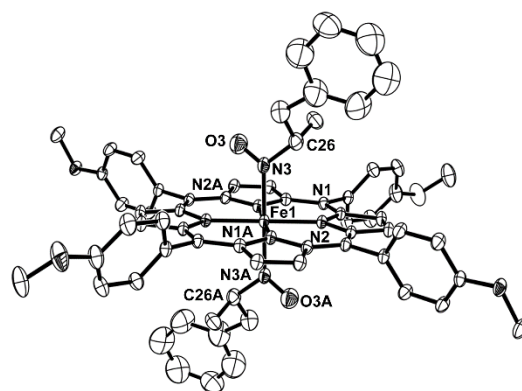
Figure 2.10. (a) Molecular structure of (T(*p*-OMe)PP)Fe(NOAmph)₂. Hydrogen atoms have been omitted for clarity. (b) Perpendicular atom displacements (in units of 0.01 Å) of the porphyrin core from the 24-atom mean porphyrin plane. (c) The top view showing the axial RNO ligand orientation. The i-methoxyphenyl and one of the NOAmph groups are omitted for clarity.

Due to the uniqueness of the bis-nitroso structure reported in Figure 2.10, namely that this was the first such bis-nitrosoalkane structure, I pursued further studies with this compound to investigate its stability both in solution and in the solid-state. As part of my detailed study, I was able to repeat the crystallization under what I felt were the identical conditions used earlier for the structure shown in Figure 2.10. To my amazement, the resulting crystalline product from what I perceived to be the same reaction and crystallization conditions yielded the "expected" six-coordinate (T(p-OMe)PP)Fe(NOAmph)$_2$. However, the occupancy of the sixth ligand, namely the second NOAmph ligand, was only ~77%, leading to the net presence of both the expected six-coordinate complex (as in Figure 2.8) as the major component (77%), and the unexpected five-coordinate (T(p-OMe)PP)Fe(NOAmph) as the minor component (23%) as shown in Figure 2.11. Obtaining this structure shown in Figure 2.11 and identifying both the five- and six-coordinate forms substantiates the view that having two NOAmph ligands *trans* to the same metal center results in a weakening of the Fe-axial ligand interaction. We were unsuccessful on attempts to obtain sufficiently accurate metrical parameters for the five-coordinate component as a separate entity to compare with the structure shown in Figure 2.10.
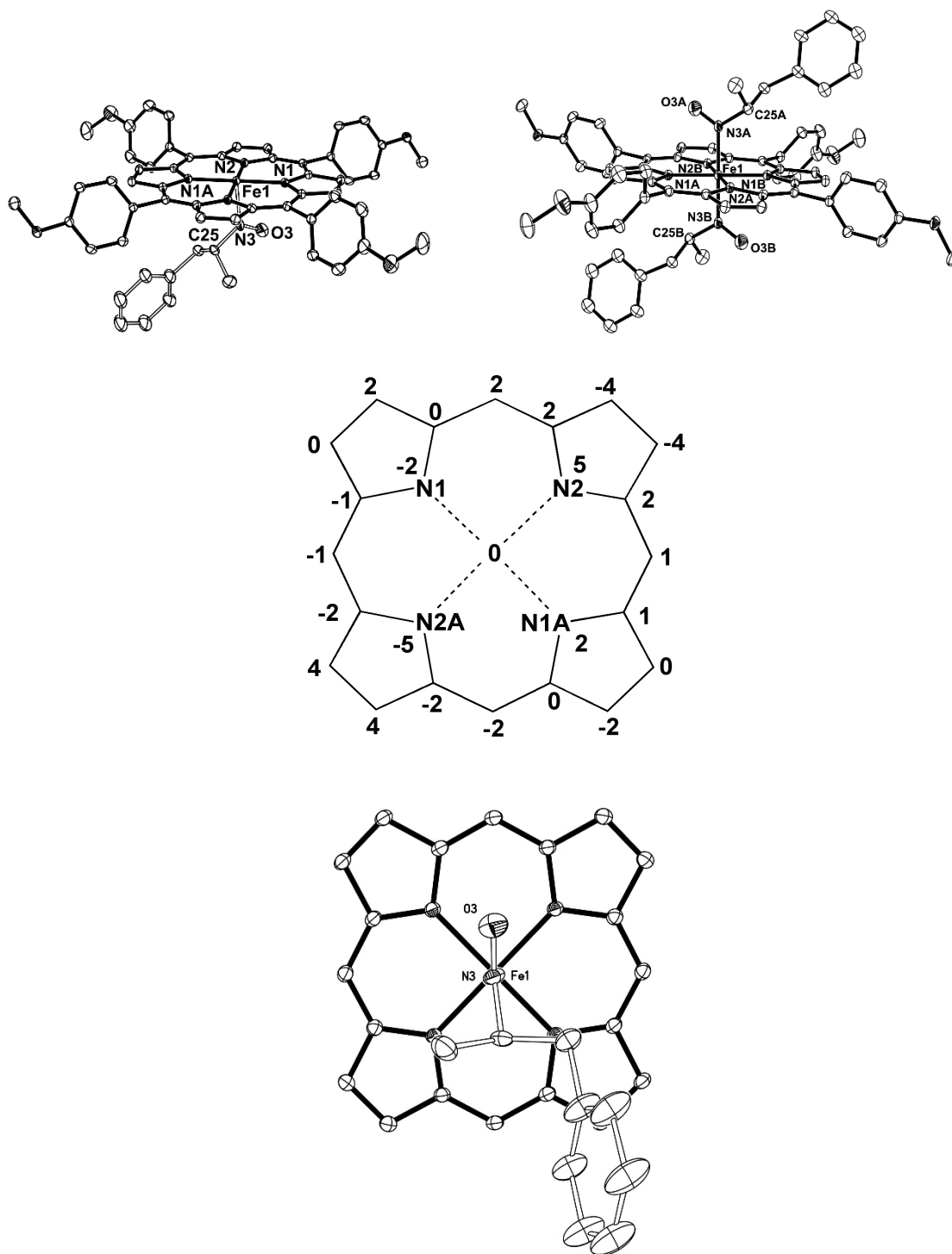
Figure 2.11 (a) Molecular structures of the five-coordinate (T(*p*-OMe)PP)Fe(NOAmph) (top left; 23%) and the six-coordinate (T(*p*-OMe)PP)Fe(NOAmph)$_2$ (top right; 77%) in the same crystal. Hydrogen atoms have been omitted for clarity. (b) Perpendicular atom displacements (in units of 0.01 Å) of the porphyrin cores from the 24-atom mean porphyrin planes. (c) The top view showing the RNO ligand orientation.

I was also fortunate to obtain suitable crystals of the mixed nitroso-hydroxylamine derivative (TPP)Fe(NOAmph)(AmphNHOH), and the crystal structure of this complex is shown in Figure 2.12. Fortunately, the hydrogen atoms on the ligand N and O atoms were located on a difference map and are indicated at the top of Figure 2.12. The nitroso Fe-N5 distance is 1.8226(17) Å, whereas the hydroxylamino Fe-N6 distance is 2.1405(17) Å. The hydroxylamino N-O formal single-bond distance of 1.432(2) Å is longer than the *trans* nitroso formal double-bond distance. These data also substantiate the formulation of this compound as a (por)Fe(RN=O)(L) species. Three observations from this structure are noteworthy. First, the hydroxylamino moiety is stabilized on the metal center by a hydrogen bond between the hydroxyl H-atom and a porphyrin N-atom, with an O···N distance of 2.963(2) Å; this probably also determines the orientation of the AmphNHOH ligand with respect to the metalloporphyin plane. I note that the porphyrin N-atom in question (i.e., N4) is apically displaced towards the AmphNHOH ligand by 0.04 Å from the porphyrin plane (middle of Figure 2.12). Second, the relative orientation of the mutually *trans* NOAmph and AmphNHOH ligands suggest that this compound may be the likely precursor to the bis-nitroso (por)Fe(NOAmph)$_2$ derivatives.   Third, the near-parallel (to the porphyrin macrocycle) orientation of the Ph group in the AmphNHOH ligand is notably different from the orientation of the Ph group in the *trans* NOAmph ligand. DFT calculations support the stability of such a relative orientation. Curiously, there are no iron porphyrin hydroxylamine crystal structures in the literature!
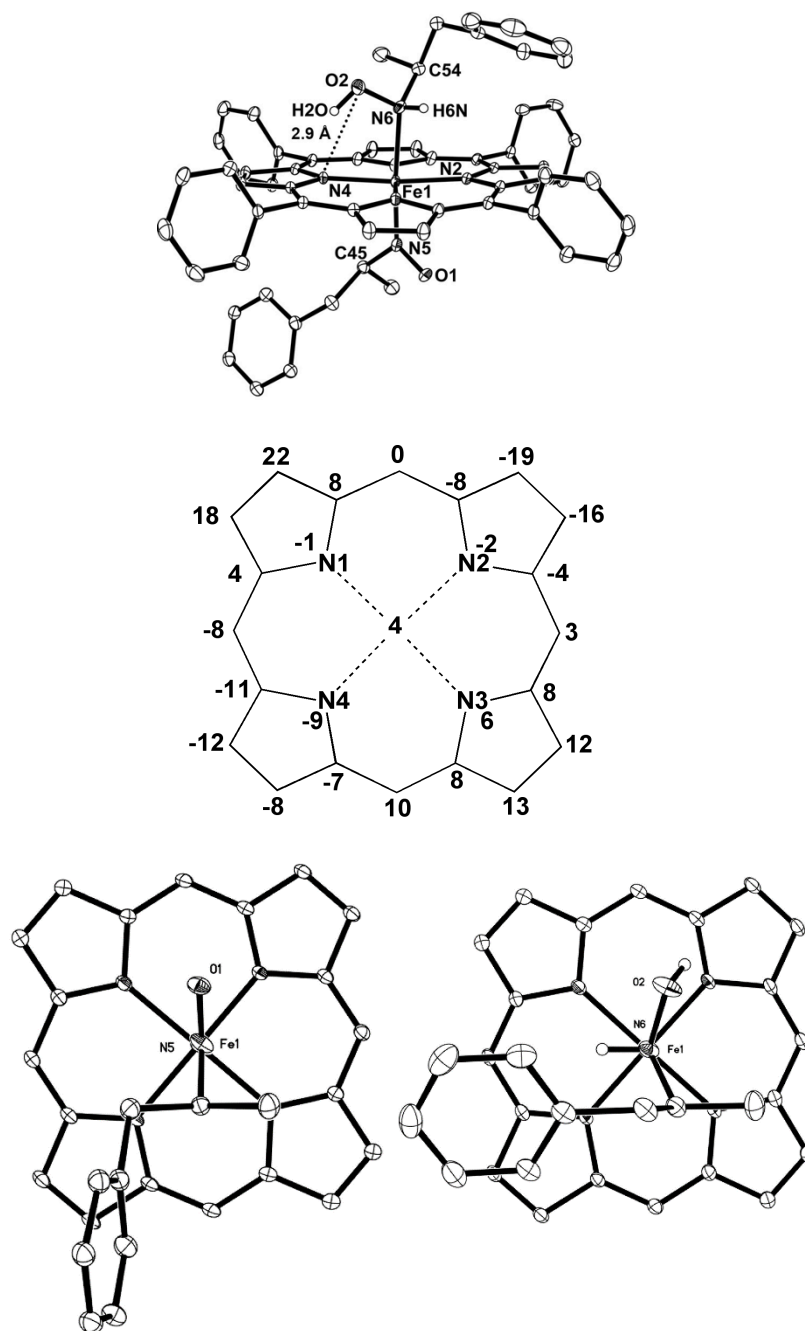
Figure 2.12. (a) Molecular structure of (TPP)Fe(NOAmph)(AmphNHOH). Hydrogen atoms have been omitted for clarity except those on the NHOH moiety. A hydrogen bond between the porphyrin N4 atom and the NOH proton (H2O) is represented by a dashed line. (b) Perpendicular atom displacements (in units of 0.01 Å) of the porphyrin core from the 24-atom mean porphyrin plane; the NOAmph ligand is closer to the reader. (c) *Left*: the top view from NOAmph side. *Right*: the top view from AmphNHOH side. The porphyrin substituents are omitted for clarity
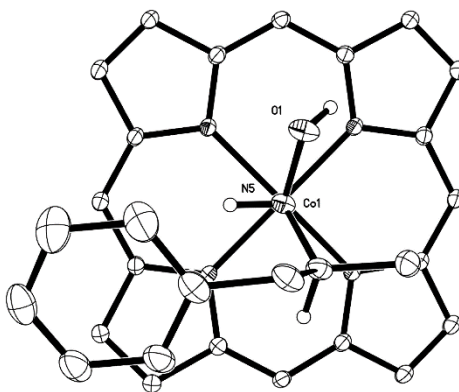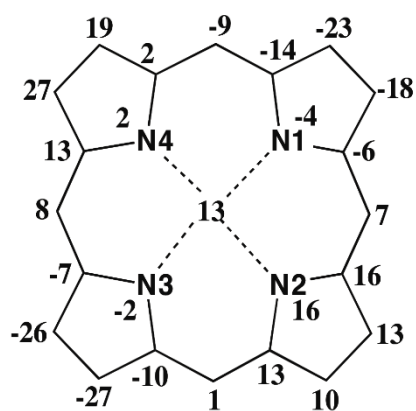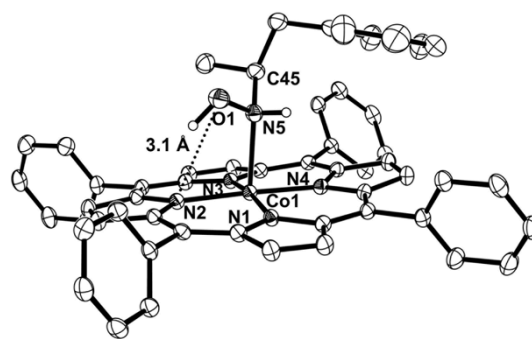
Figure 2.13 (a) Molecular structure of (TPP)Co(AmphNHOH). Hydrogen atoms have been omitted for clarity except those on the NHOH group. A hydrogen bond between the porphyrin N2 atom and the NOH proton (H1O) is represented by a dashed line. (b) Perpendicular atom displacements (in units of 0.01 Å) of the porphyrin core from the 24-atom mean porphyrin plane. (c) The top view from AmphNHOH side. The porphyrin substituents are omitted for clarity.

I extended my investigations to utilize the Co(II) ion which has one more electron in its valence shell than the ferrous Fe(II) does. My goal was to determine if the Co metal could also assist in the net formal oxidation of the AmphNHOH ligand to the nitroso NOAmph form during the binding events. The only product I was able to obtain was that containing the AmphNHOH ligand (Figure 2.13), suggesting that Fe was overall more efficient in oxidizing AmphNHOH to its nitroso NOAmph form than Co was. As noted also for the Fe case in Figure 2.12, the AmphNHOH ligand appears to be stabilized on the Co center via a H-bond to a porphyrin N-atom (top of Figure 2.13) in this significantly *ruffled* porphyrin (middle of Figure 2.13).

2.3.4 Density functional calculations

I performed DFT calculations at the B3LYP/DGDZVP level, using an unsubstituted porphine (por) ligand as the macrocycle for computational efficiency. I wanted to determine if the calculations reproduced the geometrical patterns observed in the X-ray crystal structures of the NOAmph and AmphNHOH complexes. Importantly, I also wanted to use the DFT results as a confirmatory tool for the IR υ_{NO} data and trends observed. A summary of the results is displayed in Table 2.2.

The DFT results confirmed that these complexes were minima on their potential energy curves. The N-binding of the ligands were also reproduced in accord with the structures obtained. The axial ligand orientations also matched those determined by X-ray crystallography. For example, the top view (third column of Table 2.2) of (por)Fe(NOAmph)(1-MeIm) matched that seen for the crystal structure of (OEP)Fe(NOAmph)(1-MeIm) in Figure 2.9; i.e., the observed orientation (orientation 1) in the crystal structure is a minimum energy structure. There is an alternate phenyl

orientation in the NOAmph ligand (i.e., orientation 2) as shown by the second entry in Table 2.2. Interestingly, this orientation that has the phenyl near-parallel to the porphine macrocycle is 8.6 kcal/mol *lower* in energy. So why isn't this orientation 2 observed in (OEP)Fe(NOAmph)(1-MeIm). I note that the DFT calculations were performed essentially on isolated "gas phase" molecules, whereas the crystal structure obtained embodies various degrees of crystal packing effects. These packing effects could influence the final orientation of the NOAmph ligand.

For the AmphNHOH complexs, we noted some rather unique H-bonding interactions involving the AmphNHO<u>H</u> proton and a porphyrin pyrrole N-atom (e.g., top of Figures 2.12 and 2.13). These H-bonding interactions were reproduced well by the DFT calculations as shown for the (por)Fe(AmphNHOH)(NOAmph) complex in Figure 2.14 below. It thus appears that this H-bonding interaction also determines the axial ligand orientation in these and related complexes.
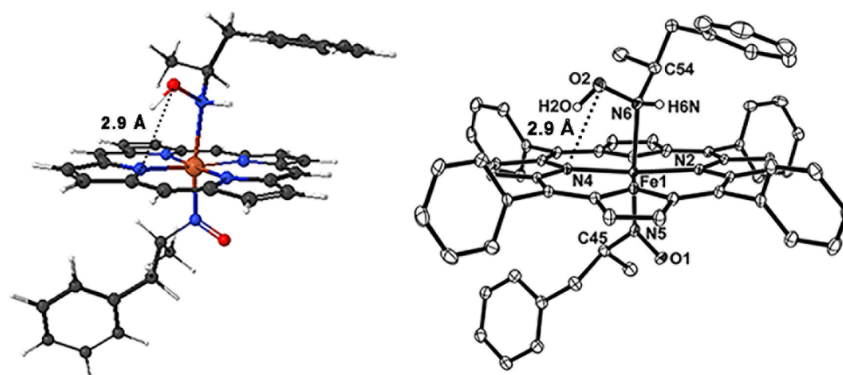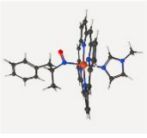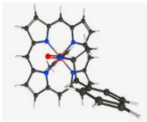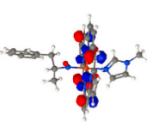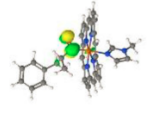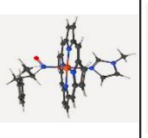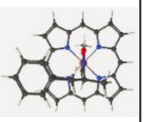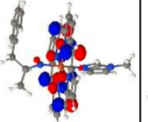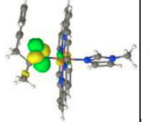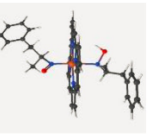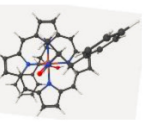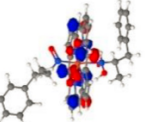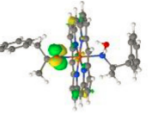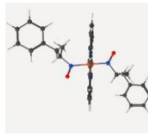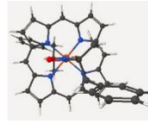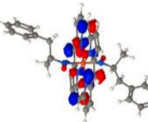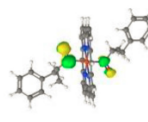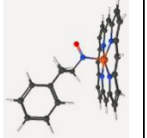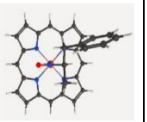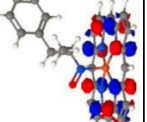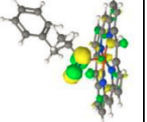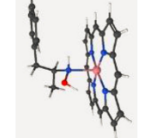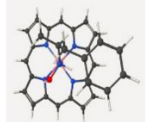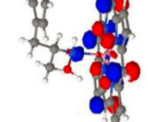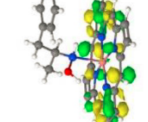
Figure 2.14. The hydrogen bonds between the porphyrin N4 atom and the NOH proton (H2O) in DFT calculation (*left*) and solid-state crystal structure (*right*) are represented by a dashed line.

Table 2.2. DFT-calculated geometries (Å) and IR υ_{NO} vibrational frequencies.

	Side view	Top view	HOMO	LUMO	M-N(O)	M-L(ax)	υ_{NO}
(por)Fe(1-MeIm)-(NOAmph)					1.914	2.082	1532
(por)Fe(1-MeIm)-(NOAmph)*					1.869	2.088	1555
(por)Fe(NOAmph)-(AmphNHOH)					1.850	2.229	1564
(por)Fe(NOAmph)$_2$					1.896	2.072	1582
(por)Fe(NOAmph)					1.781		1562
(por)Co(AmphNHOH)						2.338	

49

The highest occupied molecular orbitals (HOMOs) of these complexes are porphine based as illustrated in Table 2.2, whereas the lowest unoccupied molecular orbitals (LUMOs) of the Fe derivatives have large NO contributions consistent with the availability of the π^* orbitals on the NO fragment behaving as π-acids. The exception for this pattern on the LUMOs is that for the Co complex, which does not contain the "oxidized" π-acid NOAmph ligand, but rather the AmphNHOH ligand.

The trend in the DFT-calculated υ_{NO}s follows the experimentally observed trend, namely that for the (por)Fe(NOAmph)(L) derivatives, the trend follows the overall basicity of L being 1-MeIm (1532 cm^{-1}) < *no ligand* (1562 cm^{-1}) < AmphNHOH (1564 cm^{-1}) < NOAmph (1582 cm^{-1}).

2.3.5 Additional reactivity studies

When (OEP)Fe(NOAmph)(1-MeIm) was reacted with nitrosobenzene, the υ_{NO} due to this complex was gradually replaced by a new band at 1336 cm^{-1} (Figure 2.15).
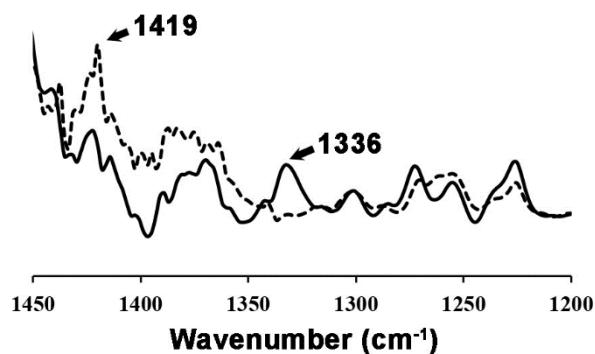
Figure 2.15. The IR spectra showing the υ_{NO} of the precursor (OEP)Fe(NOAmph)(1-meIm) at 14119 cm^{-1} (dashed line) and the υ_{NO} of the product at 1336 cm^{-1} (solid line) after reaction with 1 equiv. of PhNO after a 4 hr period.

To confirm the identity of the presumed (OEP)Fe(PhNO)(1-MeIm) product, I carried out the control reaction of (OEP)FeCl with $NaBH_4$ in CH_2Cl_2 in the presence of 1-MeIm and 2 equiv. of PhNO. The color of the solution changed from brown-black to a pink-red color after an overnight reaction. The product with a υ_{NO} of 1336 cm^{-1} was consequently assigned to the (OEP)Fe(PhNO)(1-MeIm) product; this product has also been characterized by another group member by X-ray crystallography. We thus describe the reaction by eq. 2.9.

(2.9)
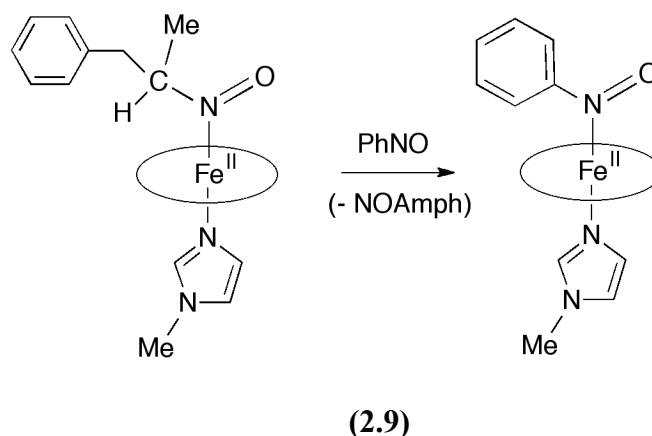
If the reaction to prepare (TPP)Fe(NOAmph)(1-MeIm) is carried out in the presence of a large excess of 1-MeIm (~10x excess), the final product obtained is the Fe(TPP)(1-MeIm)$_2$·2(1-MeIm) derivative which we characterized by X-ray crystallography. [35]

(2.10)

51
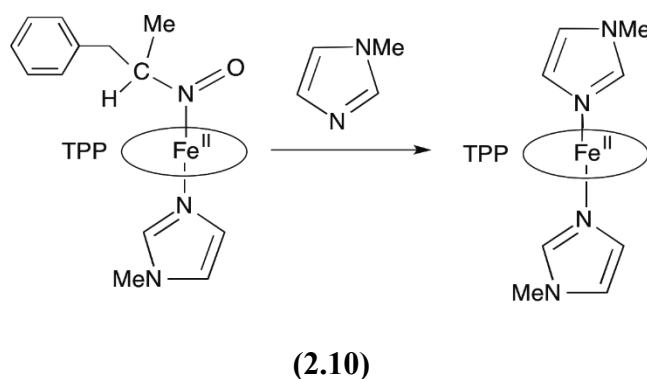
Red plate-shaped crystals of this Fe(TPP)(1-MeIm)$_2$·2(1-MeIm) product grew

from its CH$_2$Cl$_2$/hexane solution. The molecular structure of this compound is shown in

Figure 2.16. In this structure, the two 1-MeIm planes are mutually parallel. The

projection of the axial ligand has a dihedral angle of 28° with the closest Fe-Np bond.
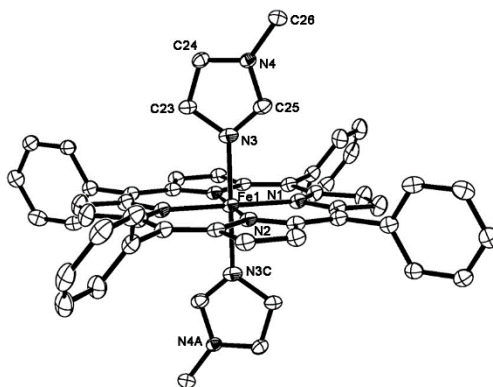
Figure 2.16. Molecular structure of (TPP)Fe(1-MeIm)$_2$. Hydrogen atoms and the two uncoordinated 1-MeIm molecules have been omitted for clarity.

I note that although ferrous (por)Fe(imidazole)$_2$ species are excellent structural

models for the reduced cytochromes utilized in biological electron-transfer reactions,[24]

this is only the third ferrous (por)Fe(imidazole)$_2$ structure ever to have been reported in

the literature.[36,37]

In this work, I successfully synthesized a series of NOAmph bound iron

porphyrins complexes from the reactions between AmphNHOH and iron porphyrins in

the presence or absence of organic bases. Selected complexes have been structurally

characterized. We have obtained the first crystal structure of an amphetamine derivative

of an iron porphyrin ((OEP)Fe(NOAmph)(1-MeIm)). We also successfully obtained the

first crystal structure of a bis-nitrosoalkane coordinated iron porphyrin ((T(*p*-

OMe)PP)Fe(NOAmph)$_2$). Unexpectedly, one of the crystal structures of showed the

presence of both (T(p-OMe)PP)Fe(NOAmph)$_2$ (major) and the five-coordinate (T(p-OMe)PP)Fe(NOAmph) (minor) in the crystal. Furthermore, from a study of the reaction of AmphNHOH with (TPP)FeCl, we obtained the first crystal structure of a hydroxylamine (NHOH) coordinated iron porphyrin complex. An unexpected hydrogen bond was observed between the hydroxyl H-atom on the ligand and a porphyrin N-atom, which helped stabilize the hydroxylamino moiety and could possibly involve in the *H*-abstraction process to form the NOAmph derivative.

We also extended our investigations to the reaction of AmphNHOH with (TPP)CoCl. A single crystal of the five-coordinated (TPP)Co(AmphNHOH) was isolated from the product, and the structure showed a similar H-binding to that observed in the structure of (TPP)Fe(AmphNHOH). The reaction of AmphNHOH with (Por)Co(III) was further studied by UV-vis spectroscopy. The stabilities and reactivities of selected NOAmph binding metal porphyrins have also been investigated and are reported. Our structural and spectroscopic studies on the NOAmph binding heme model complexes will not only fill in the gap of *C*-nitroso compounds coordination chemistry, but will also help to understand the reactivity of amphetamine derivatives in heme proteins.

2.3.6 References

(1)   Lee, J.; Chen, L.; West, A. H.; Richter-Addo, G. B. *Chem Rev* **2002**, *102*, 1019.

(2)   Mansuy, D.; Beaune, P.; Chottard, J. C.; Bartoli, J. F.; Gans, P. *Biochem Pharmacol* **1976**, *25*, 609.

(3)   Mansuy, D.; Rouer, E.; Bacot, C.; Gans, P.; Chottard, J. C.; Leroux, J. P. *Biochem Pharmacol* **1978**, *27*, 1129.

(4)   Mahy, J. P.; Mansuy, D. *Biochemistry* **1991**, *30*, 4165.

(5)   Harrison, J. H., Jr.; Jollow, D. J. *Mol Pharmacol* **1987**, *32*, 423.

(6)   Khan, M. F.; Wu, X.; Kaphalia, B. S.; Boor, P. J.; Ansari, G. A. *Toxicol Lett* **1997**, *92*, 31.

(7)   Bensoussan, C.; Delaforge, M.; Mansuy, D. *Biochem Pharmacol* **1995**, *49*, 591.

(8)   Yi, J.; Ye, G.; Thomas, L. M.; Richter-Addo, G. B. *Chem Commun (Camb)* **2013**, *49*, 11179.

(9)   Chakrapani, H.; Bartberger, M. D.; Toone, E. J. *J Org Chem* **2009**, *74*, 1450.

(10)   Percy, M. J.; McFerran, N. V.; Lappin, T. R. J. *Blood Rev* **2005**, *19*, 61.

(11)   Sohl, C. D.; Lee, J. Y.; Alguindigue, S. S.; Khan, M. A.; Richter-Addo, G. B. *J Inorg Biochem* **2004**, *98*, 1238.

(12)   Lee, J.; Twamley, B.; Richter-Addo, G. B. *Dalton Trans* **2004**, 189.

(13)   Schultze, S. J.; Chen, L.; Khan, M. A.; Richter-Addo, G. B. *Inorg Chem* **1997**, *36*, 6465.

(14)   Godbout, N.; Sanders, L. K.; Salzmann, R.; Havlin, R. H.; Wojdelski, M.; Oldfield, E. *J Am Chem Soc* **1999**, *121*, 3829.

(15)   Chen, L.; Khan, M. A.; Richter-Addo, G. B.; Young, V. G.; Powell, D. R. *Inorg Chem* **1998**, *37*, 4689.

(16)   Sulzer, D.; Sonders, M. S.; Poulsen, N. W.; Galli, A. *Prog Neurobiol* **2005**, *75*, 406.

(17)   Spencer, T.; Biederman, J.; Wilens, T.; Faraone, S.; Prince, J.; Gerard, K.;
         Doyle, R.; Parekh, A.; Kagan, J.; Bearman, S. K. *Arch Gen Psychiatry* **2001**, *58*,
         775.

(18)   Shelton, J.; Nishino, S.; Vaught, J.; Dement, W. C.; Mignot, E. *Sleep* **1995**, *18*,
         817.

(19)   Parli, C. J.; McMahon, R. E. *Drug Metab Dispos* **1973**, *1*, 337.

(20)   Parli, C. J.; Wang, N.; McMahon, R. E. *Biochem Biophys Res Commun* **1971**,
         43, 1204.

(21)   Wright, J.; Cho, A. K.; Gal, J. *Xenobiotica* **1977**, *7*, 257.

(22)   Cashman, J. R.; Xiong, Y. N.; Xu, L.; Janowsky, A. *J Pharmacol Exp Ther*
         1999, *288*, 1251.

(23)   Levi, M. S.; Patton, R. E.; Hanig, J. P.; Tranter, K. M.; George, N. I.; James, L.
         P.; Davis, K. J.; Bowyer, J. F. *Neurotoxicology* **2013**, *37*, 40.

(24)   Bruker-AXS *Data Collection*: SMART Software Reference Manual **1998**.

(25)   Bruker-AXS *Data Reduction*: SMART Software Reference Manual **1998**.

(26)   Frisch, M. J.; Trucks, G. W.; Schlegel, H. B.; Scuseria, G. E.; Robb, M. A.;
         Cheeseman, J. R.; Scalmani, G.; Barone, V.; Mennucci, B.; Petersson, G. A.;
         Nakatsuji, H.; Caricato, M.; Li, X.; Hratchian, H. P.; Izmaylov, A. F.; Bloino, J.;
         Zheng, G.; Sonnenberg, J. L.; Hada, M.; Ehara, M.; Toyota, K.; Fukuda, R.;
         Hasegawa, J.; Ishida, M.; Nakajima, T.; Honda, Y.; Kitao, O.; Nakai, H.;
         Vreven, T.; Montgomery Jr., J. A.; Peralta, J. E.; Ogliaro, F.; Bearpark, M. J.;
         Heyd, J.; Brothers, E. N.; Kudin, K. N.; Staroverov, V. N.; Kobayashi, R.;
         Normand, J.; Raghavachari, K.; Rendell, A. P.; Burant, J. C.; Iyengar, S. S.;
         Tomasi, J.; Cossi, M.; Rega, N.; Millam, N. J.; Klene, M.; Knox, J. E.; Cross, J.
         B.; Bakken, V.; Adamo, C.; Jaramillo, J.; Gomperts, R.; Stratmann, R. E.;
         Yazyev, O.; Austin, A. J.; Cammi, R.; Pomelli, C.; Ochterski, J. W.; Martin, R.
         L.; Morokuma, K.; Zakrzewski, V. G.; Voth, G. A.; Salvador, P.; Dannenberg, J.
         J.; Dapprich, S.; Daniels, A. D.; Farkas, Ö.; Foresman, J. B.; Ortiz, J. V.;
         Cioslowski, J.; Fox, D. J.; Gaussian, Inc.: Wallingford, CT, USA, 2009.

(27)   Datta-Gupta, N. a. B., T. J. *J Pharm Sci* **1968**, *57*, 300.

(28)   Mourad, M. S.; Varma, R. S.; Kabalka, G. W. *Synthesis-Stuttgart* **1985**, 654.

(29)   Hass, H. B.; Susie, A. G.; Heider, R. L. *J Org Chem* **1950**, *15*, 8.

(30)   Calheiros, R.; Milhazes, N.; Borges, F.; Marques, M. P. M. *J Mol Struct* **2004**, *692*, 91.

(31)   Randall, E. W.; Mitsopoulou, C. A. NMR of Compounds Containing -NH_2, -NO_2 and -NO Groups. In *Patai's Chemistry of Functional Groups;* S. Patai; Chichester, UK: John Wiley & Sons, Ltd. 1996

(32)   Li, J.; Noll, B. C.; Oliver, A. G.; Ferraudi, G.; Lappin, A. G.; Scheidt, W. R. *Inorg Chem* **2010**, *49*, 2398.

(33)   Choi, I. K.; Liu, Y. M.; Wei, Z. C.; Ryan, M. D. *Inorg Chem* **1997**, *36*, 3113.

(34)   Scheidt, W. R. Systematics of the Stereochemistry of Porphyrins and Metalloporphyrins. In *The Porphyrin Handbook;* Kadish, K.M., Smith, K.M., Guilard, R., Eds.; Academic Press: New York, 2000; Vol. 3 (Inorganic, Organometallic, and Coordination Chemistry), pp. 49-112.

(35)   Guan, Y.; Powell, D. R.; Richter-Addo, G. B. *Acta Cryst E* **2015**, *71*, m57.

(36)   Li, J.; Nair, S. M.; Noll, B. C.; Schulz, C. E.; Scheidt, W. R. *Inorg Chem* **2008**, *47*, 3841.

(37)   Hu, C.; Noll, B. C.; Schulz, C. E.; Scheidt, W. R. *Inorg Chem* **2005**, *44*, 4346.

Chapter 3. Spectroscopic studies and structural characterizations of RNO adducts of human hemoglobins and the NOAmph adducts of sw Mb H64A complex

3.1 Introduction

Organic *C*-nitroso compounds (RN=O; R = alkyl, aryl) form from the metabolic activation of their corresponding amine or nitro precursor drugs. For example, nitrosomethane (MeN=O) is generated from the metabolic activation of aziridine-based antitumor drugs.[1] *N*-hydroxyamphetamine (AmphNHOH) is generated from the *N*-oxidization of amphetamine (Amph),[2,3] and further reacts with cytochrome P450[4-6] and prostaglandin H synthase (PGHS)[7] to form nitrosoamphetamine (NOAmph). It is also known that the metabolic activation of aniline (PhNH$_2$) in rats results in the production of PhNO/PhNHOH.[8] These *C*-nitroso metabolites are toxic to cells. They inhibit the function of the important cytochrome P450 enzymes[9-11] and mitochondrial respiration in living cells, and covalently modify the βcys93 residue of human Hb.[12] In addition, it is now known that the PhNO metabolite generated from the initial interaction of aniline with red blood cells results in increased Fe deposition in the spleen, and induces methemoglobinemia and hemolytic anemia in the animal.[13] Importantly, the molecular mechanisms for the degradation and denaturing of Hb by RNO compounds remain unknown. There is also an increased interest in the design of RNO compounds as NO donors for biological studies,[14] making it even more important to study the underlying mechanisms of their toxicity towards heme proteins and red blood cells.[15]

Despite numerous spectroscopic studies on the interactions of *C*-nitroso compounds with heme proteins, very little structural information is known regarding the resulting heme-RNO products. Prior to my work in this area, there were only two heme-

RNO structures published in the literature, namely those of horse heart Mb(EtNO)[16] and the monomeric legHb(PhNO) from *Lupinus luteus*.[17]

Our work in the first half of this chapter provides insight into the molecular pathway responsible for Hb degradation by *C*-nitroso compounds. In the second half of this chapter, we extend our work to a more physiologically important drug, amphetamine (Figure 3.1, *left*).

Amphetamine   *N*-hydroxyamphetamine   Nitrosomphetamine
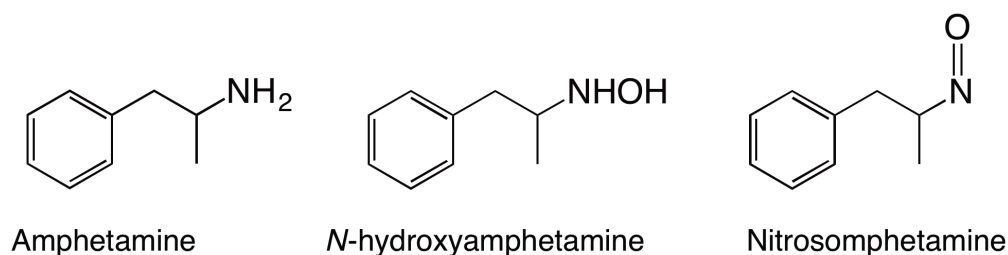
Figure 3.1. The structures of amphetamine, *N*-hydroxyamphetamine and nitrosoamphetamine.

The function and metabolism of amphetamine was introduced briefly in Chapter 2. We were interested in the AmphNHOH/NOAmph derivatives generated from the metabolism of amphetamine in vitro. The NOAmph compound (Figure.3.1, *right*) containing a phenyl group attached to the β-carbon is more bulky than the simple RNO compounds. In fact, prior to our work in this chapter, it was assumed that AmphNHOH/NOAmph could only react with heme proteins with very large active sites, such as cytochrome P450 and PHGS. It was thought that heme proteins with smaller active sites (e.g. Hb and Mb) could not form stable NOAmph-Fe^{II} protein complexes with amphetamine derivatives.[7]

3.2 Experimental section

3.2.1 Materials, instrumentation and methods

Human blood was obtained from the Emergency Room at the University of Oklahoma Medical Center in Oklahoma City. The required training allowing me to handle blood was completed prior to me handling the blood. The oxyHb was separated from the blood cells, and the subsequent purification was performed using published methods with slight modification.[18,19] The purified protein was concentrated to 140mg/mL and frozen in liquid N_2 prior to storage at -80 °C. Horse heart *met*-myoglobin (hh *met*Mb) was purchased from Sigma. Ferric swMbH64A and its crystals were kindly provided by Bing Wang of our laboratory.

Monobasic sodium phosphate, dibasic sodium phosphate, sodium hydrosulfite, sodium chloride and sodium borohydride (98.5%) were purchased from Sigma. EDTA (disodium salt), nitromethane (99.5%), nitroethane (99.5%), 1-nitropropane (98%), 2-nitropropane (97%), *n*-butylamine(99%), benzaldehyde (99%), 1-propanol (99.7%) and borane-tetrahydrofuran (1M solution in THF) were purchased from Aldrich. Anhydrous ethanol (ACS grade) was purchased from Pharmco-AAPER. THF was collected from a solvent distillation system (Innovative Technology, Inc. Newburyport, MA, USA, PS-4000-5MD) under nitrogen.

1-phenyl-2-nitropropene and *N*-hydroxyamphetamine were prepared using the same procedures described in Chapter 2. 1-phenyl-2-nitropropane was prepared by literature method.[20]

UV-vis spectroscopy experiments were carried out on a Hewlett Packard 8453 spectrophotometer equipped with a diode array detector. X-ray diffraction data sets

were collected on our home source RigakuMSC RU-H3R X-ray generator operated at

50 kV/100 mA to produce Cu/Kα radiation ($\lambda = 1.5418$ Å).

3.2.2 The preparation of metHb from oxyHb

MetHb was prepared from the oxidation of oxyHb.[18] 1.2 fold of potassium

ferricyanide was slowly added into an oxyHb solution in phosphate buffer on ice over a

5~10 min period. A color change of from red to dark red was observed. The mixture

was then dialyzed in 20 mM phosphate buffer at pH 6.8 to remove the excess salt. The

mixture was then centrifuged at 12000g for 5 min to remove any degraded protein. The

formation of metHb was determined by UV-vis spectra from the Soret, α-, and β- bands.

The extinction coefficient of metHb at 500 nm was used to calculate the concentration

of protein.[18]

3.2.3 UV-vis spectral studies of the reactions of nitroalkanes with hemoglobins in the presence of a reducing agent

The reactions between nitroalkanes and hemoglobin in the presence of a

reducing agents were examined for both oxyHb and metHb. The experiments were

carried out in 3 mL quartz cuvettes and monitored by UV-vis spectroscopy. To a 2 mL

solution of protein (7.5 μM in 100 mM phosphate buffer containing 1 mM EDTA at pH

7.4) was added a ~20 fold excess of sodium dithionite (0.01 M, 30 μL), followed by the

addition of 30 - 40 μL of the nitroalkane solution (nitroalkanes were diluted 2~fold in

methanol). The nitroalkanes used for the experiments include nitromethane, nitroethane,

1-nitropropane and 2-nitropropane. The spectra were collected aerobically at room

temperature (~21°C). The sodium dithionite solution was prepared freshly before each

reaction. The stock solution of protein was kept on ice during the experiment to minimize decomposition.

In a control experiment, sodium dithionite was added to the protein solution prior to the addition of the nitroalkanes. The results did not show significant differences between these two methods in the generation of the final products.

3.2.4 Crystallization of Hb(RNO) derivatives

For the preparation of Hb(RNO) complexes, sodium dithionite (~100-150 mg) and the respective nitroalkanes RNO_2 (R = Me, Et; 50 μL) were added to a solution of purified human metHb (30-40 mg/mL; phosphate buffer, pH 6.8). The mixture was kept at 4 °C for 4-5 h, centrifuged, and the precipite was discarded.

Crystals of the Hb(RNO) derivatives were obtained using the batch method according to published procedures for Hb derivatives.[19] Several pH conditions in the 5.6–7.0 range were achieved by varying the volume ratios of sodium phosphate (monobasic; 3.2 M) to potassium phosphate (dibasic; 3.2 M). 100 μL of protein solutions (40 mg/mL) were added into various amounts (0.18–0.38 mL) of phosphate buffer as well as 1–2 drops of toluene in 3 mL-sized vacutainer tubes. The protein solutions were mixed gently by slowly inverting the stoppered vacutainer tubes. Diamond shaped crystals of the Hb(RNO) (R = Me, Et) products started forming after ~3 days. Suitably sized Hb(RNO) crystals were harvested using cryo-loops, soaked in the mother liquid containing 16% glycerol for 5 min, and then flash-frozen in liquid nitrogen prior to data collection.

3.2.5 X-ray diffraction data collection and processing (with Dr. Jun Yi)

Data collection and structure solutions were performed in collaboration with Dr. Jun Yi.

X-ray data were collected at 100 K on the homesource RigakuMSC RU-H3R X-ray generator operated at 50 kV/100 mA to produce Cu/Kα radiation ($\lambda = 1.5418$ Å). For the Hb(MeNO) structure, 0.5° oscillation images were collected over a range of 100° with an exposure time of 5 min/image and a crystal-to-detector distance of 160 mm. For the Hb(EtNO) structure, 0.5° oscillation images were collected over a range of 145° with an exposure time of 5 min/image and a crystal-to-detector distance of 160 mm. Diffraction data were indexed and processed with the d*TREK program (Macintosh v.99D).[21]

In general, the phase information was obtained using the molecular replacement method as implemented in *PHASER* (v1.3.3).[22] The search model was the 1.8 Å resolution structure of human Hb nitrite (PDB access code 3D7O)[23] with all solvent molecules and nitrite ligands removed. For the R_{free} calculation, 5% of randomly selected reflections were flagged and carried throughout the complete refinement procedure. The *CCP4* program *REFMAC*[24] and the *PHENIX*[25] refinement program were utilized for structure refinement. Bulk-solvent modeling and isotropic scaling of the observed and calculated structural amplitudes were used during the restrained refinements. *COOT*[26] was used for visualization and model building/corrections between refinement cycles. Water molecules were added to the structures using the "*Update Waters*" command in *PHENIX* at the later steps of refinements.

Hb(MeNO): The initial electron density map after molecular replacement revealed the presence of V-shaped Fe-bound ligands in the sixth positions for both alpha and beta subunits. The MeNO ligands were modeled into these V-shaped electron densities with the central N atom bound to Fe in both heme active sites. The nitrosomethane ligand file was imported from the monomer library implemented in the CCP4 suite with a molecular code of NSM. The Fe–N(nitrosomethane) bond distance and angle parameters were unrestrained throughout refinements; however, internal restraints of 1.22(2) Å (for d(N–O)), 1.45(2) Å (for d(C–N)) and 120(3)° (for $\angle$CNO) were applied to the nitrosomethane group. In addition to the axial ligands, three glycerol molecules were modeled into the crystal lattice based on the electron density map. The C-terminus residue of Arg141 in the alpha subunit was omitted from the structural model due to the poor electron density. The final crystallographic R and R_{free} of the human Hb(MeNO) structure are 0.22 and 0.28, respectively, in the 21.43–2.05 Å range.

Hb(EtNO): The initial electron density map revealed an axial ligand bound to heme Fe in the alpha distal pocket. The nitrosoethane ligand was modeled into this electron density map via the N atom bound to heme Fe. The crystallographic information file of nitrosoethane ligand was imported from the monomer library implemented in the CCP4 suite with a molecular code of NOE. The Fe–N(nitrosoethane) bond distance and angle parameters were unrestrained throughout refinements; however, internal restraints of 1.22(2) Å (for d(N–O)), 1.45(2) Å (for d(C2–N)) and 120(3)° (for $\angle$C2NO) were applied to the nitrosoethane group. One

glycerol molecule was modeled in the crystal lattice located at the interface of two subunits.

The electron density map of the beta heme moiety was not as clear as that in the alpha subunit. In addition to the expected heme position, there was new electron density beneath the distal His63 sidechain that showed a weak interaction with the Nε atom of this residue. To evaluate the likelihood that the extra density was due to a subpopulation of heme Fe, the *SFTool* and *FFT* programs in *CCP4* were used to calculate the Fe anomalous signals for this structure. In the anomalous map, there were two positive electron densities with an intensity ratio of 1:1, thus confirming that these signals were both from Fe in two positions [Fe_1 for the "original" heme site, and Fe_2 for the shifted heme that was shifted ~5.0 Å from its original position]. The original heme was removed from the structural model to recalculate an unbiased difference electron density map for the beta heme site. Two heme molecules were modeled into the difference density map with 50% occupancy per molecule guided by the iron anomalous map as well. There was no defined electron density showing axial ligand binding due to EtNO in the beta subunit.

The C-terminus residue Arg141 in the alpha subunit was omitted from the structural model due to the lack of electron density. The final crystallographic R and R_{free} (for the final model) of the human Hb(EtNO) structure were 0.23 and 0.27, respectively, in the 21.4–2.0 Å range.

The $2F_o$–F_c electron density maps and the F_o–F_c electron density maps were generated using *FFT* as implemented in *CCP4*. The figures of electron density maps

and the final model of the heme site of the human Hb(RNO) structures were drawn

using PyMOL.

Table 3.1. X-ray data collection and refinement statistics[a]

	Hb(MeNO)	Hb(EtNO)
Data Collection		
PDB accession code	4M4A	4M4B
Space group	$P4_12_12$	$P4_12_12$
Unit cell dimensions (Å)	53.57, 53.57, 191.87	53.44, 53.44, 193.58
Resolution range (Å)	21.43-2.05	21.4-2.0
Number of observations	110487	203574
Unique reflections	18023	19790
Average multiplicity	6.13(6.44)	10.29(7.05)
Completeness (%)	97.7(92.9)	99.4(93.5)
$<I/\sigma(I)>$	9.2(4.8)	22.1(5.8)
R_{merge}[b]	0.087(0.23)	0.044(0.274)
Refinement		
Number of protein atoms	2266	2180
Number of heteroatoms	168	218
R-factor[c]	0.224	0.229
R_{free}[d]	0.28	0.270
Average B-factor (Å^2)[e]	33.68	53.86
rms deviations[f]		
bond lengths (Å)	0.01	0.01
bond angles (°)	1.1	1.23
Ramachandran plot (%)[g]		
favored	97.9	97.52
outliers	0	0
rotamer outliers	0	0.87

[a] The data in brackets refer to the highest resolution shell.
[b] $R_{merge} = \Sigma_{\eta kl}\Sigma_i |I_i(hkl) - <I(hkl)>|/\Sigma_{\eta kl}\Sigma_i I_i(hkl)$, where $I_i(hkl)$ is the ith used observation for unique hkl, and $<I(hkl)>$ is the mean intensity for unique hkl.
[c] $R = \Sigma_{hkl}||F_{obs}| - |F_{calc}||/\Sigma_{hkl}|F_{obs}|$, where F_{obs} and F_{calc} are the observed and calculated structure factors, respectively.
[d] R_{free} was calculated using 5% of the randomly selected diffraction data which were excluded from the refinement.
[e] The average for the polypeptide atoms.
[f] deviations from ideal values.[27]
[g] calculated using *MolProbity* [28] as implemented in *PHENIX.*

3.2.6 The UV-vis spectral studies of reactions between Mb and its mutant with amphetamine derivatives

Both hh Mb and sw MbH64A were used for these experiments. Protein concentrations were calculated using the extinction coefficient of metMb of 9.47 mM^{-1}cm^{-1} at 505 nm.[18] Both 1-phenyl-2-nitropropane and *N*-hydroxyamphetamine were used in these reactions. The experiments were carried out in a 3 mL quartz cuvette and monitored by the UV-vis spectroscopy.

Reaction with 1-phenyl-2-nitropropane: 8 µL of 1-phenyl-2-nitropropane (half diluted in methanol) was added to a 2 mL of 7 µM hh Mb solution (100 mM phosphate buffer at pH 7.4), followed by an addition of freshly prepared sodium dithionite (0.02 M, 20 µL) solution.

Reaction with N-hydroxyamphetamine: *N*-hydroxyamphetamine (5 µL) was added to a 2 mL of 2.2 µM sw MbH64A solution (100 mM phosphate buffer at pH 7.4). The *N*-hydroxyamphetamine solution was prepared by dissolving 6 mg *N*-hydroxyamphetamine into 1 mL phosphate buffer (100 mM, pH = 7.4). The ligand had poor solubility in water, thus the mixture of ligand/water was vortexed three times for 1 min each to help the ligand dissolve. However, there were still white precipitates on the bottom of solution after vortexing. The clear supernatant on top was added into the protein solution and the spectra were recorded.

For the examinations of the stability of the tentative nitrosoamphetamine-sw MbH64A complex, potassium ferricyanide (5 µL, 0.05 M) or sodium dithionite (30 µL, 0.02 M) were added into the protein solution. The changes were monitored by UV spectroscopy.

3.2.7 Soaking of crystals of sw MbH64A with *N*-hydroxyamphetamine

Crystals of met sw MbH64A in a hanging drop plate (2.4 M AmSO$_4$, 1 mM EDTA, 100 mM Tris-HCl buffer, pH 9.0) were kindly provided by Bing Wang. The solution with crystals was pipeted into a 10 μL droplet of cryo solution (3.1 M AmSO$_4$, 1 mM EDTA, 10 % glycerin, 100 mM Tris-HCl buffer) on a glass slide. The droplet was washed with the same buffer with 10% glycerol several times and covered with mineral oil. Two methods were used for the addition of ligands. One was the addition of *N*-hydroxyamphetamine in powder form via a needle. The white powder floated on the surface of the droplet at the beginning and slowly dissolved after several hours. Another method was the addition of *N*-hydroxyamphetamine in methanol. The ligand solution was pipeted into the droplet. The dark red crystals gradually turned to pink during soaking. Suitably sized crystals with differing soaking times (4 hours to 2 days) were harvested with cryoloops and flash frozen in liquid nitrogen.

3.2.8 X-ray data collection and processing (with Bing Wang)

Data collection and structure solutions were performed in collaboration with Bing Wang.

The diffraction data was collected at 100 K at home source using a Rigaku RU-H3R X-ray generator coupled to a R-axis 4++ image plate detector. The data was collected at 1° oscillation angles over a 100° range with a crystal-to-detector distance of 110 mm, and an exposure time of 5 min. The data was processed using iMosflm and SCALA as implemented in the CCP4 program suite.

The phase problem was solved by the molecular replacement method with PHASER (CCP4). The starting model used was wild type met swMb(H$_2$O) at 1.5 Å

resolution (PDB code 2mbw). All water molecules and ligands were removed from the starting model.

Refinement was performed with Refmac5 (CCP4 suite) and COOT. The initial 10 cycles of restrained refinement were run with Refmac, and the R factor decreased from 0.355 to 0.275. The ligand (N-hydroxyamphetamine), sulfate ions, glycerol and water were added to the model based on the F_o-F_c electron density maps in the following refinement cycles. One N-hydroxyamphetamine ligand, four sulfate anions and five glycerol molecules were eventually added into the model. Two conformations of Lys87, Lys133, Lys145 and Gly153 were modeled with 50% occupancy for each conformation. The N-terminal residue methionine was omitted because of the lack of electron density. The final R factor and R_{free} were 0.149 and 0.177, respectively.

The model of N-hydroxyamphetamine was taken from our unpublished X-ray structure of (OEP)Fe(NOAmph)(1-MeIm) in Chapter 2. To perform restrained refinement in Refmac5, the atoms of N-hydroxyamphetamine were selected from the Pymol file and saved as another pdb file which was run in Prodrg (CCP4 suite) to generate the coordinates in a new pdb file and the topologies in a monomer library cif file.

3.3 Results and discussion

The objective of this work was to study the reactions between Hb and a series of simple nitrosoalkanes (RNO; R = Me, Et, Pr, ^{i}Pr) by UV-vis spectroscopy and X-ray crystallography to obtain insight into how the different R groups in these nitrosoalkanes affect the properties and reactivities of their Hb(RNO) adducts. Mansuy and coworkers have reported the UV-vis spectral studies of these compounds previously.[29] However,

no structural studies on these compounds had been reported prior to our work in this area.

3.3.1 Spectroscopic studies of the formation of Hb(RNO) complexes

Primary (1°) and secondary (2°) nitrosoalkanes are not stable as monomers,[30] as they isomerize to their more stable oxime derivatives (middle of Scheme 3.1; with a generic 2° R'C(Me)HNO nitroso compound). Thus, the nitrosoalkanes used in my work could not be reacted directly with the Hb protein. In general, there are two synthetic routes used for the preparation of hemeprotein-RNO complexes. One of these methods utilizes the reactions between *nitro*alkanes (RNO$_2$) and heme proteins in the presence of a reducing agent (left of Scheme 3.1).[29]
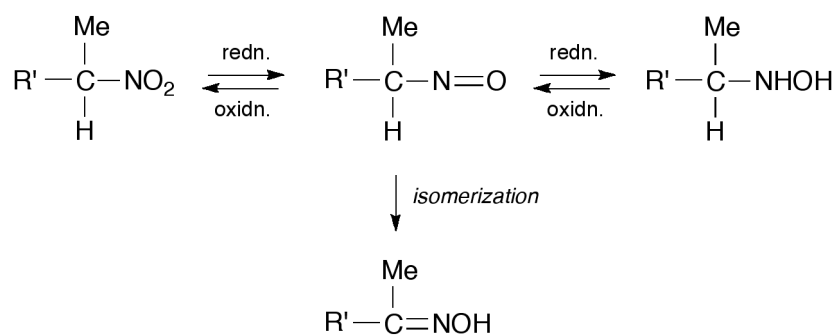
Scheme 3.1. Synthetic routes for the preparation of hemeprotein-RNO complexes.

The addition of excess sodium dithionite (as the reducing agent) into a mixture of ferric metHb and the RNO$_2$ reagents generated the ferrous Hb and the nitrosoalkanes simultaneously, to result in the formation of the Hb(RNO) products. Another method reported in the literature (and utilized in Chapter 2 of this thesis) is the direct interaction of a hemeprotein with the corresponding alkylhydroxyamine RNHOH (right of Scheme

3.1).[9] Since these *N*-alkylhydroxylamines are less stable in air than the corresponding

nitroalkanes, first method was utilized to prepare the Hb(RNO) derivatives.

In general, a ~20 fold excess of sodium dithionite was added into an aerobic

solution of oxyHb solution followed by an addition of the nitroalkane that was half-

diluted in methanol (to increase its solubility). The same procedure was used when

metHb was employed. The order of addition of the reagents was altered in some of the

experiments for the purpose of comparison. Although dithionite is known to cause Hb

degradation over long exposure periods, no formation of precipitates was observed

during the time course of the experiments below. Dithionite is frequently employed to

scavenge trace oxygen from solutions,[18] and this feature of dithionite most likely

explains why either oxyHb or metHb yield the same final Hb(RNO) products.

Addition of nitromethane ($MeNO_2$) to dithionite-reduced ferrous Hb (λ_{max} 430

nm) generated a species with λ_{max} at 420 nm as shown in the UV-vis spectra in Figure

3.2. We also observed the shifts of Q bands from 555 nm (due to ferrous Hb) to 545/560

nm due to the product. Importantly, the 420 nm species did not form when $MeNO_2$ was

added directly to metHb (λ_{max} 406 nm) or when sodium dithionite was not used in

excess.
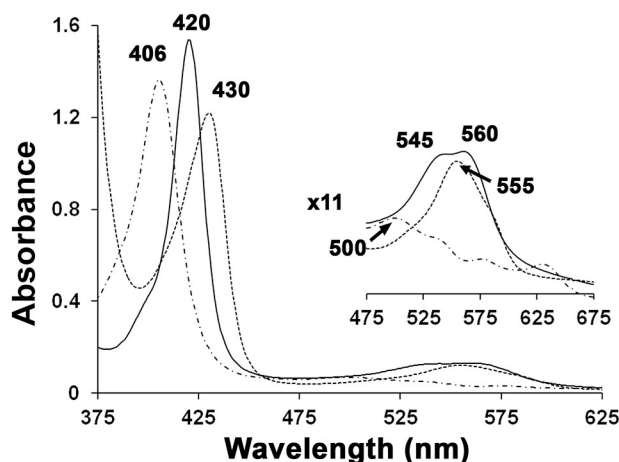
Figure 3.2. UV-vis spectra showing the conversion of ferric aquometHb (dashed line; λ_{max} 406 nm) to ferrous Hb (dotted line; λ_{max} 430 nm) and then to ferrous Hb(MeNO) (solid line; λ_{max} 420 nm). [Hb] = 7.5 μM; 100 mM phosphate buffer, 1 mM EDTA, pH 7.4.

A time-course experiment was performed for this reaction (Figure 3.3). For this experiment, the reaction was set to $t = 0$ at the time that nitromethane was added to the dithionite-reduced Hb (λ_{max} 430 nm). As shown in Figure 3.3, the Soret peak of deoxyHb at 430 nm completely shifted to 420 nm within 90 sec, after which time the intensity of the peak at 420 nm no longer increased. This indicated that the reaction was complete, but the reaction mixture was left to stand for a period of one hour to monitor any subsequent changes. There were three isosbestic points in the spectra obtained for this reaction, which are labeled with arrows in Figure 3.3 at 407, 426 and 456 nm. The presence of these isobestic points indicated that the reaction involved only two Hb species, the ferrous Hb and Hb(MeNO), without the involvement of any Hb intermediates.
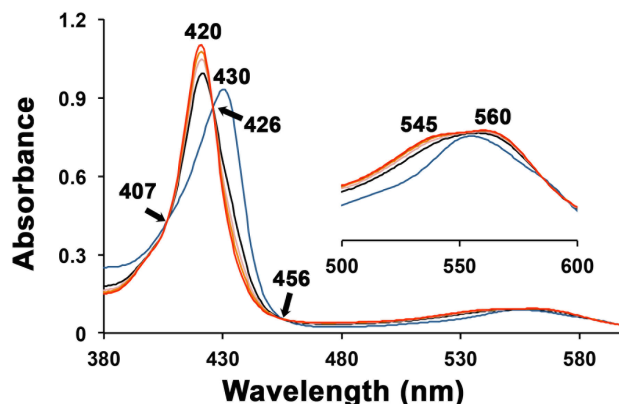
Figure 3.3. The time-course monitoring of the conversion of ferrous Hb (blue line; λ_{max} 430 nm) to ferrous Hb(MeNO) (orange line; λ_{max} 420 nm) by UV-vis spectroscopy. The first spectrum was taken at $t = 0$ s (when nitromethane was added), followed by spectral collection at 10 s, 20 s, 30 s and 90 s. Isosbestic points are at 407, 426 and 456 nm.

This 420 nm complex was stable for at least 4 days at 4 °C in air, showing no signs of significant decomposition to the ferric (λ_{max} 406 nm) or the oxy-Hb (λ_{max} 415 nm) forms (Figure 3.4). Due to the stability of this 420 nm complex, we determined that it should be feasible to crystallize pre-formed Hb(MeNO) from solution.
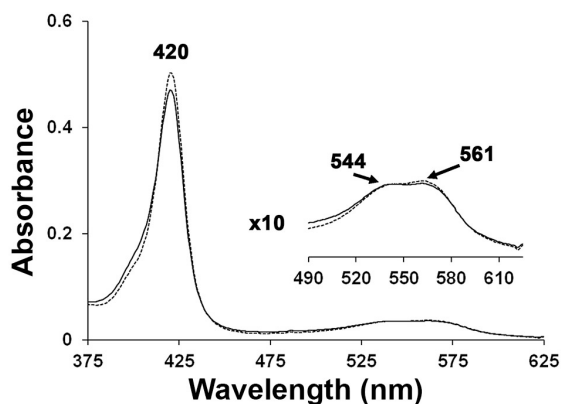
Figure 3.4. The UV-vis spectra of Hb(MeNO) in solution showing no signs of significant decomposition after the solution was left in air for 4 days at 4 °C (100 mM phosphate buffer, 1 mM EDTA, pH 7.4). The solid line is the initial spectrum. The dotted line is the spectrum of the complex after the 4 day period.

The analogous reaction using nitroethane (EtNO$_2$) resulted in the formation of a spectrum (Figure 3.5) similar to that of the product in Figure 3.2. The reaction generated a product with λ_{max} at 421 nm and additional Q bands at 544 and 561nm.
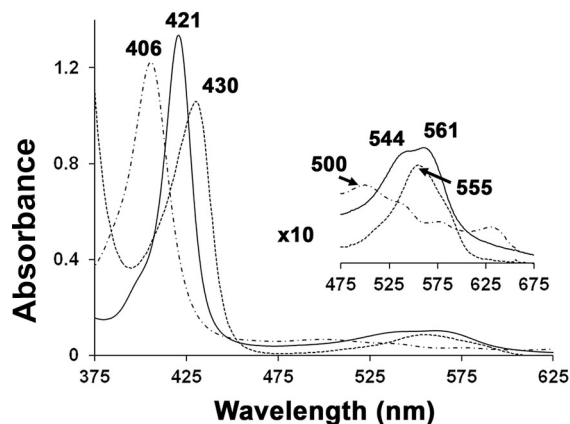
Figure 3.5. UV-vis spectra showing the conversion of ferric aquometHb (dashed line; λ_{max} 406 nm) to ferrous Hb (dotted line; λ_{max} 430 nm) and then to ferrous Hb(EtNO) (solid line; λ_{max} 420 nm). [Hb] = 6.6 μM; 100 mM phosphate buffer, 1 mM EDTA, pH 7.4.

The reaction was complete in ~3 min, as determined by a lack of further change of the 421 nm peak intensity. This is a relatively slow reaction compared to the previously described reaction with nitromethane (see above). Furthermore, the Hb(EtNO) product complex was less stable than its MeNO analogue, showing signs of decomposition after the solution was left in air for 2 days at 4°C (Figure 3.6).
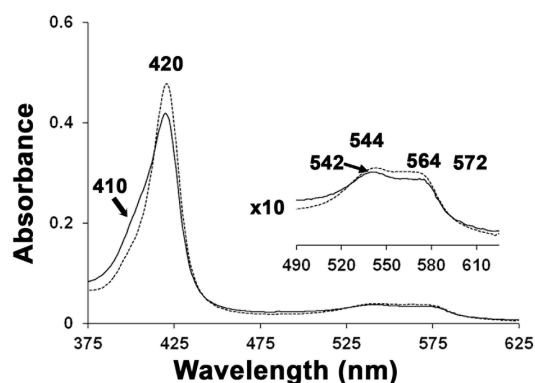
Figure 3.6. UV-vis spectra showing the decomposition of the product complex Hb(EtNO) at 420 nm. The dash line is the initial spectrum, and the solid line is the spectrum after 39 hours (100 mM phosphate buffer, 1 mM EDTA, pH 7.4).

After two days of exposure of Hb(EtNO) to air, the appearance of a shoulder peak at ~410 nm as well as the shifts of the peaks in the visible region to 542 and 572 nm were observed (Figure 3.6). The positions of the new peaks in the visible region are the same as the Q bands of oxyHb (542, 577 nm), which indicate the possible formation of oxyHb in solution. The instability of Hb(EtNO) was further demonstrated by X-ray crystallography, which will be discussed later in this chapter.

We extended our work to other nitroalkanes with larger alkyl groups, including 1-nitropropane and its isomer 2-nitropropane. Not surprisingly, those two compounds showed even slower reactions with metHb. The reaction involving 1-nitropropane was complete after only ~40 mins as determined by the lack of further change in the 419 nm peak intensity. Similar to the Hb(EtNO) complex, this 419 nm product complex is not very stable, decomposing slowly over a ~12 hr period in air.

When the more sterically hindered 2-nitropropane was used in the same reaction, the formation of an analogous 420/419 nm complex was not observed (Figure 3.7).

Rather, the spectra showed a slow aerobic conversion of deoxyHb (λ_{max} 430 nm; prepared from metHb at 406 nm) to oxyHb with the formation of new peaks at 415, 542 and 576 nm over a 1 hr period. I thus speculate that after the addition of 2-nitropropane to the protein solution followed by its reduction to the secondary 2-nitrosopropane by dithionite, that the 2-nitrosopropane ligand competes with oxygen to bind the heme site, and that sterics favor O_2 binding rather than the bulky 2-nitrosopropane ligand.
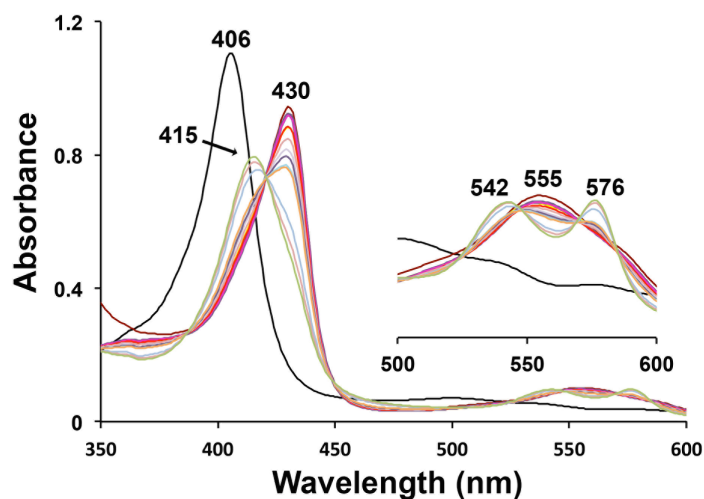
Figure 3.7. UV-vis spectral monitoring of the reaction between ferric aquometHb (black line; λ_{max} 406 nm) and dithionite to generate ferrous Hb (dotted line; λ_{max} 430 nm), and its subsequent conversion to oxyHb (light green line; λ_{max} 415 nm) after the addition of 2- nitropropane. [Hb] = 6.0 µM; 100 mM phosphate buffer, 1 mM EDTA, pH 7.4.

Overall, both the rates and extent of formation of the Hb(RNO) derivatives from metHb followed the order $MeNO_2 > EtNO_2 > PrNO_2 > {}^iPrNO_2$. This is seen in the initial slopes of the product spectra in Figure 3.8.
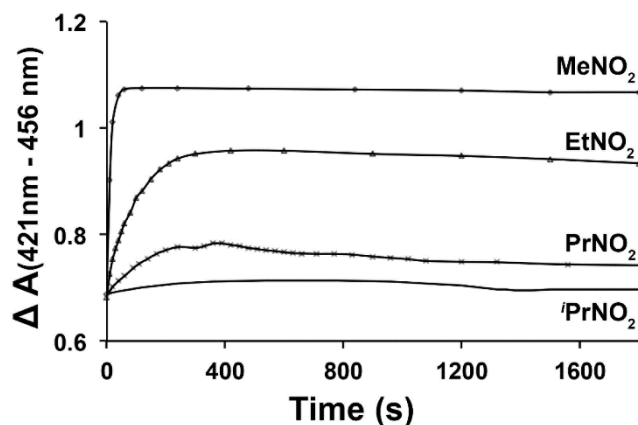
Figure 3.8. UV-vis spectral monitoring of the reactions between metHb and the various nitroalkanes in the presence of excess sodium dithionite.

This result is consistent with that previously reported by Mansuy.[29] In Chapter 2, we discussed nitrosoalkanes (RN=O) serving as π acids when they bind to the iron centers via their N-atoms. It is thus not surprising that MeNO shows the highest affinity to the Fe center, since it has more π acid properties compared to its analogues (i.e., Me is the least electron-donating of all the alkyl groups used). Also, since the reaction involves the movement of an external ligand into the heme active site, the nitrosoalkanes with shorter chains and more simple structures are likely better suited for efficient entry into the heme pocket.

Since all these reactions involve an "A + B + C" pattern (A = Hb, B = dithionite, C = nitroalkane), we further studied these reactions by changing the order of addition of the three reagents. We observed that the alternate addition of nitromethane to metHb followed by sodium dithionite resulted in the shifts of peaks to the Hb(RNO) product peaks at ~ 420, 543 and 572 nm. Although the Soret band at ~420 nm, as previously stated, indicates the formation of the Hb(RNO) derivatives, the peak profiles in the

visible region indicate that some other Hb complexes such as oxyHb may also be present in the products. Consequently, the addition of a reducing agent *before* addition of nitroalkanes were the preferred method to obtain the Hb(RNO) complexes in this work.

The differences between oxyHb and metHb (as the source of Hb) in these reactions were also examined. No difference in regards to the rates and extents of formation of the Hb(RNO) products was observed.

3.3.2 Spectroscopic studies of the formation of the Mb-nitrosoamphetamine complexes

As noted in the Introduction, nitrosoamphetamine (NOAmph) is an oxidative metabolite formed from amphetamine binds to the Fe center in various heme proteins. In Chapter 2, we reported the successful generation and crystallographic characterization of several heme model Fe-nitrosoamphetamine (Fe-NOAmph) complexes. Our three-dimensional structural results from Chapter 2 show that the NOAmph ligand binds to the Fe centers via the N-atoms. I was thus curious whether this relatively bulky NOAmph ligand would be able to enter and bind to the Fe center in a heme protein such as Mb, especially since the 2° nitrosopropane ligand did not show observable binding to the heme site in Hb (see above section). In fact, Mansuy and co-workers studied the abilities of different heme proteins to bind with various bulky and hydrophobic nitrosoalkane ligands,[7] and proposed that due to the relatively small active sites of Hb and Mb, that large/bulky and hydrophobic ligands (such as NOAmph) are far less likely to form Fe^{II}-RNO derivatives. I thus extended our RNO binding studies to the NOAmph ligand.

For NOAmph reactions, I tried both synthetic routes shown in Scheme 3.1, using both 1-phenyl-2-nitropropane and *N*-hydroxyamphetamine as the NOAmph precursors. Although AmphNHOH is less stable than 1-phenyl-2-nitropropane in solution, it is more hydrophilic than its nitroalkane derivative. To further assist with the binding of this ligand to the Mb heme site, I not only used wt Mb for our reactions, but also a distal pocket mutant, swMbH64A. In Chapter 2, the reactions between AmphNHOH and the ferric porphyrins were carried out in an anaerobic environment. However, I found that the reactions between AmphNHOH and Mb could occur aerobically. One of the two reactions presented here involves the reaction between hh Mb with 1-phenyl-2-nitropropane (NO_2Amph) in the presence of sodium dithionite. The other reaction is the one involving reaction between sperm whale (sw) MbH64A and AmphNHOH. The UV-vis spectra of the products from both methods indicated successful formation of the hh Mb Fe^{II} –NOAmph complex in solution, although the sw MbH64A-NOAmph complex appeared to be more stable than the wild type hh Mb-NOAmph analogue.

As shown in Figure 3.9, the addition of excess sodium dithionite to wt hh metMb (λ_{max} 408 nm) resulted in the generation of deoxyMb (λ_{max} 435 and 555 nm).
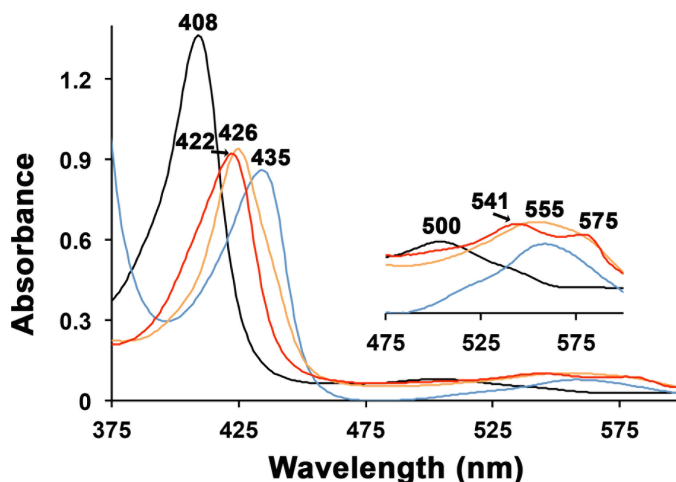
Figure 3.9. UV-vis spectra showing the conversion of ferric hhMb (black line; λ_{max} 408 nm) to ferrous hhMb (blue line; λ_{max} 435 nm) and then to a putative hh Mb(NOAmph) complex (orange line; λ_{max} 426 nm). This 426 nm product converts/decomposes to a 422 nm (red line) complex over a two-day period. [Mb] = 7.1 μM; 100 mM phosphate buffer, 1 mM EDTA, pH 7.4.

When 1-phenyl-2-nitropropane (NO₂Amph) was added into the solution

containing hh deoxyMb, the Soret peak shifted to 426 nm over a 5-hr period. This new

Soret peak is close to those of Mb/Hb(RNO) compounds (see earlier), suggesting the

formation of the wt hh Mb(NOAmph) product. However, the formation of new peaks

in the visible region was not as clearly evident. Although the peak at 555 nm (for

deoxyMb) clearly decreased over the 5-hr reaction time period, along with the

formation and slight increase of the peaks at 541 and 575 nm, a major peak in the

visible region still remained at 555 nm indicative of unreacted deoxyMb. The 541 and

575 nm peaks increase over a two-day period, with concomitant decrease in the 555 nm

peak and a broadening of the Soret band. The broadness of the Soret peak was likely

due to the re-appearance of a minor metMb peak at 408 nm (along with the appearance

of a peak at 500 nm due to metMb). I conclude that while wt hh Mb(NOAmph) forms

in solution, it is not very stable and oxidizes to the metMb precursor in air. The

instability of wt Mb(NOAmph) is not really a surprise due to the bulkiness of the

NOAmph ligand. However, I was glad to see some Mb(NOAmph) formation given the

relatively small size of the Mb active site pocket.

An objective of this project was to obtain a crystal structure of an NOAmph

ligand bound to Mb as this would provide some crucial insight into the nature of

binding of this bulky, but physiologically relevant ligand to heme centers.   Since the

crystallization of a protein complex is greatly affected by its stability in solution, it was

important to enhance the stability of such a Mb(NOAmph) product. I thus turned to the

sw MbH64A distal pocket single mutant, which has a greater ligand access to the heme

pocket. Our lab had worked with sw MbH64A previously in another project (c/o Bing

Wang). I also substituted the 1-phenyl-2-nitropropane starting reagent with N-

hydroxyamphetamine to react with sw MbH64A in the reaction.   The distal pocket

His64 residue in Mb is well known as a "gate" for ligand entry and escape.[31] The

substitution of histidine by alanine would thus likely open the gate and allow better

ligand access to the active center. Fortunately, we noted from UV-vis spectroscopic

studies, that these changes increased the reaction rate and stability of the Mb(NOAmph)

protein complex.

Figure 3.10 shows the UV-vis spectral monitoring time course of the reaction

between N-hydroxyamphetamine and sw metMbH64A (λ_{max} 406 nm).   I observed a

gradual decrease of the Soret peak of sw metMbH64A over an 80 min reaction period,

accompanied by the appearance of three new peaks at 425, 541 and 573 nm. These new

peaks are consistent with those of other Mb(RNO) proteins,[30] and are assigned to the sw

MbH64A(NOAmph) product. It is also interesting to note that a small shoulder around

402 nm started showing up during this reaction (even after ~30 mins). In fact, the
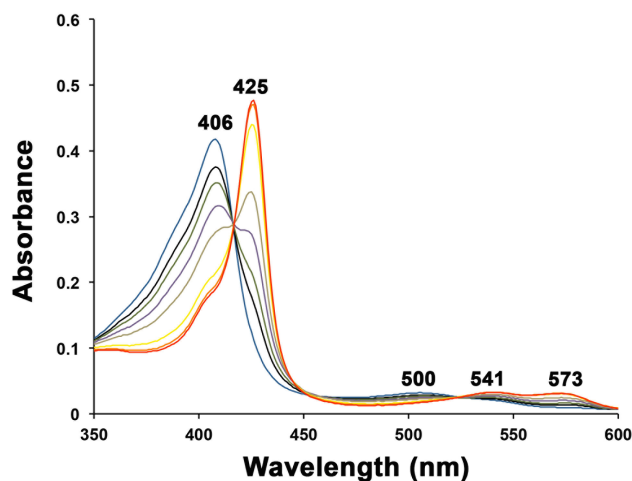
Figure 3.10. Time course of UV-vis spectra showing the conversion of ferric sw MbH64A (blue line; λ_{max} 406 nm) to sw MbH64A(NOAmph) during an 80 min reaction time period (orange line; λ_{max} 425 nm). Spectra were recorded at 0 s (blue), 1 min (dark grey), 2 min (grey), 5 min (purple), 15 min (green), 30 min (yellow), 60 min (orange), and 80 min (red). [Mb] = 2.2 µM; 100 mM phosphate buffer, 1 mM EDTA, pH 7.4.

spectra taken before the 30 min time period had good isosbestic points at 417, 502, 524

and 603 nm (not shown), which indicated a 1:1 reaction up to that point. These

isosbestic points became less clear in subsequent spectra collected after this initial 30

min time period. The formation of this unusual shoulder around 402 nm is probably the

result of some unexpected side reactions of protein.

This new complex sw MbH64A(NOAmph) showed a high stability in solution

at room temperature (Figure 3.11). The green and red lines in Figure 3.11 represent the

spectrum of the same protein solution after 1 day and 5 days of reaction time,

respectively. Although we could still observe the shoulder peak at 402 nm, there was no

sign of decomposition of the sw MbH64A(NOAmph) to the met form (λ_{max} 406 nm;

shown in black in the Figure) during this 5 day period. The stability of this new

complex allowed for its crystallization and X-ray structural characterization (see later).
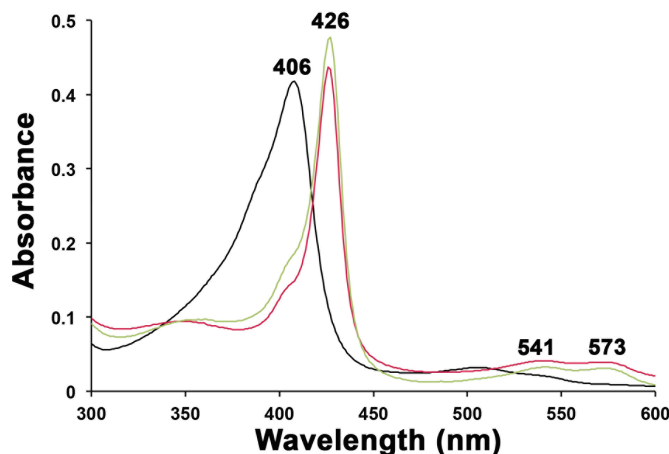
Figure 3.11. The UV-vis spectum showing no decomposition of swMbH64A-NOamph after the solution was left in air for 5 days. The black line is the spectrum of the ferric swMbH64A. The green line and red line showing the spectra of the solution after 1 day and 5 days (100 mM phosphate buffer, 1 mM EDTA, pH 7.4).

The addition of sodium dithionite to the ferrous sw MbH64A(NOAmph)

solution did not lead to any change of the spectrum. However, addition of the oxidant

potassium ferricyanide to the solution resulted in a quick spectrum change that indicated

formation of the ferric met form. As a result, the bound ligand in the heme pocket

quickly dissociated from the metal as we have shown previously in heme model

complexes (ferric porphyrins have low affinity for RNO ligands, as there is limited π

backbonding available from the d^5 ferric center to the π^* orbital of the RNO ligand).

3.3.3 Crystallographic results of the Hb(MeNO) and Hb(EtNO) products

From the UV-vis spectral studies above, only $MeNO_2$ and $EtNO_2$ reacted with

Hb in the presence of a reducing agent to form complexes that were sufficiently stable

for crystallization. Both the oxyHb and metHb precursor proteins were used in the

reactions. The metHb reaction, after appropriate workup, produced suitable crystals, whereas those obtained from the oxyHb reaction were not as suitable for X-ray diffraction studies (Figure 3.12).
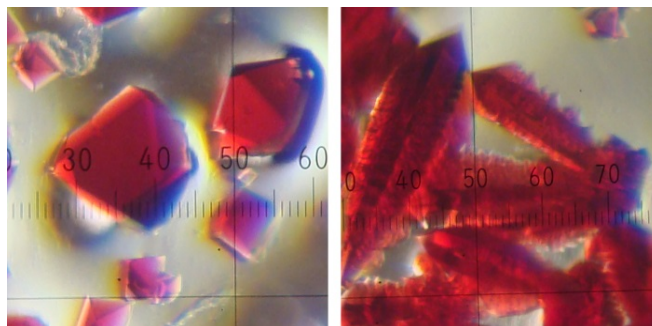
Figure 3.12. Hb(EtNO) crystals grown from (*left*) the metHb/nitroethane/dithionite reaction, and (*right*) from the oxyHb/nitroethane/dithionite reaction.

Crystals of Hb(MeNO) were generated using the batch method, and the crystal structure was solved to 2.05 Å resolution. Comparisons with known Hb crystal structures, including an analysis of the root mean square deviations between the tetramers as well as the critical contacts at the α1β2 interface, show the Hb(MeNO) crystal structure to be in the *R* state. The determination of the quaternary structures of the Hb(RNO) complexes will be discussed at the end of this section.

The electron density maps, and in particular the F_o–F_c omit electron density map of the active sites of the *α* and *β* subunits (Figure 3.13) clearly reveal the presence of V-shaped electron density in both subunits due to bound nitrosomethane (MeNO) ligands. The MeNO ligands bind Fe via their N atoms, and are further stabilized by H-bonding between the nitroso O atoms with the distal His ligands. The nitrosomethane CNO planes are generally situated between adjacent porphyrin N(pyrrole) atoms. The heme propionates of the *α* heme are pointed in different directions; one pointed in the

general direction of the distal pocket, and the other in the direction of the proximal pocket. In contrast, both heme propionates of the β heme point away from the distal His63 residue suggesting, perhaps, a higher likelihood of ligand access to/from this distal pocket. Importantly, this was the first report of a metal-MeNO crystal structure for any protein.
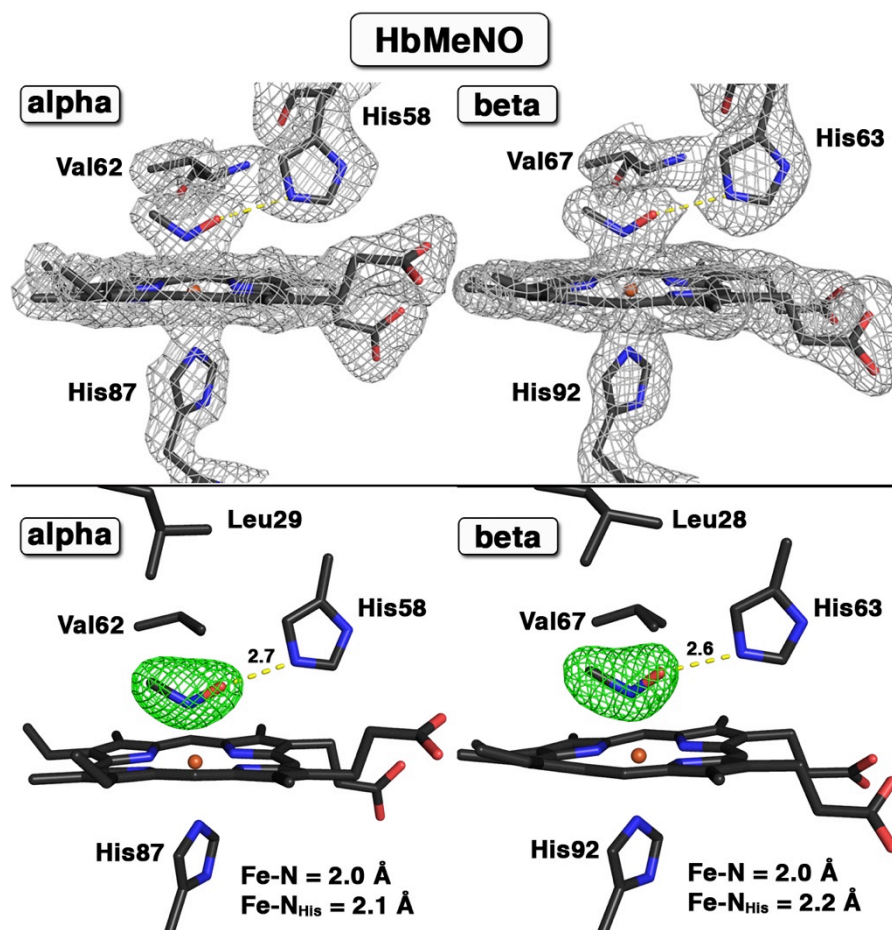
Figure 3.13. (*Top*) $2F_o$–F_c electron density maps (grey mesh, contoured at 1.0 σ), and (*Bottom*) F_o–F_c omit electron density maps (green mesh, MeNO groups, contoured at 3.0 σ) and final models of the α and β active sites of the Hb(MeNO) complex (PDB accession code 4M4A, 2.05 Å resolution).

We were also able to obtain crystals of Hb(EtNO) from the nitroethane reaction, and we solved the structure to 2.0 Å resolution. The $2F_o$–F_c electron density maps and

F_o–F_c omit electron density maps for the product derived from the dithionite-reduced

Hb/EtNO$_2$ reaction are shown in Figure 3.14.
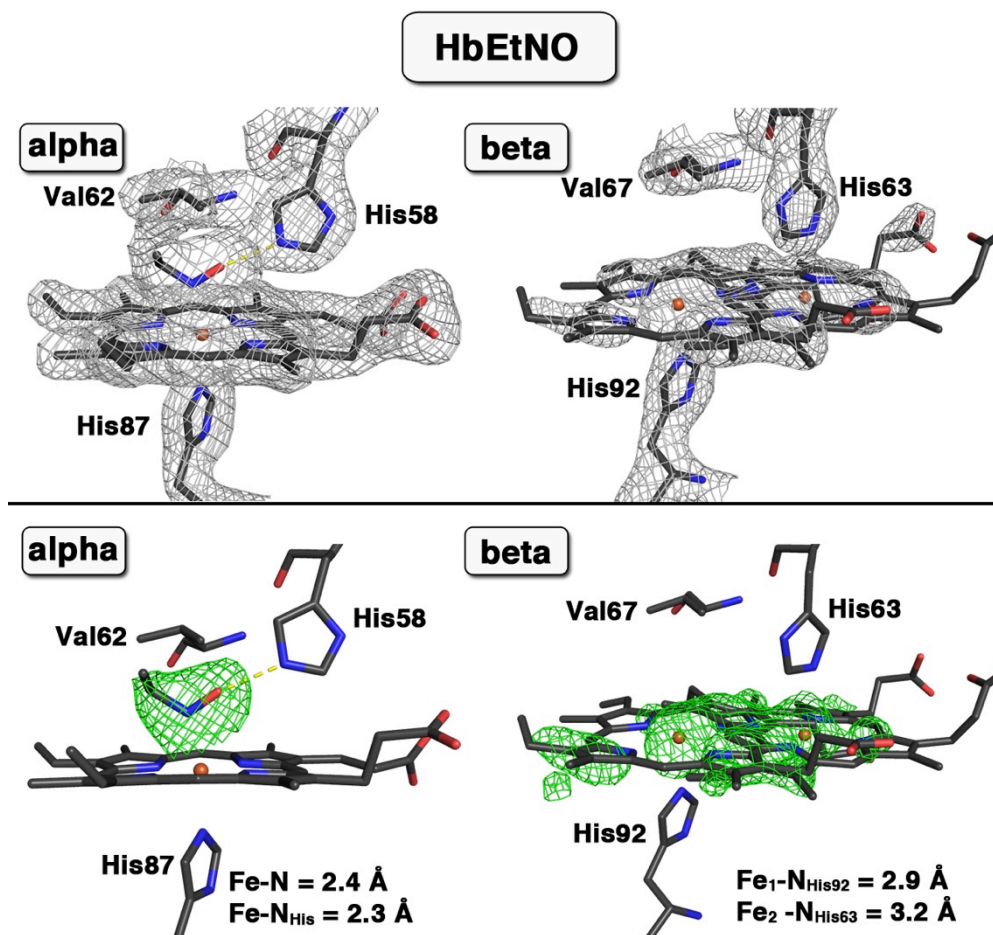
Figure 3.14. (*Top*) 2F_o–F_c electron density maps (grey mesh, contoured at 1.0σ), and (*Bottom*) F_o–F_c omit electron density maps (green mesh, EtNO groups, contoured at 3.0σ) and final models of the α and β active sites of the Hb(EtNO) complex (PDB accession code 4M4B, 2.0 Å resolution).

The 2F_o–F_c map of the α heme is consistent with the presence of the bound

nitrosoethane (EtNO) ligand. The C–C–N=O backbone of the EtNO ligand in the α

subunit is best modeled in the *trans* form with a torsion angle of –144.2°, with the

nitroso O atom H-bonded to the distal His58 residue and pointing in the direction of a

porphyrin N atom, and the hydrophobic Et group pointing towards the interior of the

subunit (Figure 3.15).

There are substantial structural differences between the α and β distal pockets in this Hb(EtNO) derivative. First, there is a notable lack of defined electron density for an ordered EtNO ligand in the β subunit of the structure (Figure 3.14). In addition, we had difficulty in modeling a single β heme in the distal pocket in its expected position. Consequently, we relied on an anomalous map that revealed two Fe positions, labeled Fe_1 and Fe_2 in Figure 3.16, in a 1:1 ratio that were 4.9 Å apart in the final model. The two Fe positions were used to model the core structures of the two hemes; we note that there was not enough observable electron density even in the $2F_o$-F_c map to accurately model the β hemes to determine if any chemical modifications had occurred in the porphyrin macrocycle.
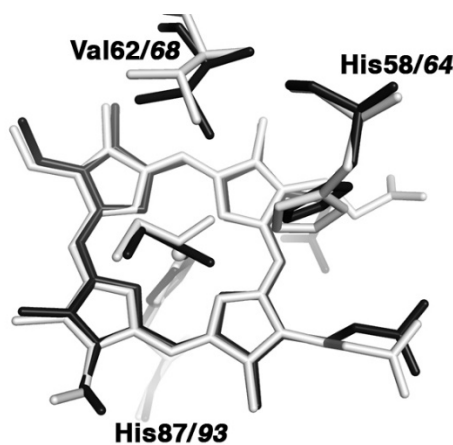
Figure 3.15. Overlay of the heme active sites of the beta subunit of Hb(EtNO) (light grey) and that of Mb(EtNO) (black), showing the relative orientations of the EtNO ligands. The residue numbers in italics are for Mb(EtNO).
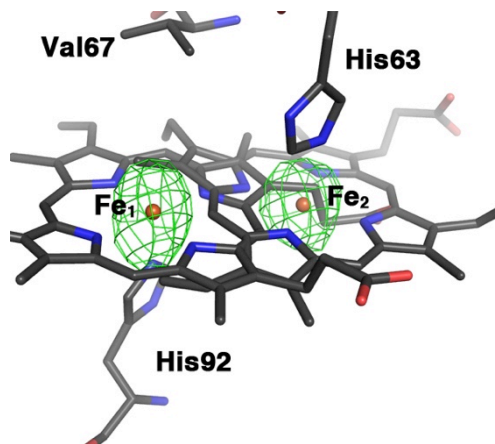
Figure 3.16. The Fe anomalous map (contoured at 3.0σ) and the final model of the β heme site of the Hb(EtNO) structure (PDB accession code 4M4B, 2.0 Å resolution). The occupancies of Fe_1 and Fe_2 are modelled at 50% for each position.

Importantly, the position of Fe_2 in Figure 3.16 places it in a position to interact weakly with the distal His63 residue (distance of 3.2 Å). This distal His63 imidazole ring experiences a twist of ~35° as it interacts weakly with the Fe_2 center. The proximal (His92)N–Fe_1 distance of 2.9 Å in the β subunit (c.f., 2.3 Å in the α subunit) is also long, and combined with the ~0.8 Å movement of the imidazole Nε atom towards the protein exterior, likely helps facilitate the departure of the heme from the β active site pocket.

The observation of heme slippage by 4.9 Å in the β subunit of the Hb(EtNO) product is remarkable. This lateral movement of the heme towards the protein exterior is similar to that (~4.8 Å) recently reported for an unusual Hb(ONO)$_{d,p}$ complex in which proximal ligand (nitrite) binding is present.[32] In the Hb(EtNO) structure, the F-helix in the β subunit remains ordered but with high B factor, suggesting its ability to unwind to allow the observed heme slippage.

It is likely the π-acidity of RNO plays a role in the degradation of the Hb(EtNO)

complex described here. Dithionite is known to cause degradation of dilute solutions of oxyHb.[33,34] However, we note that although both Hb(MeNO) and Hb(EtNO) complexes were prepared similarly in the presence of dithionite, only the Hb(EtNO) showed the heme slippage; thus making it unlikely that dithionite was the primary factor responsible for this phenomenon. Insight into the difference in apparent stability of the Hb(MeNO) vs. Hb(EtNO) is provided by the observation that the axial Fe–N bonds in Hb(EtNO) are slightly longer than those in the Hb(MeNO) analog (Figures 3.13 and 3.14), suggesting that the MeNO ligands are held tighter than EtNO to Fe in the crystal. This may help explain the observation of the heme degradation in Hb(EtNO) but not Hb(MeNO) under the conditions used.

We compared our human Hb(RNO) crystal structures with representative quaternary T, R, and R2 human Hb structures in terms of the root mean square deviation (rmsd) between the tetramers, as well as the critical contacts at the α1β2 interface that help define the description of the quaternary state. The rmsd between the different structures with least-square superposition of Cα of the tetramers (Table 3.2) suggest that the Hb(RNO) structures adopt the quaternary R conformation. Consistent with these results, the α1β2 interfaces, also a measure of quaternary matrix, of the Hb(RNO) structures are similar to those of the R state structures but different from the R2 or T structures (Figure 3.17).

In typical R state structures, the α1β2 dimer interface residue β2His97 lies between residues α1Thr41 and α1Thr38, which is what was observed in our ordered Hb(MeNO), although it lacked the R state H-bond interaction between the carbonyl atom of β2His97 and the hydroxyl of α1Thr38 (Figure 3.17). In the quaternary T state

structure, the α1β2 dimer interface rearranges, resulting in β2His97 jumping a turn to locate between α1Pro44 and α1Thr41, while in the *R2* structure the rearrangement of the α1β2 has moved β2His97 significantly away from both α1Thr41 and α1Thr38, although it is still located between these two residues.

Table 3.2. RMSD calculations[a]

	PDB i.d.	description	rmsd XYZ(Å)	ref.
Hb(EtNO)	4M4B (magenta)	*this work*	0.364	-
Hb(CO)	1AJ9 (red)	R state	0.475	35
deoxyHb[b]	1B86 (blue)	T state	2.544	36
Hb(CO)	1BBB (black)	R2 state	1.681	37
Hb(CO)	1YZI (cyan)	R3 state	1.72	38

[a] For this calculation, we fixed the Cα chains of the reference tetrameric Hb(MeNO) structure, and performed the rms deviations for Cα chains of the other tetrameric structures. [b] In complex with 2,3-DPG.
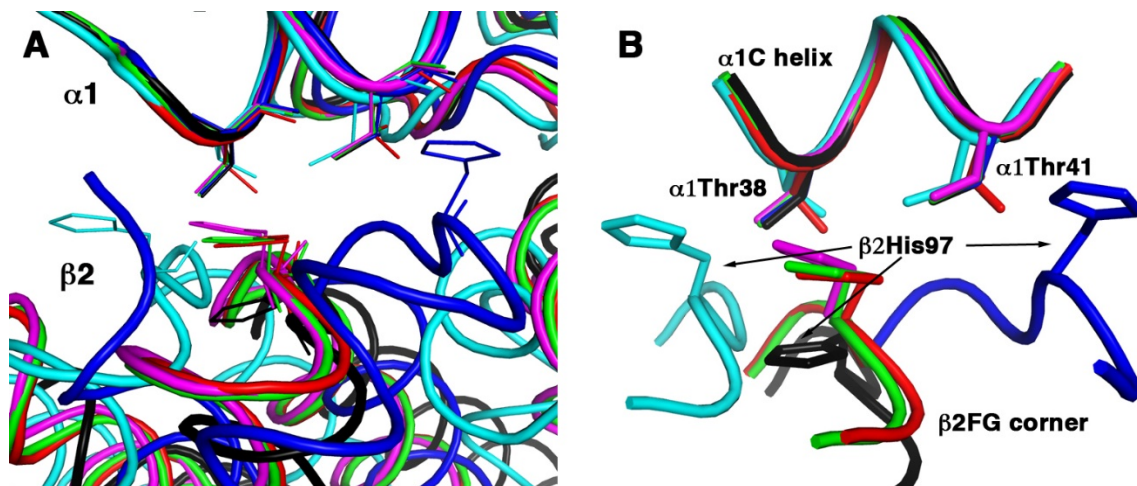
Figure 3.17. The α1β2 interface of representative Hb structures. (**A**) The α1β1 subunits were superimposed using a *T* state deoxy Hb structure as the reference (PDB accession code: 1B86, 2.5 Å resolution; shown in blue). This generates the same positions of the α1 C helices, but clearly shows different positions of the β2 FG corners for different quaternary structures. The *R* state Hb(CO) (PDB accession code: 1AJ9, 2.2 Å resolution) is shown in red; the R2 state Hb(CO) (PDB accession code: 1BBB, 1.7 Å resolution) is shown in black; and the R3 state Hb(CO) (PDB accession code: 1YZI, 2.07 Å resolution) is shown in cyan; the Hb(MeNO) (PDB accession code: 4M4A, 2.05 Å resolution; this work) is shown in green; the Hb(EtNO) (PDB accession code: 4M4B, 2.0 Å resolution; this work) is shown in magenta. (**B**) Highlights of key residues (α1Thr38, α1Thr41 and β2His97) at this α1β2 interface. This analysis shows that the Hb(RNO) structures are in the R state.

3.3.4 Crystallographic results of the sw MbH64A(NOAmph) complex

Crystals of the product from the (ferric) sw MbH64A with AmphNHOH (λ_{max}

426 nm; Figure 3.10) were generated by soaking pre-formed crystals of ferric sw

MbH64A (kindly provided by Bing Wang of our lab) with the AmphNHOH reagent.

We preferred this "crystal soaking method" over co-crystallization in this work since the

soaking method usually retains the same space group and unit cell of the crystal which

served the purpose of comparing the structures of the precursor ferric sw MbH64A and

its ferrous sw MbH64A-NOAmph product. We tried two different methods to

introduce the AmphNHOH reagent into the protein active site. The first method

90

involved the direct addition of solid AmphNHOH into the mother liquor containing the

sw MbH64A crystals, and the other method involved the addition of a solution of

AmphNHOH dissolved in methanol. When solid AmphNHOH was carefully added into

the solution containing the crystals, we observed the slow dissolution of the white

AmphNHOH powder over 2-3 hours, along with a color change of the dark red crystals

of sw MbH64A to a bright pink color. From our experience, this type of color change

indicates the reduction of ferric heme to the ferrous form. Although this color change

occurred using both approaches, only the crystals from the addition of solid

AmphNHOH gave good quality X-ray diffraction data.

The crystal structure of sw MbH64A(NOAmph) was solved to 1.73 Å

resolution. The F_o–F_c omit electron density map clearly shows the presence of a bulky

ligand in the active center (Figure 3.18). Fortunately, I had already obtained the

structure of (OEP)Fe(NOAmph)(1-MeIm) shown in Chapter 2, so the .cif file of the

ligand was used as a a model for the refinement of the NOAmph ligand in this protein

structure.
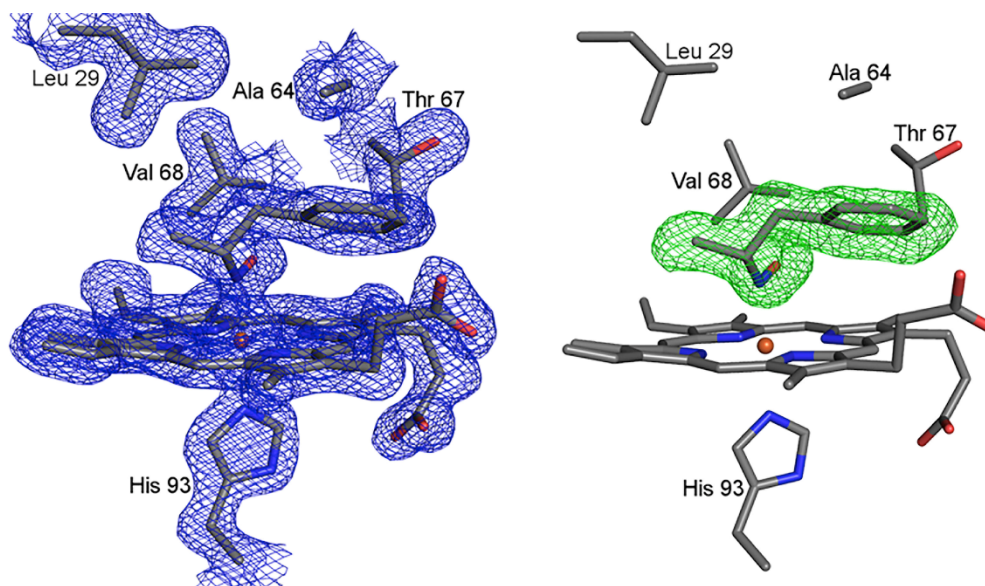
Figure 3.18. (*left*) $2F_o–F_c$ electron density maps (purple mesh, contoured at 1.0 σ), and (*right*) $F_o–F_c$ omit electron density maps (green mesh, NOAmph groups, contoured at 3.0 σ) and final models of the active site of the sw MbH64A(NOAmph) complex.

The NOAmph ligand binds to the Fe center via the N atom, similar to that observed in the other ferrous Hb(RNO) compounds discussed in the previous section. In the high resolution X-ray crystal structures of the heme model-NOAmph complexes discussed in Chapter 2, the Fe-N(NO) distances are in the 1.80-to-1.95 Å range, and are generally shorter than the Fe-N(axial *trans* ligand) distances (2.0-2.1 Å). The bond lengths in sw MbH64A(NOAmph) are very close to those observed in model complexes. In sw MbH64A(NOAmph), the Fe-N(NO) distance is 1.9 Å and the Fe-N(His) distance is 2.1 Å. Another feature that is consistent with the model complex is the orientation of the CNO plane of the NOAmph ligand that bisects adjacent porphyrin N atoms in both the model heme system complex and in sw MbH64A(NOAmph). Furthermore, the mutually *trans* CNO and 1-MeIm planes in sw MbH64A(NOAmph) are more eclipsed than staggered, a feature also observed in the model complexes in

Chapter 2. These structural similarities between the protein and model complexes are probably due the fact that the only significant interaction between the ligand and the heme is via the Fe-N bond. Indeed, no H-bonding interaction between ligand and distal pocket residues in the heme pocket of swMbH64A was observed. This lack of a H-bonding interaction between the ligand and the distal pocket is unusual, but not unexpected since the His64 residue was mutated to alanine (other distal pocket H-bonding residues include Thr67 and Y107). In contrast, H-bonding interactions between the nitroso O atoms with the distal His residues were observed in the Hb(RNO) derivatives (see earlier) and other wt Mb(RNO) complexes.[16] A notable exception was for the legHb(PhNO) crystal structure, where the large distal pocket did not favor direct H-bonding of the PhNO ligand with any distal pocket residue. [17] Figure 3.19 (*left*) shows an example of the H-bonding with distal His in the heme pocket of hhMb(EtNO). This H-bond helped stabilize the bound ligand and likely determines the orientation of the ligand. In the absence of this distal His residue (i.e., in the H64A mutant), this H-bonding is not present in the structure of sw MbH64A(NOAmph) (Figure 3.19) (*right*).
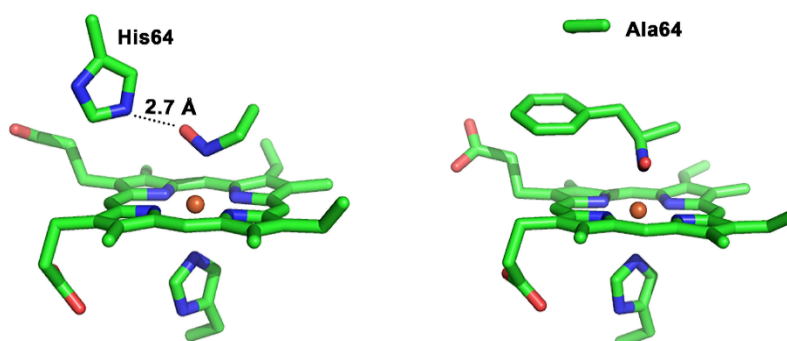
Figure 3.19. (*Left*) The H-bonding interaction between the nitroso O atom with the distal His in the heme site of hh Mb(EtNO). (*Right*) Lack of a H-bonding interaction stabilization of the NOAmph ligand in the heme site of sw MbH64A(NOAmph).

An unusual feature in the structure of sw MbH64A(NOAmph) is the orientation of the ligand in the heme pocket. In all the wt Hb(RNO) and Mb(RNO) crystal structures, the nitroso (N=O) moiety points outward towards solvent and is stabilized via H-bonding with the distal His residue, and the alkyl/aryl organic fragment pointes inwards towards the hydrophobic interior of the protein. In sw MbH64A(NOAmph) (Figure 3.19), the ligand is oriented with the nitroso moiety pointing inwards, and the hydrophobic/organic fragment pointing towards the polar solvent exterior. This ligand orientation was unexpected, as it is generally believed to be energetically unfavorable based on polarity arguments. *Why is the ligand orientated in such an unusual way?* One likely explanation is the steric effect of the ligand that would prevent the bulky Ph group to be accommodated in the distal pocket hydrophobic interior. To examine this further, we took the sw MbH46A(NOAmph) final model from the X-ray structure, and artificially rotated the NOAmph ligand in such a way to position it in the "normal expected" orientation with the bulky organic fragment in the distal pocket interior. We noted, surprisingly, that there were no significant steric clashes with any of the distal pocket residues. Clearly, more work needs to be done in this area to determine the factors that control ligand orientation in Mb complexes.

To better understand how the NOAmph ligand interacted with the active site of sw MbH64A, we compared the structures of sw MbH64A(NOAmph) with its precursor, ferric swMbH64A(H_2O) (Figure 3.20, provided by Bing Wang) in the same space group. Upon binding NOAmph in the ferrous form, the structure displayed conformational changes including the movement of the protein Cα atoms by as much as 1.5 Å. The rmsds (root mean square deviations) for these two structures are 0.27 Å for the 153

main-chain Cα atoms, and 0.67 Å for all atoms. In Figure 3.20 (*top*), it is observed that the CD loop of sw MbH64A(NOAmph) moved towards the solvent region, leaving a larger space for ligand access. Additional conformational changes were observed for the side-chains near or around the heme pocket. Figure 3.20 (*bottom*) shows the overlay of the heme sites in these two structures. Overall, the distal residues above the heme macrocycle moved upward, and the proximal residues below the heme moved slightly downward from their original positions. These changes were not unexpected, as the movements would enlarge the size of heme pocket allowing room for the ligand. Among these distal pocket residue movements, Val68 and Phe43 had the most significant displacements. Val68 is usually considered a kinetic barrier for ligand binding in Mb.[39] In our structure, the isopropyl group of Val68 was "pushed away" from the nitroso moiety of NOAmph, with a clockwise rotation of 109° to avoid a steric clash with the nitroso O-atom. The Phe43 residue displayed a displacement of 1.2 Å from its original position, moving away from the Ph group of NOAmph.
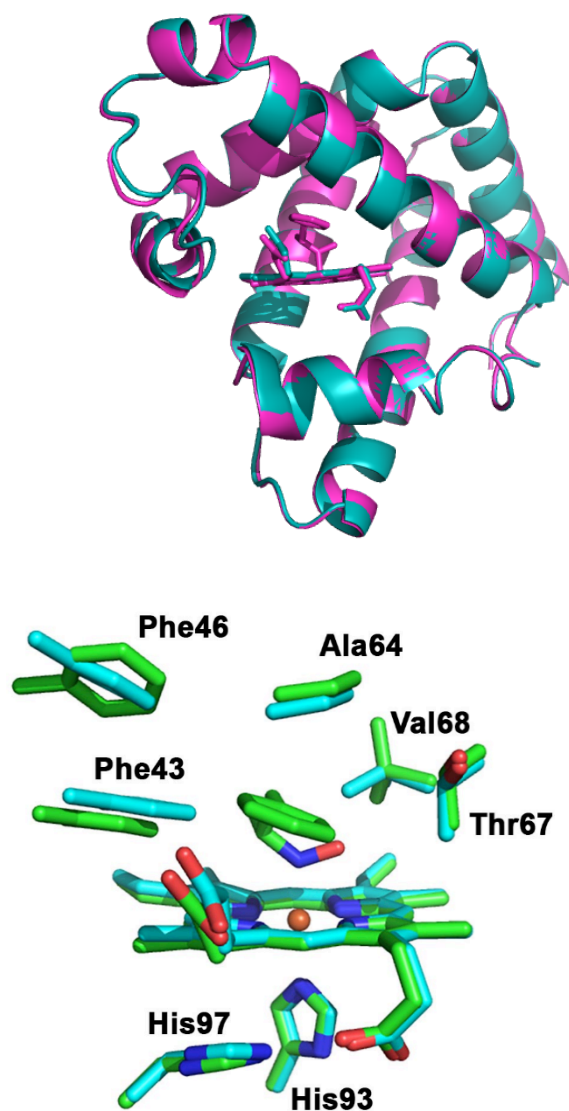
Figure 3.20. (*Top*) Overlay of the tertiary structures of sw MbH64A(NOAmph) (magenta) and ferric sw MbH64A(H_2O) (blue) showing the movement of the CD loop of the protein upon the ligand binding. (*Bottom*) Overlay of the heme sites in sw MbH64A(NOAmph) (green) and ferric sw MbH64A(H_2O) (blue) shown from the propionate side of the heme. The ligand of NOAmph is oriented toward the solvent exterior.
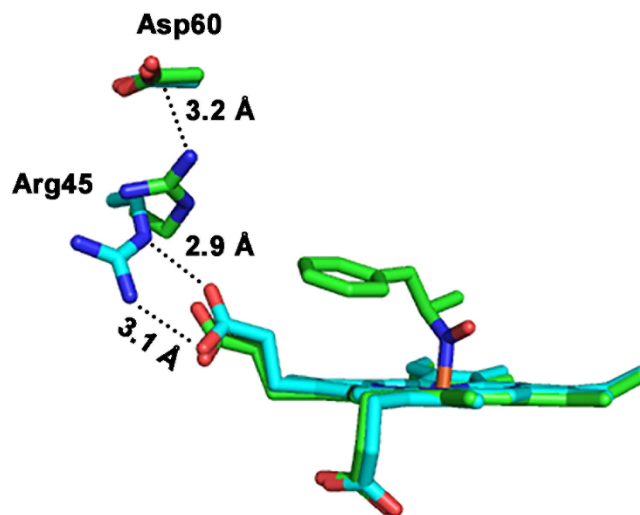
Figure 3.21. Overlay of the heme sites of sw MbH64A(H_2O) (blue) and sw MbH64A(NOAmph) (green) showing the disruption of the salt bridge between Arg45 and the heme propionate, with the formation of H-bonding between Arg45 and Asp60. The Arg45 in sw MbH64A(NOAmph) (green) flips towards Asp60.

We also noted, from the overlay of these two structures, the breaking of the salt bridge between Arg45 (positively charged) and a heme propionate side chain (negatively charge) upon binding of the NOAmph ligand with concomitant Fe reduction. The interaction between Arg45 and the heme propionate is known for its function of regulating ligand binding and stabilizing heme center in Mb.[40] Figure 3.21 shows the significant movement of Arg45 towards the C helix upon ligand binding. The heme propionate side chain in question also moved downwards slightly with the observation of a more flat heme macrocycle. These changes likely disrupted the H-bonding between $N\omega$(Arg)-O(propionate) and $N\varepsilon$(Arg)-O(priopionate). This disruption of the Arg-propionate salt bridge probably allowed for a more open access entry for the bulky NOAmph ligand into the pocket and binding to the Fe center. Interestingly, the

flip of Arg45 also led to the formation of a new salt bridge with the carboxylate oxygen of Asp60 shown in Figure 3.21.

We also compared the structure of sw MbH64A(NOAmph) with another Mb complex in the P6 space group containing a bulky ligand, namely sw MbH64A(CNC$_4$H$_7$) whose structure was reported by Smith *et al.* (pdb access code 103M).[41] In the reported structure, the hydrophobic alkyl chain of *n*-butyl isocyanide displayed the same outward-pointing orientation as the sw MbH64A(NOAmph) described in this work. However, there are some significant differences between these two structures.

The superposition of the tertiary and heme site structures of sw MbH64A(CNC$_4$H$_7$) and sw MbH64A(NOAmph) are shown in Figure 3.22. The Cα backbones of these two structures superimpose well. In both structures, the hydrophobic portions of the ligands were pointing outwards towards the solvent region. The Ph group of NOAmph and the butyl group of CNC$_4$H$_7$ bend towards the heme planes with a (N)C-C-C(Ph) angle of 120° (for NOAmph) and an N-C-C angle of 109° (for CNC$_4$H$_7$).

One important difference is the distance between Arg45 and heme propionate side chains in these two structures. As discussed above, the addition of NOAmph as a ligand in sw MbH64A(NOAmph) disrupted the Arg45-propionate salt bridge to likely assist in ligand access and binding. In contrast, in sw MbH64A(CNC$_4$H$_7$), the N$_\omega$(Arg)-O(priopionate) distance was shortened by 0.4 Å after ligand binding (Figure 3.22, *bottom*).
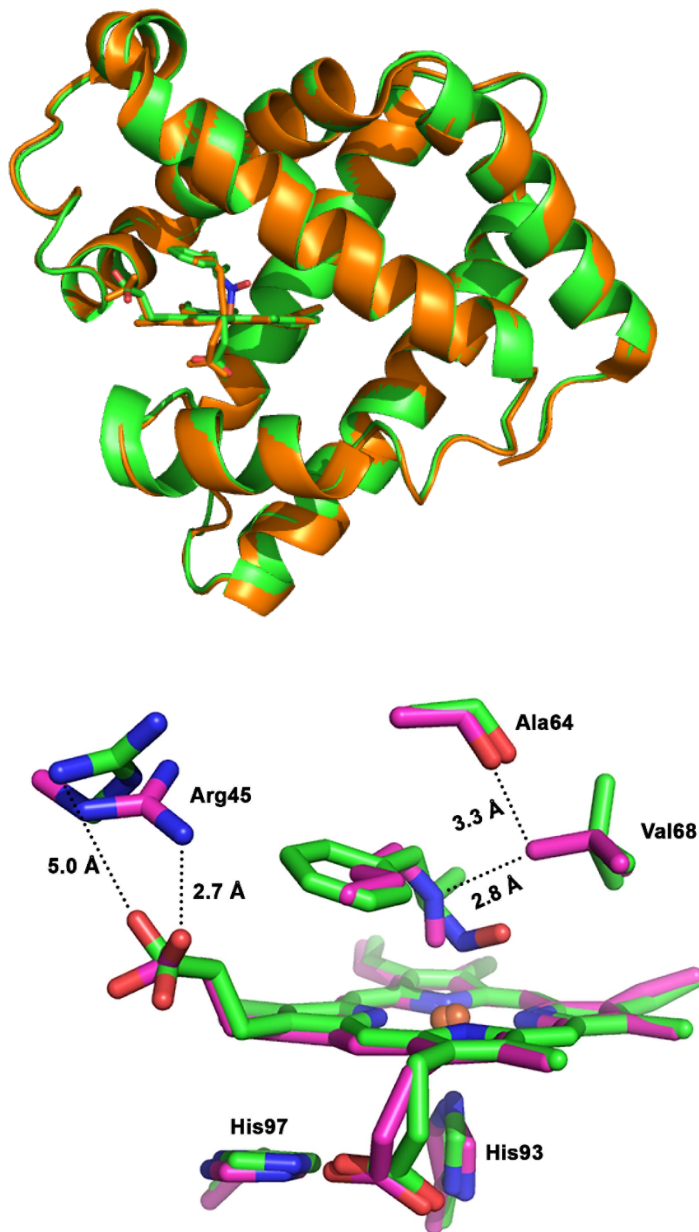
Figure 3.22. (*Top*) Overlay of the tertiary structures of sw H64AMb(CNC$_4$H$_7$) (orange; PDB accession code: 103M, 2.0 Å resolution) and sw MbH64A(NOAmph) (green). (*Bottom*) Overlay of the heme sites in sw MbH64A(CNC$_4$H$_7$) (magenta) and sw MbH64A(NOAmph) (green) shown from the propionate side of the heme. The *n*-butyl isocyanide and NOAmph ligands show similar outward-pointing orientations. In the structure of sw MbH64A(CNC$_4$H$_7$), the ligand N-atom H-bonds to Val68.

Also, it is evident from Figure 3.22 that the Val68 of sw MbH64A(CNC_4H_7) did not alter its original position after ligand binding. Instead of rotating away from the ligand as seen for sw MbH64A(NOAmph), the Val68 is within a H-bond interaction (distance of 2.9 Å) with the CNC_4H_7 ligand.

In this work, we first studied the reactions between Hb and a series of simple RNO (R = Me, Et, Pr, ^iPr) compounds by UV-vis spectroscopy, and reported the first crystal structures of RNO derivatives of human Hb, which reveal structural distortions that will lead to the biologically relevant heme loss process.

The ability of Mb to bind with NOAmph was also examined using both UV-vis spectroscopy and X-ray crystallography. The results indicated that despite the relatively small active site of myoglobin, it could still react with NOAmph and form a Fe^{II}-NOAmph protein complex. In addition, the crystal structure of sw MbH64A(NOAmph) was successfully obtained, which represents the first crystal structure of any heme protein in complex with an amphetamine derivative.

3.4 References

(1)   Hata, Y.; Watanabe, M.; Tonda, K.; Hirata, M. *Chem Biol Interact* **1987**, *63*, 171.

(2)   Wright, J.; Cho, A. K.; Gal, J. *Xenobiotica* **1977**, *7*, 257.

(3)   Cashman, J. R.; Xiong, Y. N.; Xu, L.; Janowsky, A. *J Pharmacol Exp Ther* **1999**, *288*, 1251.

(4)   Mansuy, D.; Beaune, P.; Chottard, J. C.; Bartoli, J. F.; Gans, P. *Biochem*

Pharmacol **1976**, *25*, 609.

(5)   Franklin, M. R. *Xenobiotica* **1974**, *4*, 143.

(6)   James, R. C.; Franklin, M. R. *Biochem Pharmacol* **1975**, *24*, 835.

(7)   Mahy, J. P.; Mansuy, D. *Biochemistry* **1991**, *30*, 4165.

(8)   Harrison, J. H.; Jollow, D. J. *Mol Pharmacol* **1987**, *32*, 423.

(9)   Mansuy, D.; Rouer, E.; Bacot, C.; Gans, P.; Chottard, J. C.; Leroux, J. P. *Biochem Pharmacol* **1978**, *27*, 1129.

(10)   Bensoussan, C.; Delaforge, M.; Mansuy, D. *Biochem Pharmacol* **1995**, *49*, 591.

(11)   Delaforge, M.; Jaouen, M.; Mansuy, D. *Biochem Pharmacol* **1983**, *32*, 2309.

(12)   Peter, E.; Michaela, A. *Biol Chem Hoppe-Seyler* **1987**, *368*, *285*.

(13)   Khan, M. F.; Wu, X.; Ansari, G. A. S. *J. Toxicol. Environ. Health* **2000**, *60A*, 263.

(14)   Chakrapani, H.; Bartberger, M. D.; Toone, E. J. *J Org Chem* **2009**, *74*, 1450.

(15)   Percy, M. J.; McFerran, N. V.; Lappin, T. R. J. *Blood Rev* **2005**, *19*, 61.

(16)   Richter-Addo, G. B.; Copeland, D. M.; West, A. H. *J Inorg Biochem* **2003**, *96*, 216.

(17)   I. P. Kuranova, A. V. T., G. V. Obmolova, A. A. Voronova, A. N. Popov, D. M. Kheiker and E. G. Arutyunyan *Bioorg. Khim.* **1982**, *8*, 1625.

(18)   Antonini, E.; Brunori, M. Hemoglobin and myoglobin in their reactions with ligands. Amsterdam, Netherlands: North-Holland Pub. Co.; **1971**.

(19)   Safo, M.; Abraham, D. *Methods Mol. Med.*, **2003**, 82, 1

(20)   Goudgaon, N. M.; Wadgaonkar, P. P.; Kabalka, G. W. *Synth Commun* **1989**, *19*,

805.

(21)   Pflugrath, J. *Acta Cryst.* **1999**, *D55*, 1718.

(22)   McCoy, A. J.; Grosse-Kunstleve, R. W.; Adams, P. D.; Winn, M. D.; Storoni, L. C.; Read, R. J. *J. Appl. Cryst.* **2007**, *40*, 658.

(23)   Yi, J.; Safo, M. K.; Richter-Addo, G. B. *Biochemistry* **2008**, *47*, 8247.

(24)   Murshudov, G. N.; Vagin, A. A.; Dodson, E. J. *Acta Cryst.* **1997**, *D53*, 240.

(25)   Adams, P. D.; Afonine, P. V.; Bunkoczi, G.; Chen, V. B.; Davis, I. W.; Echols, N.; Headd, J. J.; Hung, L. W.; Kapral, G. J.; Grosse-Kunstleve, R. W.; McCoy, A. J.; Moriarty, N. W.; Oeffner, R.; Read, R. J.; Richardson, D. C.; Richardson, J. S.; Terwilliger, T. C.; Zwart, P. H. *Acta Cryst.* **2010**, *D66*, 213.

(26)   Emsley, P.; Lohkamp, B.; Scott, W. G.; Cowtan, K. *Acta Cryst.* **2010**, *D66*, 486.

(27)   Engh, R. A.; Huber, R. *Acta Cryst.* **1991**, *A47*, 392.

(28)   Chen, V. B.; Arendall, W. B.; Headd, J. J.; Keedy, D. A.; Immormino, R. M.; Kapral, G. J.; Murray, L. W.; Richardson, J. S.; Richardson, D. C. *Acta Cryst.* **2010**, *D66*, 12.

(29)   Mansuy, D.; Chottard, J. C.; Chottard, G. *Eur J Biochem* **1977**, *76*, 617.

(30)   Lee, J.; Chen, L.; West, A. H.; Richter-Addo, G. B. *Chem Rev* **2002**, *102*, 1019.

(31)   Scott, E. E.; Gibson, Q. H.; Olson, J. S. *J Inorg Biochem* **2001**, *276*, 5177.

(32)   Yi, J.; Thomas, L. M.; Safo, M. K.; Richter-Addo, G. B. *Biochemistry* **2011**, 50, 8323

(33)   Dalziel, K.; O'Brien, J. R. P. *Biochem J* **1957**, *67*, 119.

(34)   Dalziel, K.; O'Brien, J. R. P. *Biochem J* **1957**, *67*, 124.

(35)   Vasquez, G. B.; Ji, X.; Fronticelli, C.; Gilliland, G. L. *Acta Cryst* **1998**, D54, 355

(36)   Richard, V.; Dodson, G. G.; Manguen, Y. *J Mol Biol* **1993**, 233, 270

(37)   Silva, M. M.; Rogers, P. H.; Arnone, A. *J Biol Chem* **1992**, 267, 17248

(38)   Safo, M. K.; Abraham, D. J. *Biochemisty* **2005**, 44, 8347

(39)   Egeberg, K. D.; Springer, B. A.; Sligar, S. G.; Carver, T. E.; Rohlfs, R. J.; Olson, J. S. *J Biol Chem* **1990**, *265*, 11788.

(40)   Neya, S.; Funasaki, N.; Igarashi, N.; Ikezaki, A.; Sato, T.; Imai, K.; Tanaka, N. *Biochemistry* **1998**, *37*, 5487.

(41)   Smith, R. D.; Blouin, G. C.; Johnson, K. A.; Phillips, G. N.; Olson, J. S. *Biochemistry* **2010**, *49*, 4977.

Chapter 4. Interactions between nitric oxide and formally d^6 metalloporphyrins of cobalt and rhodium

4.1 Introduction

As mentioned in Chapter 1, NO is a biological signaling molecule that interacts with heme proteins.[1,2] Iron is the metal center of heme proteins. Not surprisingly, most of the previous research on the interactions between NO and heme models has involved Fe and other group 8 metals as the central metal of the metalloporphyrins.[3-7] Cobalt also plays an important role in biology in the form of cobalamin,[8,9] and Co^{III} is isoelectronic with Fe^{II}. Surprisingly, the study on the interactions between NO and cobalt porphyrins has been very limited to date. To the best of our knowledge, only five-coordinated nitrosyl cobalt porphyrin complexes of the form (por)Co(NO) have been structurally characterized and reported.[10] The study on the interactions of NO and porphyrins containing other group 9 metals, such as rhodium and iridium, is even more rare. In fact, there is only one literature report on the preparation and EPR studies of the nitrosyl rhodium porphyrin ((TPP)RhNO), which dates back 35 years.[11]

The lack of knowledge in this area was surprising to us. Could it be that the bonds between NO and the metal centers of Co/Rh porphyrins may not be as strong as those of the group 8 metal porphyrins, thus making their complexes difficult to obtain? Our goal in this chapter is to gain an understanding of this "unknown" area.

4.2 Experimental section

4.2.1 Materials, instrumentation, and methods

The reactions were performed under anaerobic conditions using standard Schlenk techniques under an atmosphere of nitrogen and/or in an Innovative Technology Labmaster 100 Dry Box unless stated otherwise. Solvents used for the reactions were obtained from an Innovative Technology Pure Solv 400-5-MD Solvent Purification system under an atmosphere of nitrogen. The Tensor 27 FTIR spectrometer equipped with a mid-IR fiber-optic dip probe and liquid nitrogen cooled MCT detector (RemSpec Corporation, Sturbridge, MA, USA) was used to record the infrared spectra of solution samples. Proton NMR spectra were recorded on a Varian Mercury VX 300 MHz spectrometer at room temperature, and the signals were referenced to the solvent employed (CDCl$_3$ at 7.24 ppm). UV-vis data were collected on an HP 8453 diode array instrument. X-ray diffraction data were collected by Dr. Douglas R.Powell using a diffractometer with a Bruker APEX ccd area detector[12,13] and graphite-monochromated Mo Kα radiation (λ = 0.71703Å).

Hydrochloric acid (37%) was purchased from EMD chemicals; cobalt(II) *meso*-tetraphenylporphine was purchased from Strem; benzonitrile (99%), tetrabutyltin (93%), methanol (99.8%), methanol (anhydrous, 99.8%) and anhydrous ethanol were purchased from Aldrich; dichloromethane, acetonitrile, benzene and hexane were collected from the solvent distillation system under nitrogen; chloroform was purchased from Fisher; silica gel (Mesh 60-200) was purchased from Baker; anhydrous sodium acetate, di-μ-chlorotetraethylene dirhodium (I) and rhodium (III) chloride hydrate were purchased from Aldrich; chloroform-*d* (99.8%) was purchased from Cambridge Isotope

Laboratories. Nitric oxide (98%, Matheson Gas) was purified by passing the gas through a column of KOH pellets followed by a cold trap (acetone/dry ice, -78°C) to eliminate higher nitrogen oxides. TPPH$_2$ (TPP = 5, 10, 15, 20-tetraphenylporphyrinato dianion) was prepared following literature methods.[14]

(TPP)CoCl was prepared by a literature method[15] and crystallized from CH$_2$Cl$_2$/hexane.

4.2.2 Synthesis

(TPP)Co(n-Bu)(1) : The compound (TPP)Co(*n*-Bu) was prepared following published method.[16] Tetrabutyltin (Sn(*n*-Bu)$_4$, 18 mg, 0.05 mmol) was added to a chloroform/acetonitrile (5:1) solution of (TPP)CoCl (36 mg, 0.05 mmol) in a Schlenk tube. The Schlenk tube was kept in the dark by wrapping it tightly with aluminum foil. After stirring for 3 hours, the solution turned to a red color. It was then taken to dryness in vacuo and the residue was washed with hexane. The slow evaporation of a CH$_2$Cl$_2$/hexane (1:1) solution of the residue in a glove box resulted in the formation of block shaped red/black crystals of (TPP)Co(*n*-Bu). The isolated yield of the crystals is 98%. ^{1}H NMR (CDCl$_3$, ppm): 8.75 (s, 8H, pyrrole-H of TPP), 8.10 (m, 8H, *o*-H of TPP), 7.72 (m, 12H, *p/m*-H of TPP), -0.71 (t, 3H of Bu), -1.33 (m, 2H of Bu), -4.63 (m, 2H of Bu), -3.65 (t, 2H of Bu),. UV-vis (CH$_2$Cl$_2$, λ/nm): 408, 531. IR (KBr, cm^{-1}): 1697 s, 1653 m, 1598 s, 1559 w, 1540 m, 1457 s, 1440 s, 1375 m, 1351 s, 1174 m, 1156 w, 1111 w, 1072 s, 998 s, 798 s, 752 s, 718 w, 701 s.

Attempted preparation of (TPP)Co(NO)(n-Bu)(2): Crystals of (TPP)Co(*n*-Bu) were carefully selected and placed in a small glass vial. The vial and its contents were sealed with an air-tight septum and electrical tape. It was purged with nitrogen through a needle

for 2 hours to remove the oxygen inside the vial. NO gas was then introduced into the vial through a needle for 20 mins to ensure that the glass vial was filled with NO, and the vial contents were kept under NO for more than one week. An X-ray crystal structural determination of the product did not indicate the binding of NO to the metal center of (TPP)Co(n-Bu). However, we observed the formation of a new peak in the IR-spectrum, which was assigned to (TPP)Co(NO). IR (KBr, cm^{-1}): υ_{NO} =1682 s m; also 1696 m, 1634 s, 1600 w, 1557 w, 1540 w, 1462 s, 1384 m, 1351 s, 1175 w, 1074 s, 1004 s, 799 s, 753 s, 701 s, 667 m.

(TPP)Rh(Ph)(3): The compound of (TPP)Rh(Ph) was prepared following a published method with slight modification.[17] To a 5 mL CH$_2$Cl$_2$ solution of Rh$_2$(CO)$_4$Cl$_2$ (125 mg, 0.06 mmol) in a Schlenk tube was added TPPH$_2$ (25 mg, 0.04 mmol) and anhydrous NaOAc (125 mg, 1.5 mmol). The solution was stirred for an hour under a flow of nitrogen until the solvent completely evaporated. This procedure was repeated with the addition of another 5 mL CH$_2$Cl$_2$ into the Schlenk tube. The black red residue was dissolved in CH$_2$Cl$_2$ and filter-cannulated to another Schlenk tube under nitrogen. After taking the contents to dryness in vacuo, 30 mL of benzene was added to dissolve the solid and the mixture was heated to 80 °C for 8 hours in the dark in the presence of trace air. The air was introduced by connecting the Schelnk tube to air through a needle placed on the septum. A black precipitate formed on the bottom of Schlenk tube during the reaction. After cooling the reaction vessel down to room temperature, the solution was filtered and concentrated to 2 mL before loading on a silica column (1 x 15 cm) that was prepared in benzene/hexane (2:1). The product was then eluted using a concentration gradient of increasing benzene (from 65% to 75%). The second visible

fraction of the eluent was collected and identified as (TPP)Rh(Ph) by UV-vis spectroscopy. This fraction was taken to dryness in vacuo and the product obtained in 45% yield. The slow evaporation of a CH_2Cl_2/hexane (1:1) solution of the product in a glove box resulted in the formation of red block-shaped crystals in 3 days. UV-vis (CH_2Cl_2, λ/nm): 412, 520. ^{1}H NMR ($CDCl_3$, ppm): 8.68 (s, 8H, pyrrole-H of TPP), 8.09 (d, 8H, *o*-H of TPP), 7.67 (m, 12H, *p/m*-H of TPP), 5.19 (t, 1H, *p*-H of C_6H_5), 4.70 (t, 2H, *m*-H of C_6H_5), 0.21 (d, 2H, *o*-H of C_6H_5). IR (KBr, cm^{-1}): 1633 m, 1595 m, 1560 w, 1537 w, 1488 w, 1470 s, 1442 s, 1351 s, 1306 m, 1261 w, 1027 w, 1175 w, 1073 s, 1011 s, 796 s, 756 s, 703 s, 656 w.

(TPP)Rh(Ph)(CH₃OH): A slow evaporation of a solution of (TPP)Rh(Ph) in CH_2Cl_2/methanol in a glove box over 3 days resulted in the formation of orange plate-shaped crystals, which was determined, by X-ray crystallography, to be (TPP)Rh(Ph)(CH$_3$OH).

(TPP)Rh(NO)(Ph): Crystals of (TPP)Rh(Ph)(CH$_3$OH) were carefully picked and placed in a small glass vial. The vial and its contents were sealed with an air-tight septum and secured by electrical tape. It was purged with nitrogen through a needle for 2 hours to remove the trapped air. NO gas was then introduced into the vial through a needle for 20 mins to ensure the glass vial was filled with NO, and the vial contents kept under NO for more than one week. The crystals were then harvested under argon. IR (KBr, cm^{-1}): υ_{NO} = 1811 w; also 1596 s, 1561 s, 1535 m, 1470 m, 1440 s, 1397 w, 1351 s, 1321 m, 1308 s, 1260 w, 1207 m, 1176 s, 1073 s, 1010 s, 796 s, 752 s, 700 s, 657 m.

A similar experiment was also performed with the five-coordinate (TPP)Rh(Ph) crystals. No formation of nitrosyl complex was observed for the later complex using X-ray crystallography.

(TPP)RhCl: (TPP)RhCl was prepared by a published method.[18] To a 10 mL PhCN solution of $RhCl_3 \cdot H_2O$ (0.104 g, 0.50 mmol) was added H_2TPP (0.157 mg, 0.51 mmol). The mixture was refluxed in air for 3 hours, during which time the color of the solution changed from purple to red. The mixture was taken to dryness in vacuo and re-dissolved in a small amount of CH_2Cl_2 to load onto a silica column (1 x 15 cm) prepared in CH_2Cl_2. The column was washed with a gradient elution of CH_2Cl_2/PhCN. Three fractions were eluted and were examined by UV-vis spectroscopy. The second fraction, which was identified as the known (TPP)RhCl, was collected. The eluent was dried in vacuo and the red residue was re-dissolved in a mixture of methanol and CH_2Cl_2. A slow evaporation of this solution in a dry box gave a mixture of purple block-shaped crystals and red plate-shaped crystals. The isolated yield of the crystals is ~70%. Both of the crystals were examined by X-ray crystallography. Only the block-shape crystals gave good X-ray diffraction data, and the compound was determined to be the expected product (TPP)RhCl(CH_3OH). UV-vis of (TPP)RhCl (CH_2Cl_2, λ /nm): 422, 533, 568. IR (KBr, cm^{-1}): 1652 w, 1635 w, 1595 s, 1538 m, 1488 w, 1439 s, 1352 s, 1310 s, 1207 m, 1176 s, 1072 s, 1012 s, 795 s, 754 s, 703 s, 666 w.

Preparation of (TPP)Rh(NO)Cl: The preparation of (TPP)Rh(NO)Cl followed the same procedure described for Rh(TPP)(NO)(Ph). Crystals of (TPP)RhCl were exposed to NO at room temperature for two weeks in an anaerobic environment. A product crystal was harvested under argon for an X-ray diffraction study. IR (KBr, cm^{-1}): $\upsilon_{NO} = 1732$ w;

also 1633 w, 1594 m, 1538 s, 1439 s, 1397 w, 1352 s, 1309 m, 1261 s, 1206 m, 1175 s, 1071 s, 1012 s, 795 s, 754 s, 703 s.

(OEP)Rh(CH₂Cl): This chemical was purchased commercially as "(OEP)RhCl" from Frontier Science. The "(OEP)RhCl" we received was shown by UV-vis and ^{1}H NMR spectroscopy to be a different chemical from what we initially expected. A slow evaporation of a CH_2Cl_2/hexane/methanol (7:1:1) solution of this chemical in a glove box resulted in the formation of crystals with a tree-like architecture in 3 days. The crystals were carefully selected and cut under a microscope. It was identified by X-ray crystallography as (OEP)Rh(CH₂Cl). ^{1}H NMR (CDCl₃, ppm): 10.11 (s, 4H, meso-H of OEP), 4.05 (m, 16H, *CH₂*CH₃ of OEP), 1.90 (t, 24H, CH₂*CH₃* of OEP), -3.31 (d, 2H, C*H₂*Cl). UV-vis (CH_2Cl_2, λ/nm): 394, 511, 543. IR (KBr, cm^{-1}): 1652 w, 1549 m, 1464 s, 1449 s, 1381 s, 1318 w, 1271 s, 1228 m, 1153 s, 1110 m, 1055 s, 1020 s, 995 s, 962 s, 845 s, 747 m.

Attempted preparation of (OEP)Rh(NO)(CH₂Cl): The attempted preparation of (TPP)Rh(NO)Cl followed the same procedure described for (TPP)Rh(NO)(Ph) using a gas-solid method. However, the X-ray diffraction data collected on the crystals were not of sufficient quality for structure determination.

(TPP)Rh(C₆H₄Cl): This chemical was commercially purchased as " (TPP)Rh" from Frontier Science. The "(TPP)Rh" we received was shown by UV-vis and ^{1}H NMR spectroscopy to be a different chemical from what we initially expected. A slow evaporation of a CH_2Cl_2/methanol (4:1) solution of this compound in glove box resulted in the formation of plate-shaped crystals which were determined by X-ray crystallography to be a mixture of (TPP)Rh(*p*-C₆H₄Cl) and (TPP)Rh(*m*-C₆H₄Cl) (9:1).

^{1}H NMR (CDCl$_3$, ppm) of (TPP)Rh(p-C$_6$H$_4$Cl): 8.75 (s, 8H, pyrrole-H of TPP), 8.12 (m, 8H, o-H of TPP), 7.72 (m, 12H, p, m-H of TPP), 4.76 (d, 2H, m-H of C$_6$H$_4$Cl), 0.17 (d, 2H, o-H of C$_6$H$_4$Cl). UV-vis (CH$_2$Cl$_2$, λ / nm): 413, 521, 634. IR (KBr, cm^{-1}): 1649 s, 1635 s, 1557 m, 1539 m, 1467 m, 1441 m, 1384 s, 1352 s, 1308 m, 1258 w, 1177 w, 1076 s, 1047 w, 1010 vs, 839 w, 796 s, 753 s, 702 s.

(TPP)Rh(NOC$_6$H$_4$Cl): The preparation of (TPP)Rh(NOC$_6$H$_4$Cl) followed the same procedure described for Rh(TPP)(NO)(Ph). Crystals of (TPP)Rh(C$_6$H$_4$Cl) were exposed to NO at room temperature for two weeks in an anaerobic environment, during which time the crystals turned to a darker color. The crystal was harvested under argon for an X-ray diffraction study. IR (KBr, cm^{-1}): υ_{NO} = 1414; also 1632 s, 1574 w, 1556 w, 1538 w, 1462 w, 1348 s, 1265 m, 1083 s, 1012 w, 866 s, 802 w, 736 w.

((NO$_2$)$_2$TPP)Rh(Ph): NO gas was introduced into a 3 mL CH$_2$Cl$_2$ solution of Rh(TPP)Ph (3 mg, 0.003 mmol) in a Schlenk tube through a needle over a 25 min period. The solution changed from bright orange to a dark red color. The excess NO was then flushed away by N$_2$, and ~2 mL hexane was added into the Schlenk tube. A slow evaporation of this solution in a glove box resulted in the formation of violet block-shaped crystals over a period of three days. The crystals were harvested in air for an X-ray diffraction study. IR (KBr, cm^{-1}): 1632 m, 1538 s, 1469 m, 1454 m, 1443 m, 1346 m, 1261 s, 1175 w, 1158 w, 1097 m, 1074 m, 1032 m, 1031 m, 798 s, 754 w, 701 m, 639 w.

4.2.3 Infrared spectral monitoring of the reactions of the (por)Rh(R) compounds with NO

The following is representative: Approximately 3 mg of a powered sample of the (por)Rh(R) was placed into a Schlenk tube equipped with an air-tight septum. The

tube was placed under vacuum for 30 mins and re-filled with nitrogen. CH_2Cl_2 (3 mL) was carefully added into the schlenk tube via an air-tight syringe to completely dissolve the reagent. NO gas was introduced into the solution using a gas-tight syring needle over a 25 min period. The solution was transferred to a glass vial protected by a blanket of nitrogen using an air-tight syringe to record its IR spectrum.

For the spectral recording, a mid-IR fiber-optic dip probe was placed inside a small glass vial that was sealed in a clear ziplock bag. The ziplock bag was pre-purged with nitrogen for 1.5 hrs to remove any air. A blanket of N_2 was maintained in and over the glass vial throughout the experiment. A background spectrum was taken with the N_2. The product solution was transferred into the glass vial through an air-tight syringe under the protection of N_2.

4.3 Results and discussion

### 4.3.1 Synthesis and characterization

In this chapter, I describe the preparations and structural characterizations of a series of cobalt(III) and rhodium(III) porphyrins, including (TPP)RhCl, (TPP)Co(n-Bu), (TPP)Rh(Ph), (TPP)Rh(C_6H_4Cl) and (OEP)Rh(CH_2Cl). Although the preparations of these precursor compounds have been reported by others previously, their crystal structures reported here were previously unknown. Importantly, these compounds were used by me as precursors for the reactions with NO gas to generate a previously unreported class of group 9 (por)Rh(NO)X derivatives.

The known (TPP)RhCl complex was prepared by treating H_2(TPP) with $RhCl_3 \cdot H_2O$ in a solution of PhCN (eq. 4.1).[18] It was isolated in 70% yield after purification by column chromatography. Interestingly, both red needle-like and purple

112

block-shaped crystals grew simultaneously from a solution of the product in

$CH_2Cl_2/MeOH$. While these two types of crystals are different in shape and color, both

of them were identified by UV-vis spectroscopy to be (TPP)RhCl (Table 4.1).

Unfortunately, only the purple block-shaped crystals were of sufficient quality for X-ray

diffraction data collection.

(4.1)
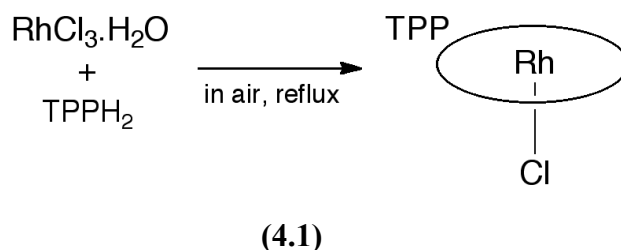
The crystal structure of (TPP)RhCl with a coordinated methanol in the axial

position is shown in Figure 4.1. The Rh-Cl bond length is 2.305 (19) Å. The axial Cl

atom displays a weak electrostatic interaction with a MeOH solvate molecule. A 3.45 Å
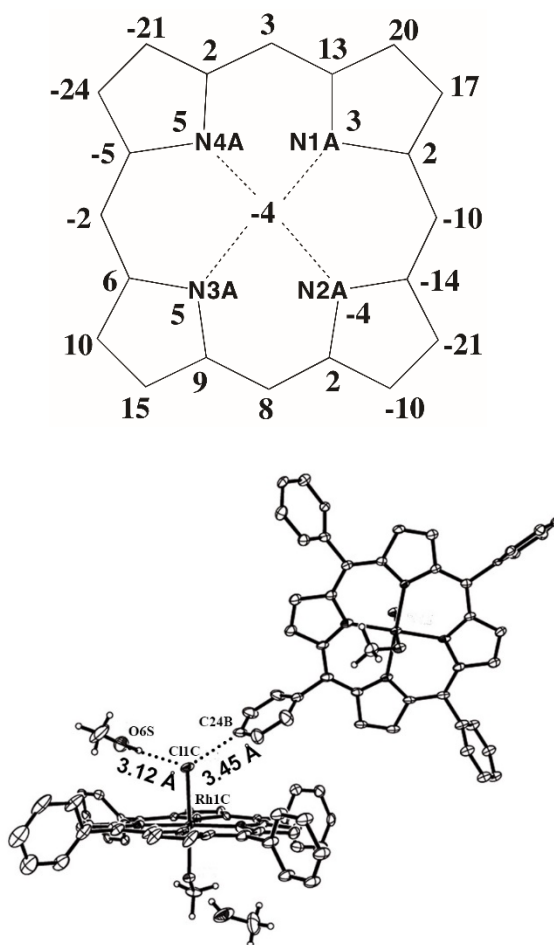

113
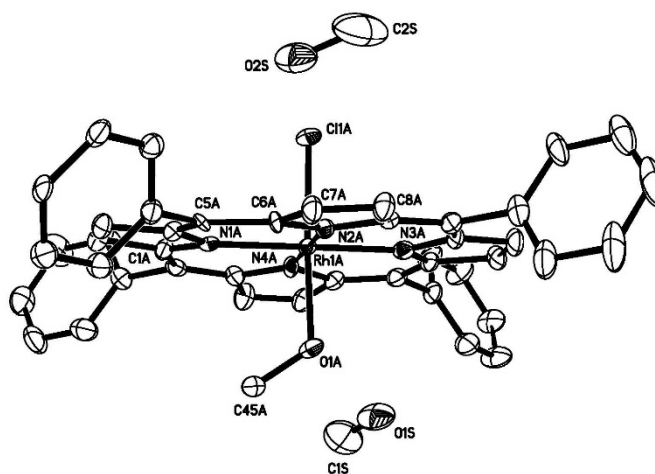
Figure 4.1. (*Top*) Molecular structure of (TPP)RhCl(MeOH). Hydrogen atoms have been omitted for clarity. (*Middle*) Perpendicular atom displacements (in units of 0.01 Å) of the porphyrin core atoms from the 24-atom mean porphyrin plane. (Bottom) The relative orientation of (TPP)RhCl(MeOH) and a neighboring MeOH and porphyrin.

distance between this Cl atom and a porphyrin phenyl group is outside of the range for a

normal hydrogen bond.

The alkyl and aryl σ-bonded d^6 group 9 metal (Co, Rh) porphyrins employed in

this chapter were prepared by previously reported methods.[16,17] The first method

involves the reaction of a main-group alkylating reagent with halogencobalt

(III)/halogenrhodium (III) porphyrins (eq 4.2). A second method involves the oxidative

addition of cobalt (I)/rhodium (I) porphyrins with corresponding alkyl/aryl group (eq. 4.3; see later).

The preparation of (TPP)Co(n-Bu) complex followed the first preparative method. (TPP)CoCl readily reacts with a mild alkylating reagent, tetrabutyltin, to form the (TPP)Co(n-Bu) complex in 98% yield (eq. 4.2).
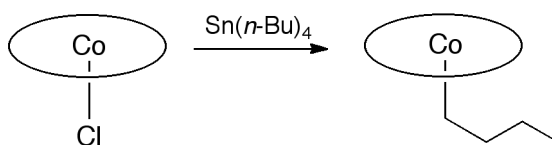
(4.2)

Organocobalt porphyrins are generally light sensitive,[19] thus, the preparation and subsequent crystallization of (TPP)Co(n-Bu) were carried out in the dark. It is not surprising that when a CH$_2$Cl$_2$ solution of (TPP)Co(n-Bu) was studied by UV-vis spectroscopy under normal laboratory lighting, I observed a slow conversion of (TPP)Co(n-Bu) (λ_{max} = 409 nm) to an unidentified (TPP)Co^{III} complex (λ_{max} = 438 nm) (Figure 4.2). Fortunately, crystals of (TPP)Co(n-Bu) were stable in air in the dark for several weeks, as determined by UV-vis spectroscopy.
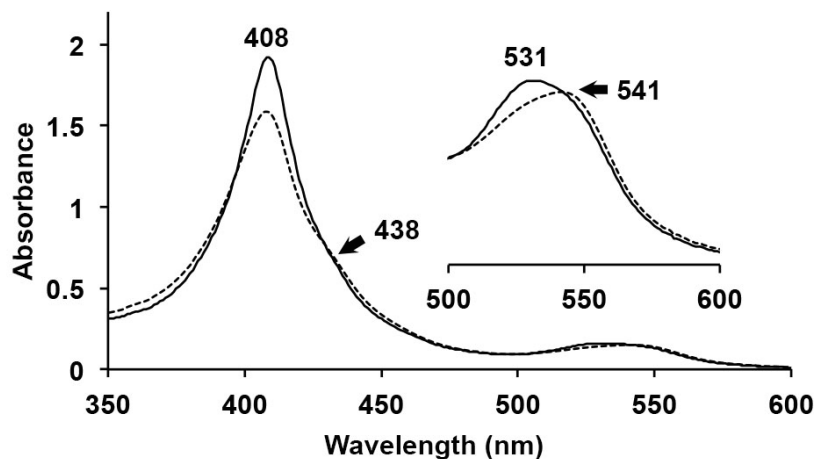
Figure 4.2. UV-vis spectra of the decomposition of (TPP)Co(*n*-Bu) in air. *Solid line:* spectrum of (TPP)Co(*n*-Bu) in CH$_2$Cl$_2$. *Dashed line*: after ~3 hrs in air under normal room lighting.

Crystals of the five-coordinate (TPP)Co(*n*-Bu) formed from a solution of CH$_2$Cl$_2$/hexane, and the structure was solved by X-ray crystallography (Figure 4.3). The X-ray structure of (TPP)Co(*n*-Bu) was unknown prior to my work in this area. The crystal structure displayed a Co-C distance of 2.018(3) Å, which is slightly longer than the corresponding Co-C bond (1.988 (2) Å) in (OEP)Co(Et).[20] The elongation of Co-C bond with increased bulky alky group was also observed in six-coordinate cobaloxime complexes.[21] The C$_\beta$-C$_\gamma$ distance is 1.512(4) Å while the C$_\alpha$-C$_\beta$ distance of the butyl group in this structure is 1.480(4) Å, which indicates an increase of s character of the CH$_2$ orbital. The short C$_\alpha$-C$_\beta$ distance, along with a Co-H$_\beta$-C$_\beta$ angle of 74.4°, is indicative of an agnostic interaction between H$_\beta$-C$_\beta$-Co. Furthermore, an interporphyrin distance of 3.81 Å was observed between the adjacent 24-atom porphyrin planes.
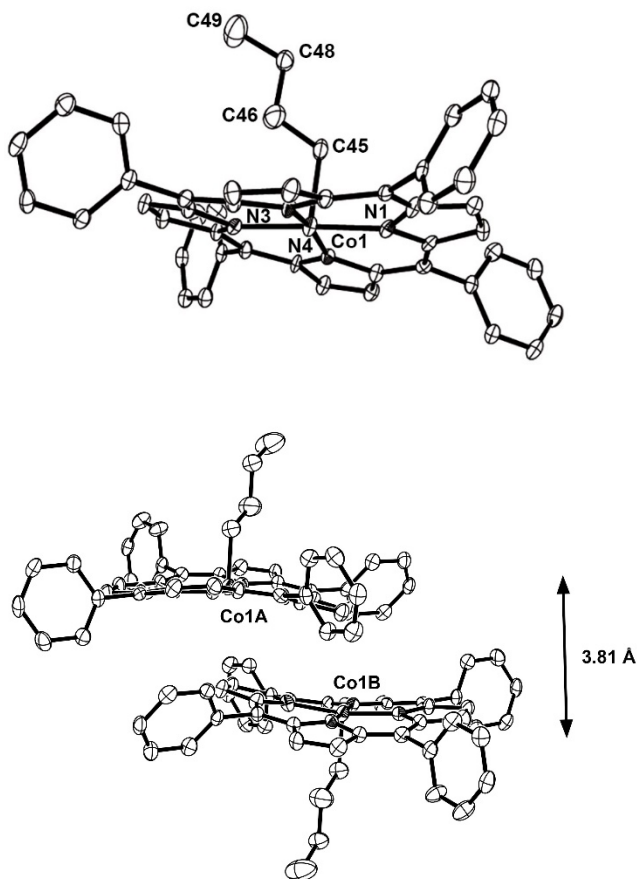
116

Figure 4.3. (*Top*) Molecular structure of (TPP)Co(*n*-Bu). Hydrogen atoms have been omitted for clarity. (*Bottom*) A distance of 3.81 Å was observed between adjacent 24-atom porphyrin planes.

The (TPP)Rh(Ph) complex was prepared by a reagent-induced oxidative addition of $Rh_2(CO_4)TPP$. The Rh(I) porphyrin ($Rh_2(CO_4)TPP$) undergoes an oxidative addition at 80 °C in benzene, and in the presence of trace air (O_2), to form a d^6 (TPP)Rh(III)Ph complex (eq. 4.3, *right*). Work-up of the product resulted in its isolation in ~45% yield. The crystals of five-coordinate (TPP)Rh(Ph) and six-coordinate (TPP)Rh(Ph)(MeOH) complexes were obtained from the slow evaporation of a solution of CH_2Cl_2/hexane or CH_2Cl_2/methanol, respectively.

(4.3)
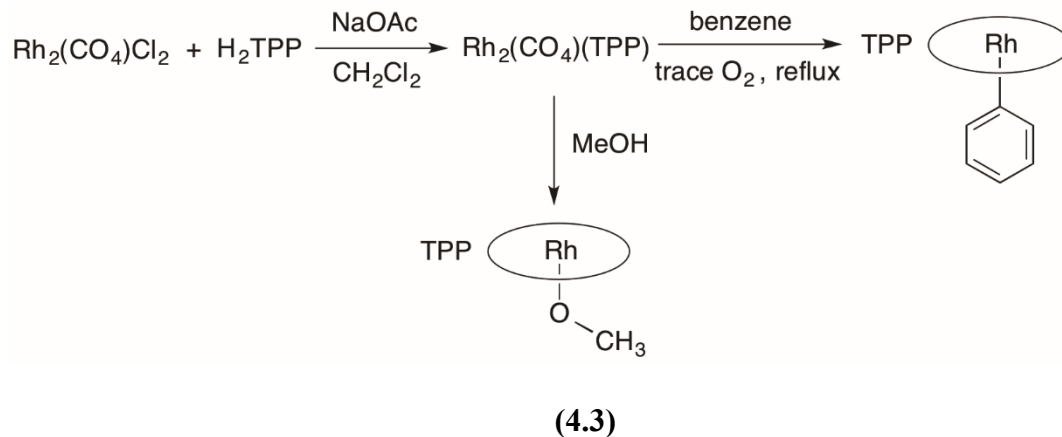
There are two unique molecules in the unit cell of the six-coordinate

(TPP)Rh(Ph)(MeOH) structure. Figure 4.4 (*top*) shows the structure of molecule A. The

Rh-C distances are 1.926(15) and 1.916(11) Å for molecules A and B, respectively.
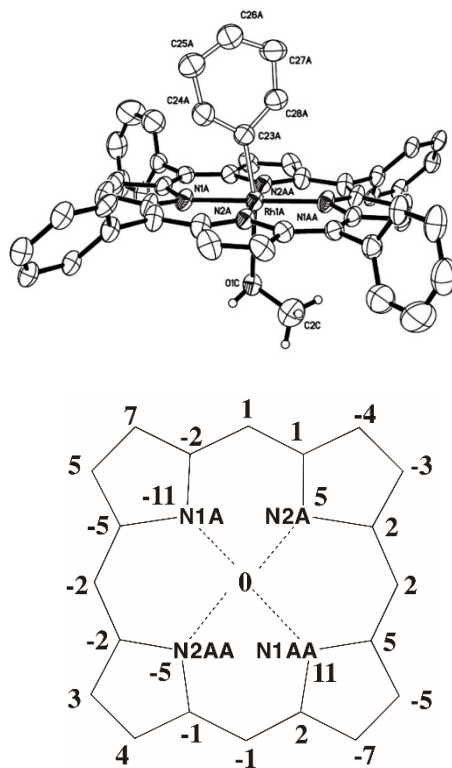

Figure 4.4. (*Top*) Molecular structure of (TPP)Rh(Ph)(MeOH) (molecule A). Hydrogen atoms have been omitted for clarity except those on MeOH. (*Bottom*) Perpendicular atom displacements (in units of 0.01 Å) of the porphyrin core atoms from the 24-atom mean porphyrin plane.

We also obtained crystals of the five-coordinate (TPP)Rh(Ph) (Figure 4.5, *top*). The Rh-C bond lengths are 2.000(5) and 1.993(5) Å, which are about 0.05 Å longer than in the six-coordinate molecule with axial methanol. In this structure, there are two close contacts between porphyrin N atoms and the phenyl groups of an adjacent molecule (Figure 4.5, *bottom*).
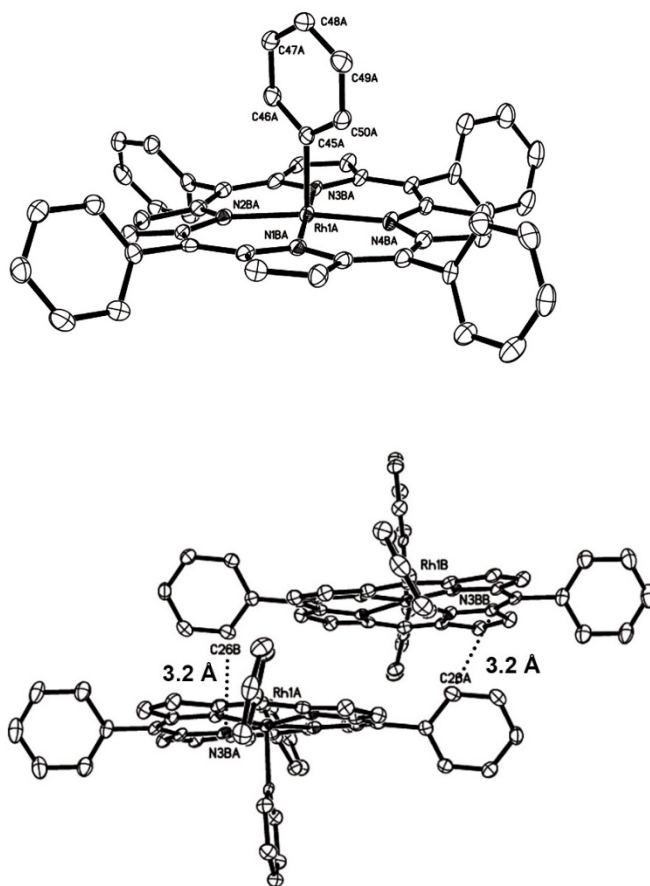

Figure 4.5. (*Top*) Molecular structure of (TPP)Rh(Ph). Hydrogen atoms have been omitted for clarity. (*Bottom*) A depiction of the close contacts between adjacent molecules.

The presence of air (O_2), which was introduced into the benzene solution of $Rh_2(CO)_4TPP$ through a needle on the septum of the schlenk tube, is crucial for the

synthesis of (TPP)Rh(Ph). In one of our experiments, when the benzene solution was completely anaerobic, the reaction resulted in a mixture of unreacted $Rh_2(CO)_4TPP$ and the (TPP)Rh(Ph) complex, evidenced by the starting material's $v_{C=O}$ (2056, 1995 cm^{-1})[17] in the IR spectrum after chromatography in air. Subsequent crystallization of this product mixture from a solution of CH_2Cl_2/methanol in a glove box generated crystals containing two different complexes, namely (TPP)Rh(Ph)(MeOH) and (TPP)Rh(OMe)(MeOH) (bottom of eq. 4.3). This is the first report of a (por)Rh(OMe) structure (Figure 4.6).
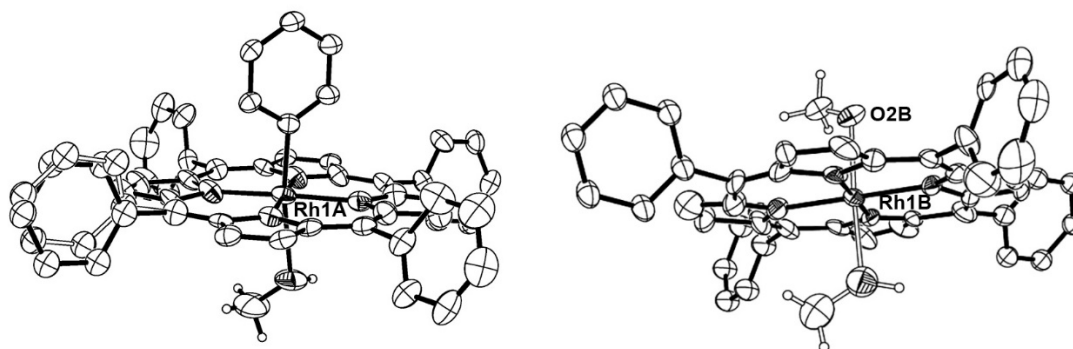

Figure 4.6. Molecular structures of (TPP)Rh(Ph)(CH$_3$OH) (*left*; 82% occupancy) and (TPP)Rh(CH$_3$O)(CH$_3$OH) (*right*; 18% occupancy) in the same crystal. Hydrogen atoms have been omitted for clarity except these on the OMe and MeOH group.

Throughout the whole preparation, methanol was involved only in the crystallization step as a solvent, thus, it is likely that the (TPP)Rh(OMe) was formed through the reaction of unreacted $Rh_2(CO_4)TPP$ with methanol during the process of crystallization. (eq. 4.1, *bottom*). The ^{1}H NMR spectrum of this crystal in CDCl$_3$ displayed a signal at -5.72 ppm, which was assigned to the methoxy ligand.

Curiously, we ordered "(TPP)Rh" and "(OEP)RhCl" from a reputable chemical supplier. I had extreme difficulty over several months characterizing several derivatives

that I generated using these purchased materials. I then re-characterized these commercial samples and found them to be, surprisingly, $(TPP)Rh(C_6H_4Cl)$ and $(OEP)Rh(CH_2Cl)$, instead of what we initially ordered.

Crystals of $(TPP)Rh(C_6H_4Cl)(MeOH)$ were obtained from a solution of the compound in $CH_2Cl_2/MeOH$, and its structure was determined by X-ray crystallography (Figure 4.7). The occupancies of the disordered Cl atoms at the *para* and *meta* positions of the ligand were refined to be 0.872(3) and 0.128(3), respectively, which are consistent with the result from an ^1H NMR spectroscopy study of the complex.

Crystals of the five-coordinate $(OEP)Rh(CH_2Cl)$ formed from a solution of the compound in $CH_2Cl_2/MeOH/hexane$. The crystal structure (Figure 4.8) displayed a Rh-C distance of 2.015(7) Å, which is similar to the Rh-C distance of 2.010(4) Å in the related $(TPP)Rh(CH_2Cl)$ structure published by Collman.[22] However, in the structure of $(TPP)Rh(CH_2Cl)$, the β carbon atoms on the porphyrin displayed a large distortion with a maximum displacement of 0.484 Å to the 24-atom mean porphyrin plane. The closest Rh-Rh distance and the interporphyrin separation in $(TPP)Rh(CH_2Cl)$ are 5.32 and 3.67 Å, respectively. In our structure of $(OEP)Rh(CH_2Cl)$, the porphyrin is more "flat" (Figure 4.8, *middle*). The two distances above mentioned are shortened by 0.7 and 0.4 Å, respectively. An interporphyrin separation distance of 3.32 Å indicates a strong porphyrin π-π stacking (Figure 4.8, *bottom*) between the adjacent porphyrins in the structure of $(OEP)Rh(CH_2Cl)$.
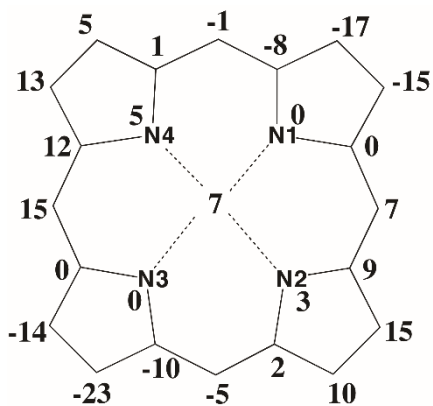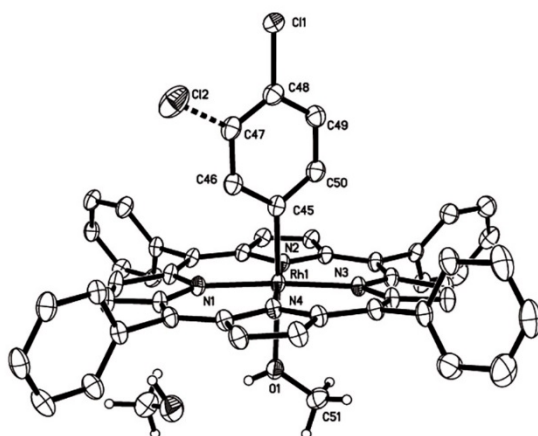
Figure 4.7. (*Top*) Molecular structure of (TPP)Rh(C₆H₄Cl)(MeOH). Hydrogen atoms have been omitted for clarity except those on MeOH. The Cl atom was disordered at two positions. (*Bottom*) Perpendicular atom displacements (in units of 0.01 Å) of the porphyrin core atoms from the 24-atom mean porphyrin plane.
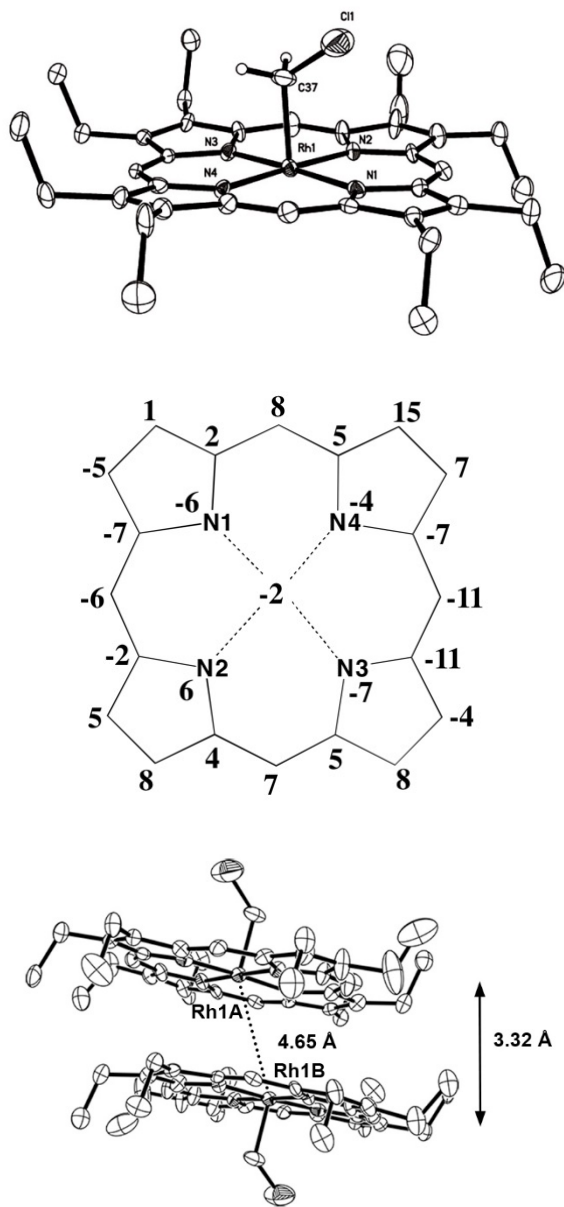
Figure 4.8. (*Top*) Molecular structure of (TPP)Rh(CH$_2$Cl). Hydrogen atoms have been omitted for clarity except those on the CH$_2$Cl group. (*Middle*) Perpendicular atom displacements (in units of 0.01 Å) of the porphyrin core atoms from the 24-atom mean porphyrin plane. (*Bottom*) A diagram showing the distance of 3.32 Å between adjacent porphyrin macrocycles.

The UV-vis and ^{1}H NMR spectral data of the cobalt and rhodium porphyrins described in this chapter are listed in Table 4.1 and Figure 4.9, respectively. These data are consistent with the literature values.

Table 4.1. Selected UV-vis spectral data of synthesized and characterized Rh(III)/Co(III) porphyrins in CH_2Cl_2.

Compound	Peak position, λ (nm) (This work)	Peak position, λ (nm) (Ref)
(TPP)RhCl	422, 533, 568	
(TPP)Rh(C_6H_4Cl)	413, 521, 634	
(TPP)Rh(C_6H_5)	412, 520, 548	413, 520, 548[17]
(OEP)Rh(CH_2Cl)	394, 511, 543	
(TPP)Co(n-Bu)	408, 531	409, 531[16]

The ^{1}H NMR spectra displayed peaks, as expected, due to the porphyrin macrocycle and the axial ligands in these diamagnetic complexes. The ^{1}H signals of the ligands coordinated to the metals are upfield from the normal region of the uncoordinated ligand, which results from the ring current effect of the aromatic porphyrin macrocycles.[23] The ring current effect decreases with distance. As expected, the signal of H4 of the butyl group of (TPP)Co(n-Bu) shifted less than the H3. However, it is interesting to note that the H2 of (TPP)Co(n-Bu) resonates at higher field than the H1. This observation is consistent with the NMR spectra of other previously reported five-coordinate alkyl cobalt porphyrin complexes. It is likely resulted from the agnostic interaction between C2-H2-Co.

Also, the ^{1}H NMR spectrum of (TPP)Rh(Ph) displayed *pyr-H* signal at a chemical shift of 8.68 ppm. In comparison, the *pyr-H* was observed at a higher chemical shift at 8.75 ppm for (TPP)Rh(p-C_6H_4Cl), which parallels the better electron donating ability of the phenyl ligand. The aryl ligand, as a σ-donor, enhances the Rh to porphyrin

124

π-bonding and results in the increasing shielding of the porphyrin protons. The better electron donating ability of the axial ligand will lead to an increased shielding of the porphyrin. This *cis*-effect was previously observed for the alkylmetalloporphyrins with metals in d^6 configuration.[24] Furthermore, although not shown in Scheme 4.1, the ^{1}H NMR spectrum of (TPP)Rh(C$_6$H$_4$Cl) indicated that it is a mixture of two isomers, (TPP)Rh(*p*-C$_6$H$_4$Cl) (β-pyr, 8.75 ppm) and (TPP)Rh(*m*-C$_6$H$_4$Cl) (β-pyr, 8.76 ppm),[17] and (TPP)Rh(*p*- C$_6$H$_4$Cl) was the major component in this mixture, which is consistent with the results from X-ray crystallography studies.

1

TPP signals

8.68 (s, β-H)
8.09 (d, *o*-H of phenyl)
7.67 (m, *p*,*m*-H of phenyl)

2

TPP signals

8.75 (s, β-H)
8.12 (d, *o*-H of phenyl)
7.72 (m, *p*,*m*-H of phenyl)

3

TPP signals

8.75 (s, β-H)
8.10 (d, *o*-H of phenyl)
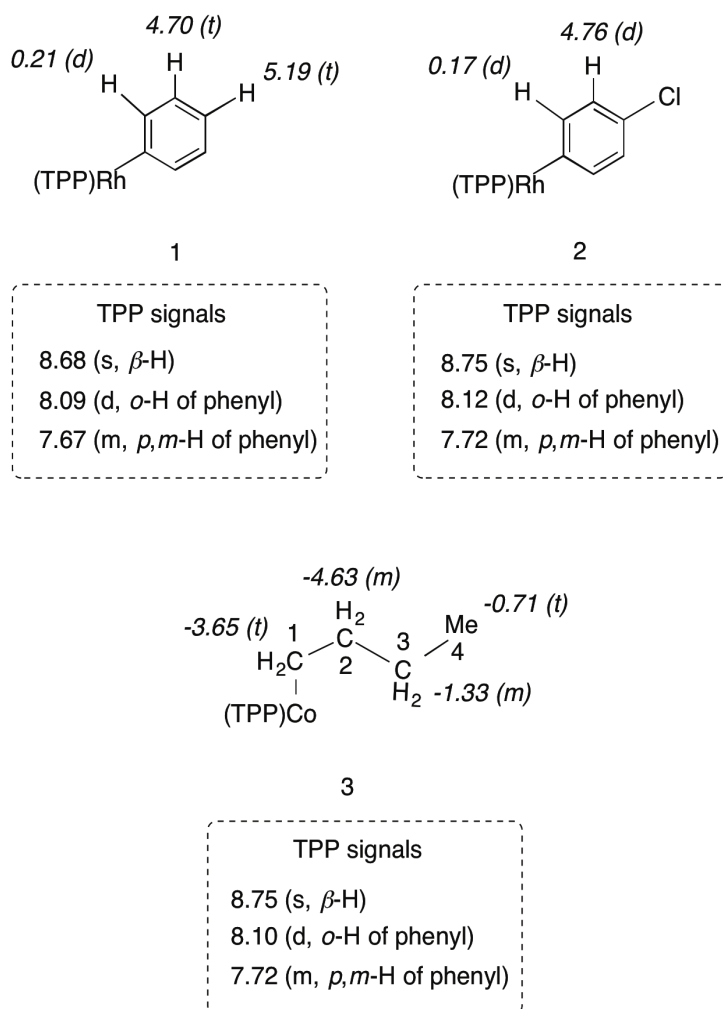7.72 (m, *p*,*m*-H of phenyl)

Figure 4.9. ^{1}H NMR spectral data of selected rhodium/cobalt porphyrins in CDCl$_3$.

4.3.2 The reaction of (TPP)Rh(R) with NO in solution

The reactivity of NO gas with the σ-bonded aryl rhodium porphyrins, (TPP)Rh(C$_6$H$_4$Cl) and (TPP)Rh(Ph), was studied by infrared spectroscopy in CH$_2$Cl$_2$, as described in the experimental section. Addition of NO to (TPP)Rh(Ph) changes the color of the solution from bright orange to dark red over a period of 25 min. Excess NO was then removed by displacement of the headspace with N$_2$. The product was quickly transferred by an air-tight syringe to a glass vial equipped with a mid-IR fiber-optic dip probe. The IR spectrum of the product solution displayed two new peaks at 1758 and 1712 cm^{-1}, along with a shoulder at 1637 cm^{-1} (Figure 4.10). The multiple new peaks in the solution IR spectrum were indicative of perhaps a not-so-straightforward reaction product. The shoulder at 1637 cm^{-1} is close to the reported v_{NO} of a putative (TPP)Rh(NO) at 1630 cm^{-1}.[11]
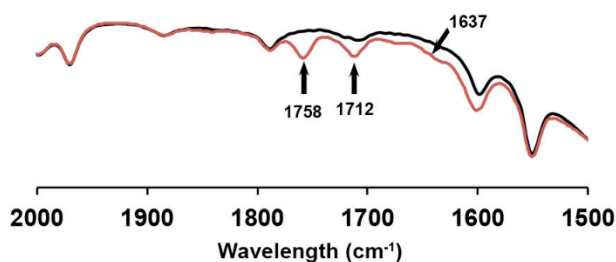

Figure 4.10. The IR spectra (CH$_2$Cl$_2$) showing the formation of new peaks at 1758, 1712 and 1637(sh) cm^{-1} when (TPP)Rh(Ph) was reacted with NO in solution.

Crystallization of this product from the slow evaporation of a CH$_2$Cl$_2$/hexane solution of the product in a glove box resulted in the formation of violet block shaped crystals over a period of two days. The X-ray crystallography was used to characterize the product which turned out to be a mixture of (TPP)Rh(Ph) (starting material) and the

bis-β-nitrated $((NO_2)_2TPP)Rh(Ph)$ complexes. The formation of $((NO_2)_2TPP)Rh(Ph)$ was completely unexpected, and may result from the attack of an in-situ generated NO_x species on the porphyrin. The formation of the nitro groups was also indicative in the IR(KBr) spectrum of the crystals, judged by the increase of peak intensity at 1262 cm^{-1}.[11]

The structure of $((NO_2)_2TPP)Rh(Ph)$ is shown in Figure 4.11. It is not surprising that the porphyrin macrocycle displays a large "saddled" distortion[25] after the nitration of the porphyrin at the β positions (Figure 4.11, *middle*), with a largest displacement of 0.52 Å from the 24-atom mean porphyrin plane being that of a non-nitrated pyrrole C-atom. Interestingly, we observed an unusual short distance between the Rh and the *pyrrole*-Cs on an adjacent porphyrin (Figure 4.11, *bottom*), which may lead to or result from the large distortion of the porphyrin macrocyle. The C=C double bonds are located in the "axial" position of the metal, indicating a possible but weak C=C π-interaction with the metal center.

A similar reaction of $(TPP)Rh(C_6H_4Cl)$ with NO gas in CH_2Cl_2 also resulted in the formation of IR bands at 1758 and 1712 cm^{-1}, but all attempts to grow crystals from this reaction solution were unsuccessful.
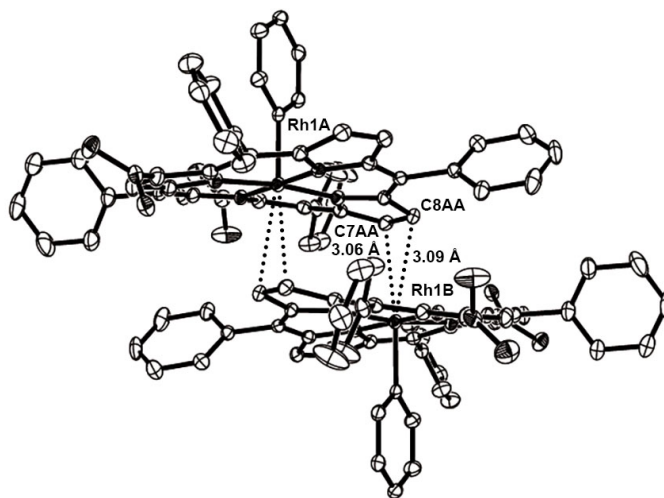
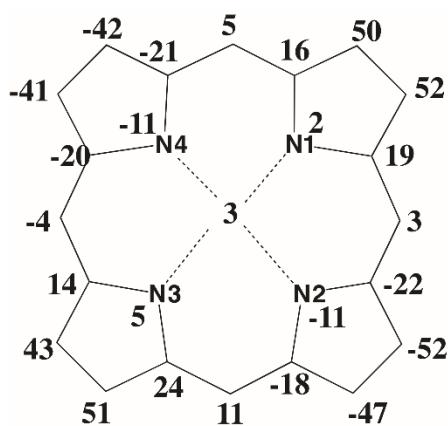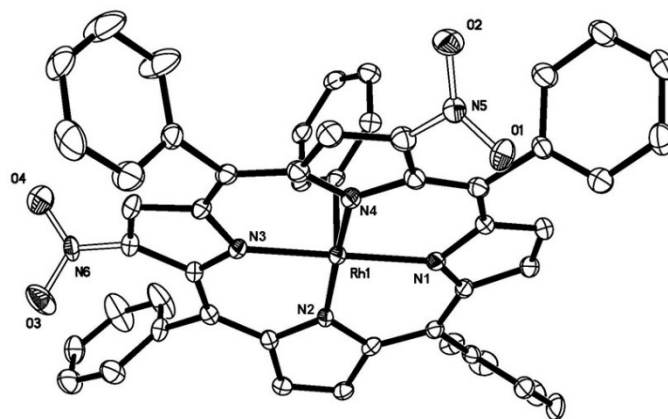**Figure 4.11.** (*Top*) Molecular structure of ((NO₂)₂TPP)Rh(Ph). Hydrogen atoms have been omitted for clarity. (*Middle*) Perpendicular atom displacements (in units of 0.01 Å) of the porphyrin core atoms from the 24-atom mean porphyrin plane. (*Bottom*) The short distance between the Rh and the *pyrrole*-Cs on an adjacent porphyrin.

4.3.3 The reactions with NO gas in crystals: a solid-gas method

Soaking crystals of metallooporphyrins in an atmosphere of NO gas could allow

NO to diffuse into the crystals and coordinate with the metal centers of the porphyrins,

if the space between porphyrin molecules is large enough to allow unhindered NO

diffusion. This method has been successfully utilized by a former group member (Dr.

Nan Xu), to obtain the first structures of previously inaccessible (por)Fe(NO)(thiolate)[4]

and (por)Fe(NO)(O-ligand) complexes.[3] The solid-gas method is especially useful to

prepare nitrosyl metal porphyrin derivatives that are unstable in solution precluding

crystallization from solution. The reactions of NO with (por)Rh(R) in solution discussed

previously is complicated, and resulted in the isolation of the unexpected nitrated

porphyrin as the product. Thus, the solid-gas method was attempted here to obtain the

(por)Rh(NO)X products.

Soaking crystals of the five-coordinate Rh/Co porphyrins ((TPP)Co(n-Bu),

(TPP)Rh(Ph), (OEP)Rh(CH$_2$Cl)) with NO gas did not result in the formation of the

nitrosyl metal derivatives. As discussed earlier, the five-coordinate Rh/Co porphyrin

complexes are usually packed tightly in crystals with short intermolecular distances

(Figures 4.3, 4.5, 4.8), which probably disfavor an incoming sixth (NO) ligand.

However, soaking crystals of (TPP)Co(n-Bu) with NO for two weeks resulted in

the formation of new IR bands at 1683 and 1634 cm^{-1} along with an increase of peak

intensity at 1462 cm^{-1}. The peak at 1683 cm^{-1} is indicative of the formation of the

known (TPP)CoNO,[10] accompanied by the dissociation of butyl group. The peaks at

1634 and 1462 cm^{-1} indicate the formation of a derivative that has not yet been

identified.

In contrast, the use of the six-coordinate (por)Rh(X)(solvent) precursors in these NO-soaking experiments allowed for the formation of the desired (por)Rh(NO)X derivatives. (TPP)Rh(Cl)(MeOH) was used to obtain (TPP)Rh(NO)Cl, and (TPP)Rh(Ph)(MeOH) was used to obtain (TPP)Rh(NO)(Ph). The structures of (TPP)Rh(NO)(Cl) and (TPP)Rh(NO)(Ph) are shown in Figure 4.12 and Figure 4.13. Selected bond lengths (Å) and bond angles (°) for the precursor Rh(III) porphyrins and their NO adducts are listed in Table 4.2.

Table 4.2. Selected bond lengths (Å) and bond angles (°) in the structures of precursor Rh(III) porphyrins and their NO derivatives.

	Rh-N(por)	Rh-X(axial)	Rh-N(O)	Rh-N-O	ΔRh^*
(TPP)Rh(Cl)(CH$_3$OH)	2.031 (6)	2.305 (19)			4
(TPP)Rh(Ph)	2.022 (4)	2.000 (5)			11
		1.993 (5)			
(TPP)Rh(Ph)(CH$_3$OH)	2.037 (6)	1.926 (15)			0
	2.037 (6)	1.916 (11)			
(TPP)Rh(C$_6$H$_4$Cl)(CH$_3$OH)		1.997 (4)			7
(TPP)Rh(NO)(Cl)	2.038 (9)	2.263 (3)	2.202 (11)	123.6 (16)	1
				123.9 (14)	
(TPP)Rh(NO)(Ph)	2.031 (6)	1.962 (16)	2.310 (13)	106.1 (17)	0
	2.029 (6)	2.114 (18)	2.308 (12)	115.2 (14)	
(TPP)Rh(N(=O)C$_6$H$_4$Cl)	2.039 (10)		1.976 (12)	120.0 (11)	8

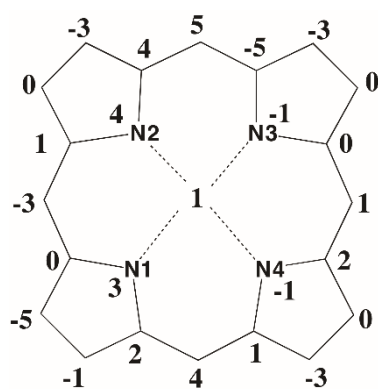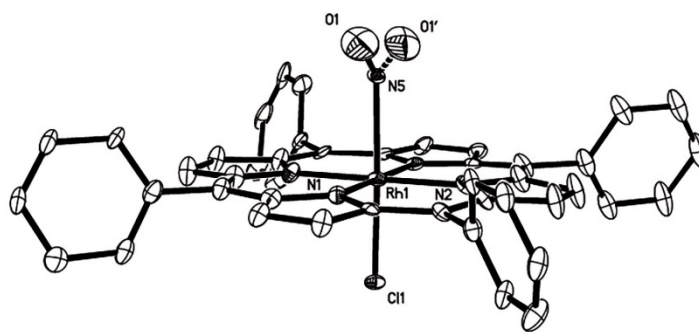* The displacement of Rh towards aryl/chloro ligand.

Figure 4.12. (*Top*) Molecular structure of (TPP)Rh(NO)Cl. Hydrogen atoms have been omitted for clarity. The oxygen atom was disordered over two positions. (*Bottom*) Perpendicular atom displacements (in units of 0.01 Å) of the porphyrin core atoms from the 24-atom mean porphyrin plane.
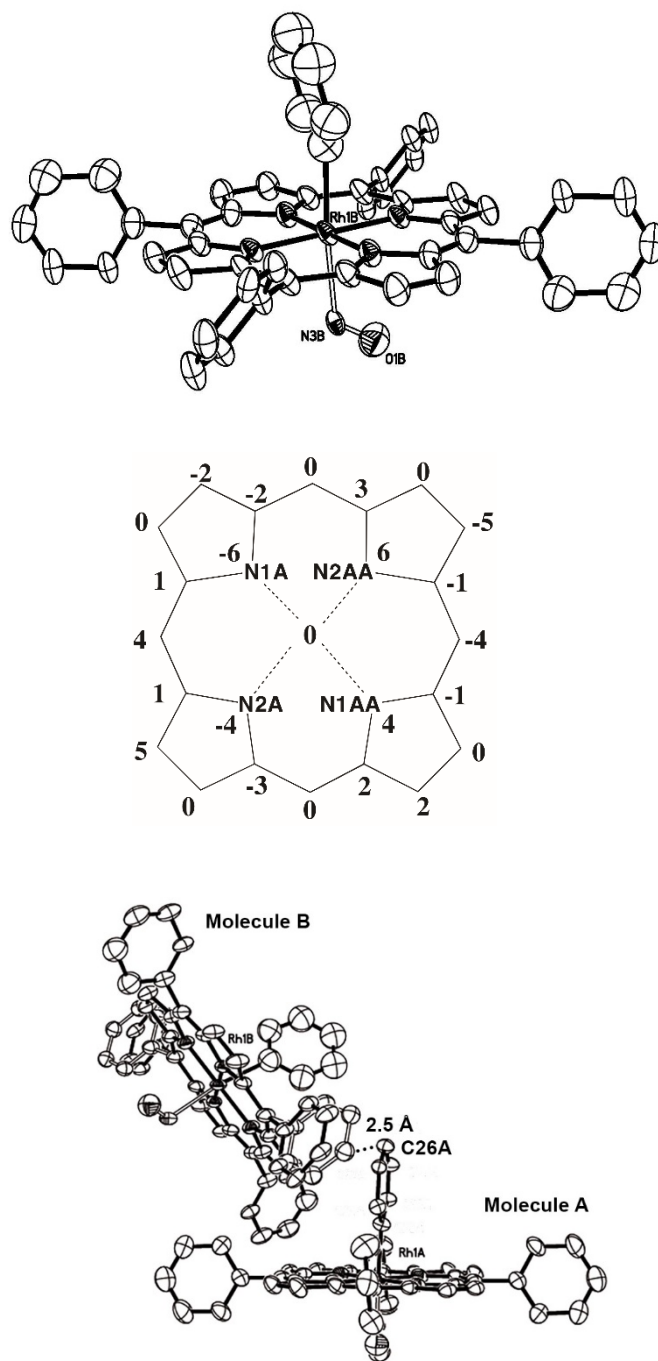
Figure 4.13. (*Top*) Molecular structure of molecule B in (TPP)Rh(NO)(Ph). Hydrogen atoms have been omitted for clarity. (*Middle*) Perpendicular atom displacements (in units of 0.01 Å) of the porphyrin core atoms from the 24-atom mean porphyrin plane. (*Bottom*) Relative orientation of molecules A and B in the unit cell.

132

There are two unique molecules in the unit cell of (TPP)Rh(NO)(Ph), namely molecule A and molecule B (Figure 4.13, *bottom).* The Rh-C distances and the bond angles of Rh-N-O are slightly different for these two molecules (Table 4.2). A short intermolecular distance of 2.5 Å was observed between the C26A atom on the phenyl ligand of molecule A and the C atom on the phenyl group on the *meso*-pyrrole position of molecule B (Figure 4.13, *bottom*). This close distance between two phenyl groups likely led to the disorder of these *meso*-phenyl groups of molecule B. It could also affect the orientation of the phenyl ligand on molecule A to result in the differences in Rh-C distances in these two molecules.

Several interesting features of these two six-coordinate nitrosyl rhodium porphyrin complexes are worthy of note. First, upon NO bonding, the previously saddled porphyrin macrocyle of (TPP)Rh(Cl)(MeOH) changed to a near-planar conformation (Figures 4.1 and 4.12). Changing to a more flat porphyrin macrocycle with NO binding was also observed in the crystal structure of (TPP)Rh(NO)(Ph) (Figures 4.4 and 4.13). Second, the Rh-N(O) distances in the structures of (TPP)Rh(NO)(Cl) and (TPP)Rh(NO)(Ph) were refined to be 2.202(11) and 2.310(13) Å, respectively. These bond lengths are rather long and suggest that the NO molecules are only weakly coordinated to the metal centers. More importantly, this experimental result is consistent with other DFT calculations from our group (not shown).

Also, the RhNO moiety in (TPP)Rh(NO)Cl is bent with an angle of 123.6(16)$^\text{o}$, while the RhNO moiety in (TPP)Rh(Ph)(NO) is bent with an angle of 106.1$^\text{o}$(17) and 115$^\text{o}$(14) for molecules A and B, respectively (Scheme 4.1). These values are also unexpected. In the structure of five-coordinate nitrosyl iron (II) porphyrin, the Fe-N-O

displayed an angle of approximately 140 °. In general, (por)M(NO)X porphyrins that are formally {MNO}[7] expected to have M-N-O angle of ~140°.[26] In my structures, these angles are significantly decreased by ~20 ° (Scheme 4.2). It could be a result from the very weak Rh-N(O) bonds that place these compounds as "exceptions" to the normal cases.
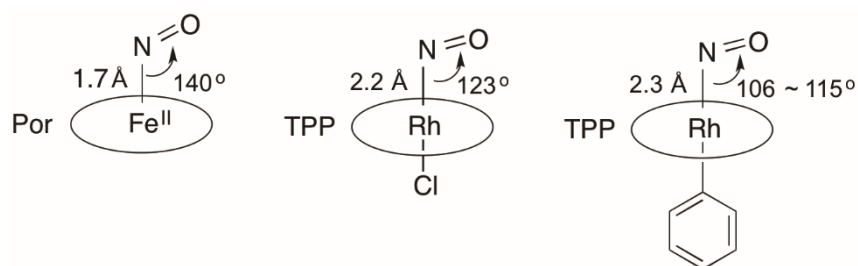
Scheme 4.1. The bond distances and angles of some formally {MNO}[7] nitrosyl metal porphyrins.

In the work of our previous group member (Dr. Nan Xu), the solid-state structure of six-coordinate (OEP)Fe(NO)(S-2,6-(CF$_3$CONH)$_2$C$_6$H$_3$] compound displays an unusual bent Fe-N-O linkage (159.6°),[4] while the (TPP)Fe(NO)(OCOCF$_3$) compound displays an expected near liner conformation of the Fe-N-O moiety,[3] as shown on the left side of Scheme 4.2. A following DFT calculation by Lehnert revealed that the differences in bond angles are due to the differences in σ-trans effects of the coordinated ligands. In our work, a similar trend was also observed. The Rh-N-O moiety in (TPP)Rh(NO)(Ph) is more bent than the one in (TPP)Rh(NO)(Cl).
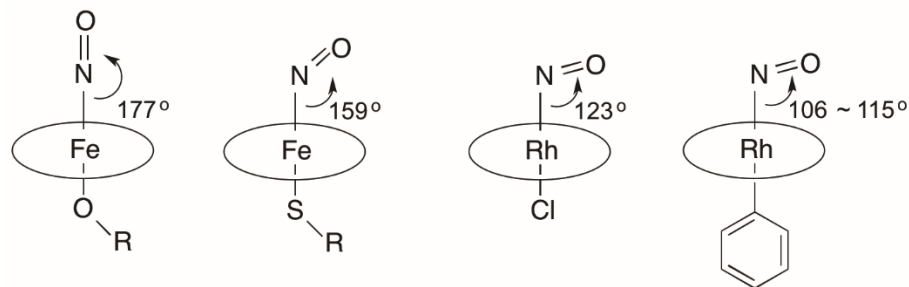
Scheme 4.2. The nitrosyl metal porphyrins with different ligands showing different bonding angles.

The weak Rh-N(O) bond and the ease of oxidation of (por)Rh(NO)(R) in air resulted in difficulties in obtaining reliable IR spectra of the complexes.[11] The IR spectrum (KBr) of crystals of (TPP)Rh(NO)(Cl) displayed the formation of weak peaks at 1731, 1397 and 1261 cm^{-1}, along with the significant increase of peak at 1538 cm^{-1}. The formation of new peaks in the range from 1500 to 1200 cm^{-1} indicate oxidation of the bound NO to nitrite in the presence of trace air (O_2) when recording the IR spectrum.[27] The same phenomenon was also observed for the IR spectrum of (TPP)Rh(NO)(Ph) where I observed the formation of new peaks at 1811, 1397 and 1321 cm^{-1} and an increase of peak intensity at 1595 cm^{-1}.

To my surprise, exposing crystals of (TPP)Rh(C_6H_4Cl) to NO gas for two weeks led to a completely unexpected result. The structure of the product was determined, by X-ray crystallography, to be a mixture of (TPP)Rh(N(=O)C_6H_4Cl) and (TPP)Rh(C_6H_4Cl)(CH_2Cl_2) (Figure 4.14). Instead of binding to the metal center at the *trans* position as observed in the structures described above, NO had selectively inserted in the metal-carbon bonds of some of the molecules in the crystal to result in the formation of a *C*-nitroso rhodium porhyrin complex, with an N=O distance of 1.223(15) Å.
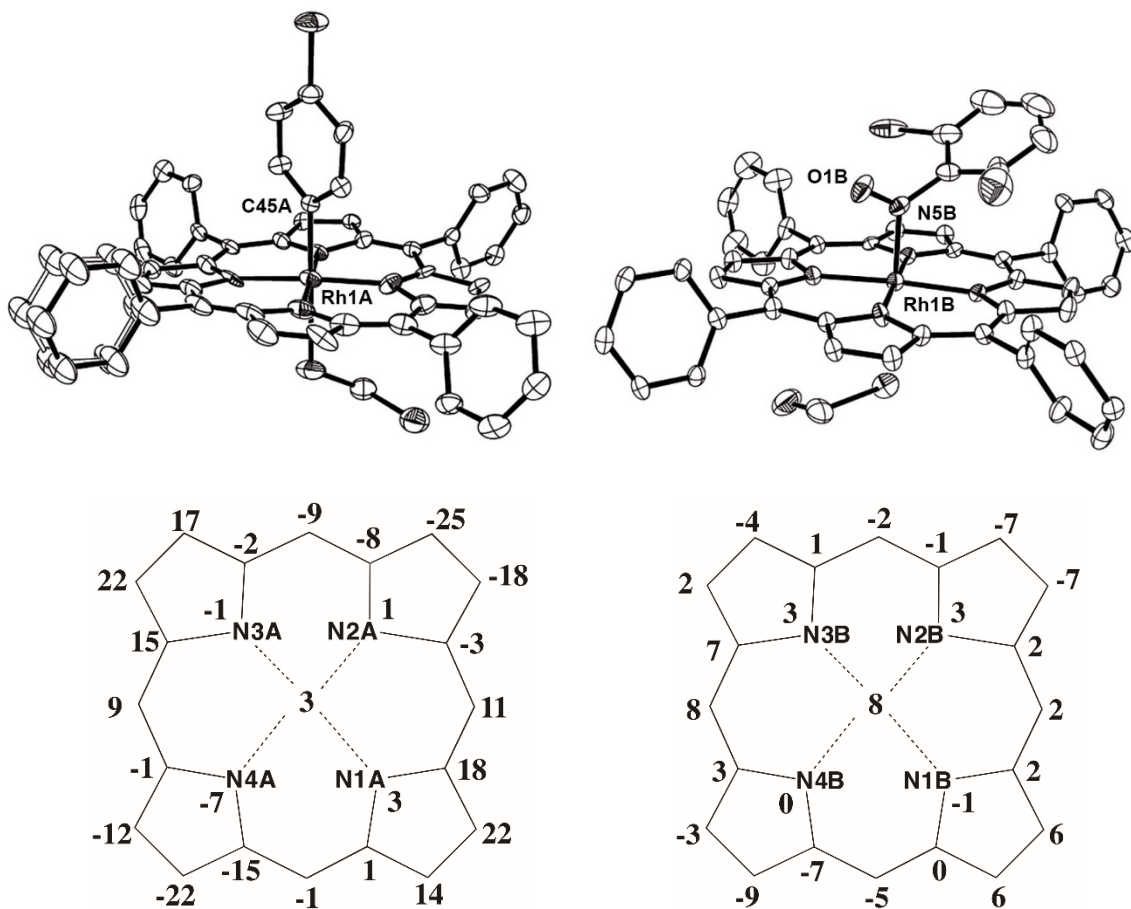
Figure 4.14. (*Top*) Molecular structures of (TPP)Rh(C_6H_4Cl)(CH_2Cl_2) (*left*) and (TPP)Rh(N(=O)C_6H_4Cl) (*right*) in the same crystal. Hydrogen atoms have been omitted for clarity. (*Bottom*) Perpendicular atom displacements (in units of 0.01 Å) of the porphyrin core atoms from the 24-atom mean porphyrin plane of (TPP)Rh(C_6H_4Cl)(CH_2Cl_2) (*left*) and (TPP)Rh(N(=O)C_6H_4Cl) (*right*).

Curiously, the chloro substituent on the aryl ring of the axial ligand had (formally) migrated to the *ortho* position in the *C*-nitroso product (Figure 4.14, right). This migration of Cl atom may play an important role in the NO insertion. However, it is important to note that the crystals we used to obtain the structure of the precursor compound ((TPP)Rh(C_6H_4Cl)(MeOH)) and the crystals used for NO soaking *are not from the same batch of crystals*. Although those two batches of crystals were

crystallized under the same conditions, we are hesitant to compare their structures and over-interpret the structural differences.

The IR (KBr) spectrum of the NO-soaked crystals left in the vial displayed the formation of a new peak at 1414 cm^{-1}, which was assigned to the v_{NO} stretching frequency of the *C*-nitroso ligand (Figure 4.15). It is in the same range as the v_{NO} stretching frequencies (1330~1500 cm^{-1}) reported for the other C-nitroso metal porphyrin complexes.[28-30]
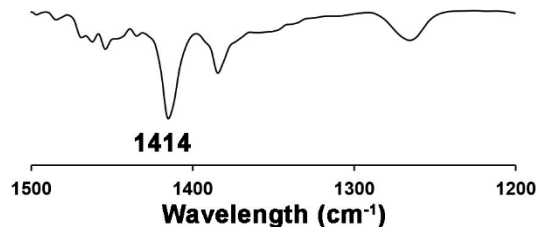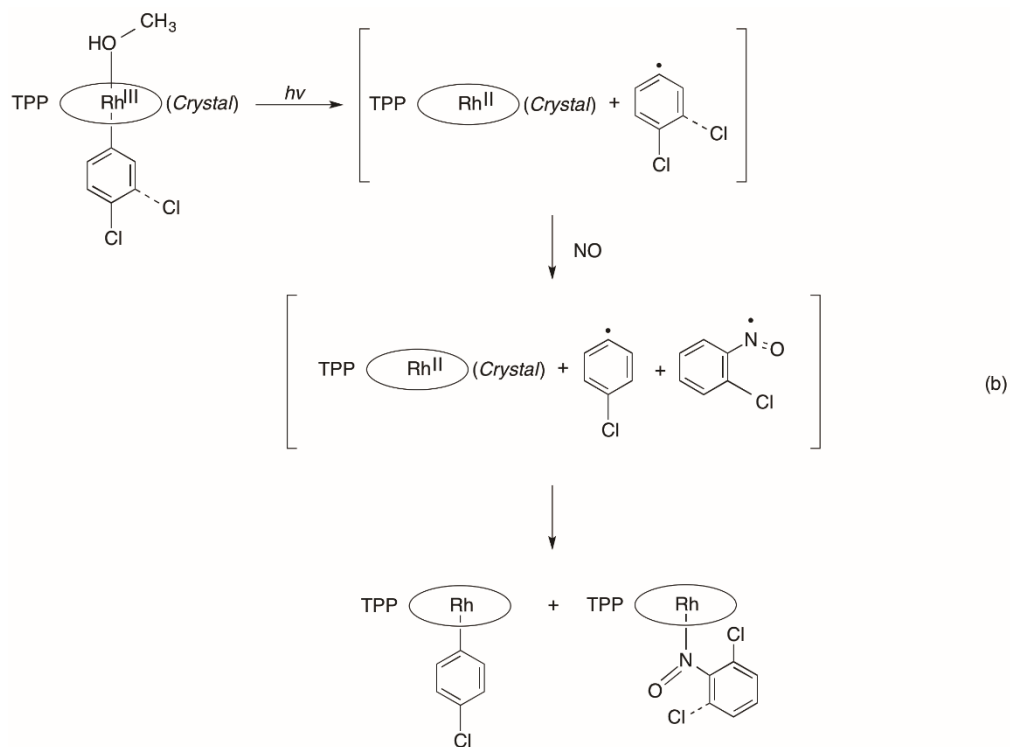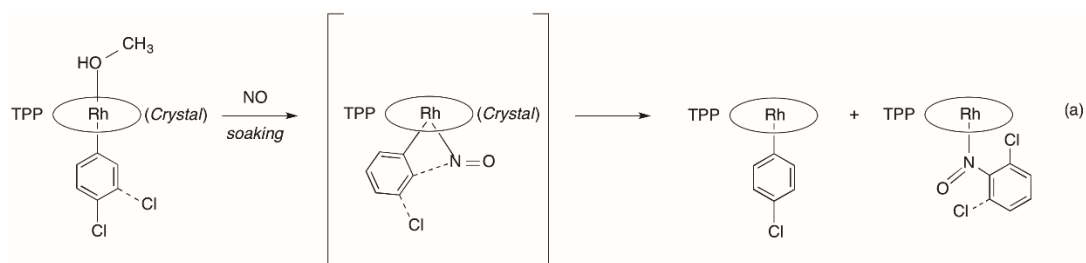

Figure 4.15. The infrared spectrum of the crystal containing (TPP)Rh(NOC$_6$H$_4$Cl) highlighting the formation of a new band at 1414 cm^{-1}.

Our group is still working on the mechanism of this unusual NO insertion. Generally, there are two possible ways for NO insertion into a metal-carbon bond, which are shown in eq. 4.4.

(4.4)

Proposal (a) is a migratory insertion reaction; proposal (b) involves the photo-cleavage of the rhodium-carbon bond, which will consequently generate an organic radical and a porphyrin rhodium (II). Since the reaction is happening in a crystal, due to a sterically unfavorable coordination of a Rh(o-C$_6$H$_4$Cl) species, NO might preferentially attack at the ortho position of the chlorobenzene radical, which results in the formation of C-nitroso compound and the migration of the Cl atom in the final product.

In summary, I managed to prepare and structurally characterize the first set of rhodium nitrosyl porphyrins (TPP)Rh(NO)Cl and (TPP)Rh(NO)Ph using a "solid-gas NO soaking" method in this work.[3,4] X-ray crystallography was used to determine accurate geometries of the Rh-N-O linkage, which were found to deviate significantly from what was predicted in the literature. The unexpected long Rh-N(O) bond lengths of ~2.2 Å could signify weak interactions between NO and these group 9 metalloporphyrins, placing them in a "non-classical" set of (por)M(NO)X systems. In addition, for the reaction between NO and the crystals of (TPP)Rh(C_6H_4Cl), I observed the first reported NO insertion into a metal-carbon bond in a porphyrin system, to result in the formation of a coordinated C-nitroso ligand.

4.4 References

(1)   Marletta, M. A. *J Biol Chem* **1993**, *268*, 12231.

(2)   Bellamy, T. C.; Wood, J.; Garthwaite, J. *Proc Natl Acad Sci U S A* **2002**, *99*, 507.

(3)   Xu, N.; Goodrich, L. E.; Lehnert, N.; Powell, D. R.; Richter-Addo, G. B. *Angew Chem Int Ed Engl* **2013**, *52*, 3896.

(4)   Xu, N.; Powell, D. R.; Richter-Addo, G. B. *Angew Chem Int Ed Engl* **2011**, *50*, 9694.

(5)   Ellison, M. K.; Scheidt, W. R. *J Am Chem Soc* **1997**, *119*, 7404.

(6)   Awasabisah, D.; Xu, N.; Sharmah Gautam, K. P.; Powell, D. R.; Shaw, M. J.; Richter-Addo, G. B. *Dalton Trans* **2013**, *42*, 8537.

(7) Cheng, L.; Chen, L.; Chung, H.-S.; Khan, M. A.; Richter-Addo, G. B.; Young, V. G. *Organometallics* **1998**, *17*, 3853.

(8) Brown, K. L. *Chem Rev* **2005**, *105*, 2075.

(9) Kobayashi, M.; Shimizu, S. *Eur J Biochem* **1999**, *261*, 1.

(10) Richter-Addo, G. B.; Hodge, S. J.; Yi, G.-B.; Khan, M. A.; Ma, T.; Van Caemelbecke, E.; Guo, N.; Kadish, K. M. *Inorg Chem* **1996**, *35*, 6530.

(11) Wayland, B. B.; Newman, A. R. *Inorg Chem* **1981**, *20*, 3093.

(12) Bruker-AXS *Data Collection*: SMART Software Reference Manual **1998**.

(13) Bruker-AXS *Data Reduction*: SMART Software Reference Manual **1998**.

(14) Adler, A. D.; Longo, F. R.; Finarelli, J. D.; Goldmacher, J.; Assour, J.; Korsakoff, L. *J Org Chem* **1967**, *32*, 476.

(15) Datta-Gupta, N. a. B., T. J. *J Pharm Sci* **1968**, *57*, 300.

(16) Fukuzumi, S.; Kitano, T. *Inorg Chem* **1990**, *29*, 2558.

(17) Collman, J. P.; Boulatov, R. *Inorg Chem* **2001**, *40*, 2461.

(18) Zhou, X.; Wang, R.-J.; Xue, F.; Mak, T. C. W.; Chan, K. S. *J Organomet Chem* **1999**, *580*, 22.

(19) Kendrick, M. J.; Al-Akhdar, W. *Inorg Chem* **1987**, *26*, 3971.

(20) Cao, Y.; Petersen, J. L.; Stolzenberg, A. M. *Inorg Chim Acta* **1997**, *263*, 139.

(21) Bresciani-Pahor, N.; Randaccio, L.; Zangrando, E.; Toscano, P. J. *Inorg Chim Acta* **1985**, *96*, 193.

(22)   Collman, J. P.; Boulatov, R. *Inorg Chem* **2001**, *40*, 560.

(23)   Brothers, P. J.; Collman, J. P. *Acc Chem Res* **1986**, *19*, 209.

(24)   Buchler, J.; Kokisch, W.; Smith, P. Cis, Trans, and Metal effects in Transition
         Metal Porphyrins. In *Structure and bonding;* S.Hubert, M.; Hussonnois, R.G.,
         Eds.; Springer Berlin Heidelberg: 1978; Vol. 34 (Novel Aspects), pp. 79-134.

(25)   Scheidt, W. R. Systematics of the Stereochemistry of Porphyrins and
         Metalloporphyrins. In *The Porphyrin Handbook;* Kadish, K.M., Smith, K.M.,
         Guilard, R., Eds.; Academic Press: New York, 2000; Vol. 3 (Inorganic,
         Organometallic, and Coordination Chemistry), pp. 49-112.

(26)   Cheng, L.; Richter-Addo, G. B. Binding and Activation of Nitric Oxide by
         Metalloporphyrins and Heme. In *The Porphyrin Handbook*; Kadish, K.M.,
         Smith, K. M., Guilard, R., Eds.; Academic Press: New York, 2000; Vol.4
         (Biochemistry and Binding: Activation of Small Molecules), pp. 219-291

(27)   Cheng, L.; Powell, D. R.; Khan, M. A.; Richter-Addo, G. B. *Chem Commun*
         2000, 2301.

(28)   Sohl, C. D.; Lee, J. Y.; Alguindigue, S. S.; Khan, M. A.; Richter-Addo, G. B. *J
         Inorg Biochem* **2004**, *98*, 1238.

(29)   Wang, L.-S.; Chen, L.; Khan, M. A.; Richter-Addo, G. B. *Chem Commun* **1996**,
         323.

(30)   Lee, J.; Twamley, B.; Richter-Addo, G. B. *Dalton Trans* **2004**, 189.